



**MEMS-BASED LINEAR
THERMOPILE DETECTOR ARRAYS
FOR IR MICROSPECTROMETERS**

HUAIWEN WU





Uitnodiging

Hierbij nodig ik U van harte uit
voor het bijwonen
van de verdediging van mijn
proefschrift getiteld

MEMS-based Linear Thermopile Detector Arrays for IR Microspectrometers

op vrijdag 26 augustus 2011
van 12:30 tot 13:30 uur
in de Promotiezaal (1e etage)
van het Science Centre
TU Delft,
Mijnbouwstraat 120 te Delft.



Voorafgaand aan de
verdediging, om 12:00 uur,
zal ik een korte uitleg geven
over mijn werk.

Na afloop bent U van harte
welkom op de receptie in de
Faculty Room in het Science
Centre.

Huaiwen Wu

Email: h.w.wu@tudelft.nl

Tel: 015-2786285



Stellingen behorende bij het proefschrift
MEMS-based Linear Thermopile Detector Arrays
for IR Microspectrometers

Huaiwen Wu, Delft, 26 augustus 2011.

1. De omgevingscondities zijn uitermate belangrijk voor het verkrijgen van gunstige eigenschappen van een IR sensor: koeling is voor een fotonensor net zo belangrijk als vacuümzuigen is voor een thermisch sensor.
2. De "absorbers" die in dit proefschrift worden voorgesteld beperken zich niet tot toepassing in thermo-elektrische onderdelen, maar kunnen ook worden toegepast in zonnecollectoren en andere onderdelen.
3. "Absorbers" die gebaseerd zijn op het gebruik van metamaterialen combineren de functies van zowel absorptie als van spectrale filtering.
4. Het meten van lokale temperatuurverschillen maakt het mogelijk om met een thermokoppel op directe wijze opgenomen warmte te kunnen meten. In vergelijking met alternatieve thermo-elektrische onderdelen met dezelfde kwaliteiten gaat dit echter ten koste van gebruik van een groter chipoppervlak. Dit grotere oppervlak is nodig om lokaal contact te kunnen maken tussen twee grenslagen.
5. De voordelen die behaald zijn met het verminderen van warmtegeleiding via lucht door vacuümzuigen zijn van meer betekenis voor "surface-micromachined" onderdelen dan voor "bulk-micromachined" alternatieven (dit proefschrift, Figure 4-9).
6. Ofschoon het geweldig was een sensorsysteem te ontwikkelen uitgevoerd met microtechnologie, zou het toch tijdbesparend zijn geweest om hetzelfde te doen met macrotechnologie.

Stellingen behorende bij het proefschrift
**MEMS-based Linear Thermopile Detector Arrays
for IR Microspectrometers**

Huaiwen Wu, Delft, 26 augustus 2011.

7. Hoewel TUDelft binnenshuis een uitnodigende infrastructuur biedt voor het uitvoeren van onderzoek, vormt het Nederlandse weer de belangrijkste aanmoediging om er regelmatig gebruik van te maken.
8. Met het begrijpen van de complexiteit van het leven is het net zo gesteld als met het interpreteren van een meetresultaat. Je moet het statische gedrag begrijpen voordat je je in het dynamische domein begeeft.
9. Een positieve werkhouding doet je jonger voelen dan je leeftijd is. Dit is bijzonder nuttig voor het oplossen van al die problemen waarvoor je wordt gesteld bij het uitvoeren van experimenteel onderzoek.
10. Het opgroeien op een bergachtig eiland verschaft iemand het perspectief om de schoonheid van de natuur te zien; het uitvoeren van onderzoek in een vlak land op zeeniveau verwijdt iemands kijk op wetenschap.
11. Eén van de culturele verschillen tussen Oost en West: In Taiwan, zakelijke activiteiten worden verspreid over de gehele dag uitgevoerd. In Nederland, bel a.u.b. gedurende werktijd.

Deze stellingen worden oponeerbaar en verdedigbaar geacht en zijn als zodanig goedgekeurd door de promotor, prof. dr. ir. G.C.M. Meijer.

Propositions required for the thesis
**MEMS-based Linear Thermopile Detector Arrays
for IR Microspectrometers**

Huaiwen Wu, Delft, 26 august 2011.

1. The operating ambient is a key performance parameter for an IR sensor: cooling is as important to the photon sensor as evacuation is to the thermal sensor.
2. The absorbers presented in this thesis are not restricted to application in thermo-electric detectors, but they can be applied in solar collectors and other devices.
3. Absorbers based on metamaterials combine both the absorption and spectral-filtering functions.
4. Measuring the local temperature difference enables the thermocouple to directly measure absorbed heat, but comes at the expense of more chip area required than for alternative thermo-electric devices with the same performance. The larger area is needed to make thermal contact between two junctions locally.
5. The benefit gained from reducing heat conduction through air by evacuation is more significant for surface-micromachined devices than for bulk-micromachined devices. (This thesis, Figure 4-9).
6. Although it has been great to develop a sensor system in micro-technology, it would have taken much less time to do so in conventional macro-technology.

Propositions required for the thesis
**MEMS-based Linear Thermopile Detector Arrays
for IR Microspectrometers**

Huaiwen Wu, Delft, 26 august 2011.

7. Although Delft University of Technology offers an inviting indoor research infrastructure, it is the Dutch weather that provides the main incentive to make frequent use of it.
8. Understanding the complexity of life is like interpreting a measurement result. You have to understand DC behaviour before being able to jump into the AC domain.
9. A positive working attitude makes one feel even younger than one's age, which is particularly useful when trying to solve all those unexpected experimental problems.
10. Growing up on a mountainous island gives one the perspective of seeing the beauty of nature; performing research on a flat terrain at sea level widens one's view on science.
11. One of the cultural differences between East and West: In Taiwan, business activity is spread out over almost the entire day. In the Netherlands, please only call during office hours.

These propositions are regarded as opposable and defensible, and have been approved as such by the supervisor, prof. dr. ir. G.C.M. Meijer.

901237

MEMS-based Linear Thermopile Detector Arrays for IR Microspectrometers

Proefschrift

ter verkrijging van de graad van doctor
aan de Technische Universiteit Delft,
op gezag van de Rector Magnificus prof. ir. K.C.A.M. Luyben,
voorzitter van het College voor Promoties,

in het openbaar te verdedigen

op vrijdag 26 augustus 2011 om 12.30 uur

door

Huaiwen WU
elektrotechnisch ingenieur
geboren te Taipei, Taiwan

TU Delft Library
Prometheusplein 1
2628 ZC Delft

Dit proefschrift is goedgekeurd door de promotor:

Prof. dr. ir. G.C.M. Meijer

Copromotor: Dr. ir. R.F. Wolffenbuttel

Samenstelling promotiecommissie:

Rector Magnificus	voorzitter
Prof. dr. ir. G.C.M. Meijer	Technische Universiteit Delft, promotor
Dr. ir. R.F. Wolffenbuttel	Technische Universiteit Delft, copromotor
Prof. dr. G.M.H. Minas	University of Minho, Portugal
Prof. dr. P. Enoksson	Chalmers University of Technology, Sweden
Prof. dr. B. Dam	Technische Universiteit Delft
Prof. dr. ir. P.P.L. Regtien	Universiteit Twente
Dr. ing. G. de Graaf	Technische Universiteit Delft
Prof. dr. P.J. French	Technische Universiteit Delft, reservelid

ISBN: 978-94-6190-102-6

Printed by:

Ipskamp Drukkers B.V.

Josink Maatweg 43

7545 PS Enschede

The Netherlands

Copyright © 2011 by H. Wu

All rights reserved. No part of this publication may be reproduced or distributed in any form or by any means, or stored in a database or retrieval system, without the prior written permission of the author.

Printed in The Netherlands

Chapter 1. Introduction

1.1 Motivation and Objectives	1
1.2 Organization of this thesis	4
1.3 References	6

To my wife, Ifan and parents

Chapter 2. Architecture of the IR Microspectrometer

2.1 Introduction	2
2.2 Applications of the spectrometer	9
2.3 Configuration of a spectrometer	9
2.3.1 Dispersion of light	10
2.3.2 Operating principles	10
2.3.3 Dispersive component	11
2.3.3.1 Grating	11
2.3.3.2 Fabry-Perot interference filter	12
2.3.3.3 Metamaterial	13
2.4 Detection of infrared radiation	13
2.4.1 Photon detectors	14
2.4.2 Thermal detectors	15
2.4.2.1 Bolometer	18
2.4.2.2 Pyroelectric detector	19
2.4.2.3 Thermocouple/Thermopile-based detector	21
2.5 Commercially available mini- or micro- spectrometer on market	24
2.6 Conclusion	27
2.7 References	27

**Chapter 3. Design and Analysis of the Thermo-Electric
Detector: Radiant-to-Thermal Effect**

3.1 Introduction	31
3.2 Opto-thermal conversion	32
3.2.1 Metal black absorber	32
3.2.2 Carbon Nanotubes-based absorber	34
3.2.3 Metamaterials as an absorber	37
3.2.3.1 Metamaterial & Photonic crystal	38
3.2.3.2 The refractive index	39

Dit proefschrift is goedgekeurd door de promotoren:

Prof. dr. ir. G.C.M. Meijer

Sopromotor: Dr. ir. R.F. Wölfelbuttel
zinnig hat nell, shw yn of

Samenstelling promotiecommissie:

Rector Magnificus	voorzitter
Prof. dr. ir. G.C.M. Meijer	Technische Universiteit Delft, promotor
Dr. ir. R.F. Wölfelbuttel	Technische Universiteit Delft, copromotor
Prof. dr. G.M.H. Minas	University of Minho, Portugal
Prof. dr. P. Eriksson	Chalmers University of Technology, Sweden
Prof. dr. B. Dam	Technische Universiteit Delft
Prof. dr. ir. P.P.L. Regtien	Universiteit Twente
Dr. Ing. G. de Graaf	Technische Universiteit Delft
Prof. dr. P.J. French	Technische Universiteit Delft, reserve

ISBN: 978-94-6190-702-6

Printed by:
Ipskamp Drukkers B.V.
Jouink Maatweg 43
7345 PS Eersbode
The Netherlands

Copyright © 2011 by H. Wu

All rights reserved. No part of this publication may be reproduced or distributed in any form or by any means, or stored in a database or retrieval system, without the prior written permission of the author.

Printed in The Netherlands

Chapter 1. Introduction

1.1 Motivation and Objectives 1
 1.2 Organization of this thesis 4
 1.3 References 6

Chapter 2. Architecture of the IR Microspectrometer

2.1 Introduction 7
 2.2 Applications of the spectrometer 9
 2.3 Configuration of a spectrometer 9
 2.3.1 Dispersion of light 10
 2.3.2 Operating principles 10
 2.3.3 Dispersive component 11
 2.3.3.1 Grating 11
 2.3.3.2 Fabry-Perot interference filter 12
 2.3.3.3 Metamaterial 13
 2.4 Detection of Infrared radiation 13
 2.4.1 Photon detectors 14
 2.4.2 Thermal detectors 15
 2.4.2.1 Bolometer 18
 2.4.2.2 Pyroelectric detector 19
 2.4.2.3 Thermocouple/Thermopile-based detector 21
 2.5 Commercially available mini- or micro- spectrometer on market .. 24
 2.6 Conclusion 27
 2.7 References 27

Chapter 3. Design and Analysis of the Thermo-Electric Detector: Radiant-to-Thermal Effect

3.1 Introduction 31
 3.2 Opto-thermal conversion 32
 3.2.1 Metal black absorber 32
 3.2.2 Carbon Nanotubes-based absorber 34
 3.2.3 Metamaterials as an absorber 37
 3.2.3.1 Metamaterial & Photonic crystal 38
 3.2.3.2 The refractive index 39

3.2.3.3	The impedance matching	39
3.2.3.4	The resonance behavior	40
3.2.3.5	Types of metamaterials	41
3.2.3.6	Angle dependence & Polarization	42
3.2.4	Microwave absorber	43
3.2.4.1	Minimized reflection	44
3.2.5	Design of the absorber	47
3.2.6	Experimental results	53
3.2.7	Conclusion	57
3.3	References	58

Chapter 4. Thermo-Electric Effect and Design of the Detector Array

4.1	Introduction	63
4.2	Thermal parameters	64
4.2.1	The Seebeck effect	64
4.2.2	The thermal conductivity	65
4.2.3	Figure of merit of a thermoelectric material	66
4.3	Design a thermoelectric detector element (pixel)	67
4.3.1	Analytical modeling	68
4.3.1.1	Thermal modeling of cantilever structure	68
4.3.2	Figure of merit of a thermal detector	70
4.3.3	Numerical modeling method	72
4.4	Design the thermoelectric detector array for a grating based microspectrometer	73
4.4.1	The optical system	73
4.4.2	Design of thermopile array	75
4.4.3	Numerical verification of design	78
4.4.4	Pressure dependence	79
4.4.5	Theory and modeling of thermal cross-talk	82
4.4.5.1	Thermal conductivity of air	82
4.4.5.2	Theoretical considerations	83
4.4.5.3	Static response	84
4.4.5.4	Dynamic response	86

4.5 Design a thermoelectric detector array for LVOF based microspectrometer	89
4.6 Conclusion	90
4.7 References	90

**Chapter 5. Micromachining Technology for the Thermo-Electric
Detector**

5.1 Introduction	93
5.2 Bulk micromachining	94
5.2.1 Wet etching of silicon	95
5.3 Surface micromachining	95
5.3.1 Wet etching of oxide	96
5.4 Methods to prevent stiction	96
5.4.1 Freeze-drying	97
5.5 Conclusion	100
5.6 References	101

**Chapter 6. TE Detector Array Fabricated by Bulk
Micromachining**

6.1 Introduction	103
6.2 IC-compatible fabrication of the thermopile array	104
6.3 Experimental results	107
6.3.1 Sensitivity	107
6.3.2 Thermal cross-talk	108
6.4 Conclusion	111
6.5 References	113

**Chapter 7. TE Detector Array Fabricated by Surface
Micromachining**

7.1 Introduction	115
7.2 Fabrication of the absorber	116
7.3 Sacrificial etching by 73% liquid HF	120
7.4 Sacrificial etching by vapour HF	121

7.5 Experimental results	123
7.6 Conclusion	130
7.7 References	130
 Chapter 8. Conclusions	
8.1 Future work	136
Appendix A: Thermal analytical modeling	137
Abbreviations and Acronyms	149
Summary	151
Samenvatting	155
Acknowledgements	159
List of Publications	163
About the author	169

Introduction

1

1.1 Motivation and Objectives

The performance of laboratory infrared (*IR*) spectrometers, which include optics, electronics, firmware and software, has been enhanced consistently over the years. Presently, the overall system is typically capable of satisfying a resolution of 8 cm^{-1} (3.2 nm) at a wavelength of $2\text{ }\mu\text{m}$, which is more than adequate for the vast majority of applications [1.1]. Spectrometers which measure an optical spectrum have huge potential in many applications, such as in chemistry, medicine, space exploration, agriculture, and quality control in manufacturing industries [1.2]. However, laboratory spectrometers have several operational drawbacks, such as size, cost, high power consumption and lack of capability to perform the in-situ measurements. Therefore, there is an increasing demand for miniaturizing *IR* spectrometers by means of the well-developed integrated circuit (*IC*) technology. When miniaturized, a device can provide operational advantages such as portability and smaller sample requirements.

This thesis describes *IR* micro-spectrometers which are based on components that are fabricated using photonic and micro-electro-mechanical systems (*MEMS*) technologies. The micro-spectrometer may operate either by using an array of detectors, each with a uniform or spectrally selective response,

or by scanning the dispersed light using a single calibrated detector. Both methods have advantages and drawbacks. The system with a single calibrated detector can offer the options of being lower cost and having a simple design. However, the scanning time is longer during the wide spectral range scan. The complete system can even malfunction or have stability issues if the single detector is damaged or drifts. Therefore, the implementation of a detector array is usually preferred.

In general, *IR* detectors¹ can be divided into two categories: photon and thermal. Photon detectors perform much better in terms of sensitivity and response time. However, the material used for fabrication of photon detectors is not silicon, because of physical limitations. As a result, the integration of a *CMOS* process into the read-out electronics is less possible due to compatibility issues. Furthermore, the spectral response of the photon detector is not flat, meaning that the detector needs to be characterized before use in some spectral scan applications. Thermal detectors, on the other hand, convert the infrared radiation into the heat flux. The heat flux can be further converted into the electrical signal by the transduction effect. Moreover, thermal detectors can be fabricated using silicon technology, which makes it possible to integrate the electronics into the system.

Thermal detectors are suitable for consumer applications, where a moderate performance is required in terms of sensitivity and response time. The spectral response of the detector is flat due to the coating material. By applying the new technology of absorber, the spectral response can be custom tuned to achieve the spectral selective function. This option increases the possibility of further reducing the number of optical components in the micro-spectrometer.

The target of this thesis is to design an *IR* detector array for use in micro-spectrometer applications. Since the emphasis is on the compatibility with a *CMOS* process, a system with a *CMOS*-compatible silicon thermal detector array is pursued. The thermal detector array has a wide range of applications and it can be used not only in spectroscopy but also to acquire the temperature profile of the object. The potential applications of the thermal detector array are listed in Table 1.

1. The term detector is also meant 'sensor' represented in the whole thesis.

TABLE 1. Potential applications of thermal detector. [1.3]

Area	Use	Application
Automotive industry	Exhaust gases	Gas analysis
	Tyres	Temperature
	Engine Technique	Temperature
Medical	Breathing air	Gas analysis
	Anaesthesia	Gas analysis
	Body temperature	Temperature
Industry	Steel industry	Temperature
	Rolling mills	Temperature profile
	Mechanical engineering	Temperature
	Industrial plants	Temperature
Agriculture	Greenhouses	Gas analysis
	Foods	Temperature
Air conditioning technology	CO ₂ /Air measurement	Gas analysis
Security	Gas concentration	Gas analysis
Military equipment	Protection from poisonous gases	Gas analysis
	Troop movement	Temperature
Space [1.4]	Thermal imager	Temperature

Hence, the objectives to achieve a high-performance *CMOS*-compatible *IR* micro-spectrometer are listed as follows:

- Design the optical systems for an *IR* micro-spectrometer.
- Analyze and evaluate all available absorbers which perform the radiant-to-thermal conversion.
- Analyze and compare all available thermo-electric *CMOS* compatible materials.

- Design and optimize a pixel based on the geometries, materials and projected image from optics.
- Design and optimize a detector array based on the single pixel and projected image of optics.
- Analyze and implement the fabrication technologies on the device.
- Integrate the optical system with the detector array.

1.2 Organization of this thesis

The objectives and motivation of the work presented in this thesis were introduced in previous section. An overview of the contents of this thesis is presented below:

Chapter 2 Architecture of the IR Microspectrometer

An overview of microspectrometers based on different operating principles is introduced. A new type of spectrometer using metamaterial is purposed as well. This spectrometer has the potential to be either implemented with other optics or used alone such that the number of required optical components in the microspectrometer can be further reduced. Since this thesis concentrates mainly on the thermal detector, various types of thermal detectors are analyzed and their characteristics are compared with the photon detector. A market survey of commercially available products based on different operating principles is also investigated. The survey shows that not many micro-scale spectrometers can be found, which constitutes one of the driving forces behind this research.

Chapter 3 Design and Analysis of the Thermo-Electric Detector: Radiant-to-Thermal Effect

As a tandem detector, the thermal detector performs two conversions: a radiant (optical)-to-thermal and a thermo-to-electrical conversion. This chapter discusses the various types of absorbers that can be utilized for the optical-thermal conversion. Two new types of absorbers are introduced: carbon nanotubes and metamaterials. Each type of absorber has its strengths and weaknesses. The choice of absorber is based on the conversion efficiency and process compatibility.

Chapter 4 Thermo-Electric Effect and Design of the Detector Array

Chapter 4 discusses the thermo-to-electrical conversion by exploiting the Seebeck effect. Although the selected materials do not have the best thermoelectric (*TE*) effect, the choice of materials and fabrication strategy is driven by *CMOS* compatibility. The second part of this chapter presents the design and an advanced analysis. The design starts from a single element and then extends to an array that is suitable for the imaging of the dispersive spectrum. The design analysis includes the analytical modeling and numerical method for verification.

Chapter 5 Micromachining Technology for the Thermo-Electric Detector

The performance of the thermal detector is determined by its structure and the extent to which the transduction effect can be actually used. Therefore, micromachining technology is required to realize a *3D* device in which the thermal loss is minimized. Two types of conventional micromachining technologies are discussed separately.

Chapter 6 TE Detector Array Fabricated by Bulk Micromachining

A thermoelectric detector array fabricated by bulk micromachining is introduced. As the preliminary yield after the fabrication is not acceptable, the process needs to be modified in order to maintain good mechanical stability. Moreover, a device fabricated by bulk micromachining has less freedom in the post-packaging process, which is often used nowadays to improve the performance of the device substantially.

Chapter 7 TE Detector Array Fabricated by Surface Micromachining

This chapter discusses a thermoelectric detector array fabricated by surface micromachining. The fabrication of the interference-based *IR* absorber is presented. The performance of the detector array is discussed in the final part of this chapter. Although the performance of the device has much lower sensitivity compared to the device processed with bulk micromachining, it can be further improved by advanced packaging technology such as wafer-level packaging or thin-film encapsulation.

Chapter 8 Conclusions

The whole work presented in the thesis is summed up in this chapter, and several relevant inferences and future research are proposed as well.

1.3 References

- [1.1] R. A. Crocombe. (2008, 01/Jan) Miniature Optical Spectrometers: There's Plenty of Room at the Bottom Part I, Background and Mid-Infrared Spectrometers. Spectroscopy. Available: <http://spectroscopyonline.findanalytichem.com/>
- [1.2] R. F. Wolffenbuttel, "MEMS-based optical mini- and microspectrometers for the visible and infrared spectral range," *Journal of Micromechanics and Microengineering*, vol. 15, p. S145, 2005.
- [1.3] Micro-Hybrid Electronic GmbH (2011). Application Note Thermopile Detectors. Available: <http://www.micro-hybrid.de/>
- [1.4] C. R. Webster. (2010). Solar System Exploration: Status of Planetary Science Instrument Technologies. Available: <http://www.spacepolicyonline.com/>

Architecture of the IR Microspectrometer

2

2.1 Introduction

A spectrometer is an optical instrument used to measure properties of light over a specific part of the electromagnetic spectrum, as shown in Figure 2-1. It is used in spectrometry for producing spectral lines and measuring the wavelengths and intensities of light emitted, reflected or transmitted by a sample under test. Small, light-weight, miniature spectrometers for measuring an optical spectrum have a huge functionally potential in many applications, such as chemistry, medicine, space, agriculture and quality inspection in the manufacturing industries [2.1].

The practical advantages of the miniaturization of the spectrometers are their portability and the possibility to perform in-situ measurements. The miniaturization can also ease the integration of micro and miniature spectrometers into other technologies like microelectronics to results in lab-on-a-chip devices which are in great demand. Combining the microspectrometer with microelectronics enables the integration of the functionality that is required to realize the kind of user-friendliness that is required in medical applications, such as point of care diagnostics.

The pixel number in combination with the slit and grating options determines both the dimensions and resolving power. Normally, the dispersion, or the wavelength range divided by the number of pixels, is utilized while discussing the resolution. Full width-half maximum (*FWHM*), or the width of a peak at half of its maximum intensity is a better way of determining the resolution [2.2]. Based on the *FWHM* the actual optical performance of one spectrometer design can be compared directly to another. This chapter chiefly introduces the applications of the spectrometer in the first section. The different types of the spectrometers are demonstrated according to operating principle. A new type of spectrometer using metamaterials is subsequently introduced. Since this thesis emphasizes the detector array, an overall view of available detector arrays is presented as well. Finally, the commercially available mini or micro-spectrometers are outlined in the last section.

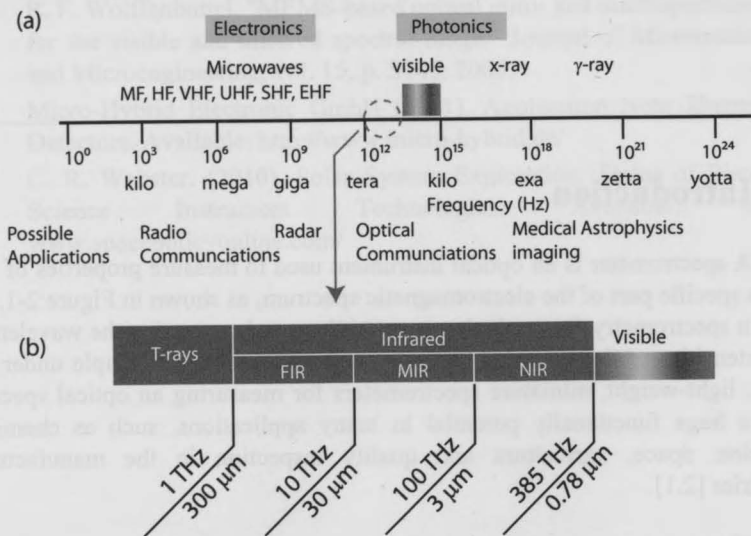


Fig. 2-1. (a) The electromagnetic radiation spectrum. (b) The infrared spectrum (FIR: far infrared, MIR: mid infrared, NIR: near infrared).

2.2 Applications of the spectrometer

In science, medicine and industry, spectroscopy is used to completely understand the chemical composition of a gas, liquid or solid of interest. Spectroscopy is the use of the absorption, emission, or scattering of electromagnetic radiation by materials to study atom or molecules or to observe physical processes. IR absorption spectroscopy is the most frequent and most important implementation [2.4]. An example is shown in Figure 2-2 showing the IR absorption spectra of water, CO_2 , and ethanol.

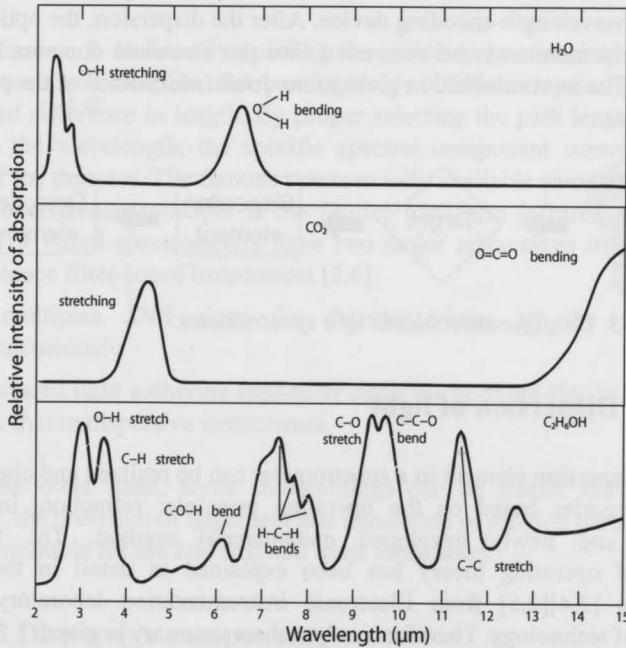


Fig. 2-2. IR absorption spectra of water, CO_2 and ethanol [2.3].

2.3 Configuration of a spectrometer

The generic configuration of the spectrometer is illustrated in Figure 2-3. A suitable light source can be used to generate a continuous or pulsed optical signal.

Pulsed light typically enables the use of measurement techniques that result in a higher signal-to-noise ratio (SNR). The amplitude or spectral distribution of the light is changed after passing through the target, which contains compounds that adsorb light at specific spectral components or generate new components by photoluminescence. Thus the information of the target is encoded in the spectrum of the light. The spectrometer is used to decode this information. The dispersion element is used to separate the broadband light signal into several narrowband signals.

In general, two different devices are used for the dispersion: a wavelength-selective or wavelength-encoding device. After the dispersion, the optical signals are accurately measured and converted into the electrical domains for further processing. The next sub-section gives more detail information of the principle of the dispersion.

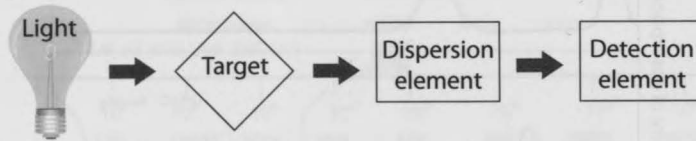


Fig. 2-3. Configuration blocks of a spectrometer.

2.3.1 Dispersion of light

The dispersion element in a spectrometer can be realized and classified into several categories based on the operating principle: refraction, interference, diffraction and newly developed metamaterial method. The first three foundational operating theory has been explained in detail in the previous dissertations [2.4][2.5] from Electronic instrumentation laboratory of Delft university of technology. Therefore, only a short summary is given.

2.3.2 Operating principles

Refraction

The refraction occurs when the light of interest is incident on a medium with different optical indexes. The prism and optical fiber are the renowned examples. The different spectral components end up at the detector due to the

different speed.

Diffraction

When a monochromatic light is incident on the surface of the grating with multi slits, it passes through the grating and is diffracted into several spectral components. The distance between two slits, namely the grating constant determines the diffraction response.

Interference

Interference is realized by splitting the incident radiation into two beams. The two beams will interfere after passing the two different optical paths with a well defined difference in length. By proper selecting the path length difference relative to the wavelength, the specific spectral component comes out at the entrance of the detector. The famous commercially available standard instrument using the interference principle is the fourier transform infrared spectrometer (*FTIR*). *FTIR* based spectrometers have two major advantages over dispersive and interference filter-based instruments [2.6]:

- A multiplex *SNR* since the detector views all the wavelengths simultaneously.
- Enhanced light gathering capability since the aperture size is much larger than that in dispersive instruments.

On the other hand, some shortcomings can be stated: the mechanical complexity, the precision of alignment and translation of moving parts. Therefore, it is less favourable for the low cost and mass fabrication.

2.3.3 Dispersive component

2.3.3.1 Grating

In 2001, S.H. Kong et al. [2.5] reported an infrared microspectrometer using diffraction grating as the dispersive element, as shown in Figure 2-4. The benefits are no-moving parts used in the system and high speed. It has been stated that the system performance is driven by not only the grating but the slit (both entrance and exit) and detector (number of and size of pixels) as well. The different types

of gratings have different efficiency curves and the imaging pattern, which is also important during optimization. A grating-based microspectrometer is designed in this thesis as well. Then the next chapter will explore the optimization of the detector array based on the imaging pattern of the grating.

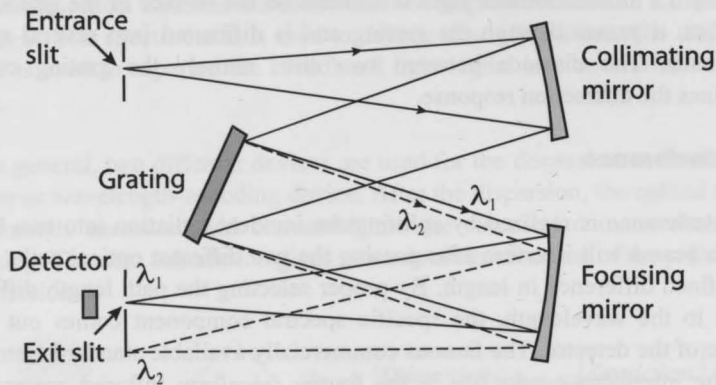


Fig. 2-4. A grating spectrometer [2.4].

2.3.3.2 Fabry-Perot interference filter

Fabry-Perot interferometer is another type of the device using interference principle except *FTIR*. A specific wavelength can be selected by simply adjusting the width of resonating cavity in the Fabry-Perot etalons as shown in Figure 2-5. J.H. Correia et al. [2.7] published a micro-spectrometer with Fabry-Perot interferometer in the visible range. It is arranged in a 4×4 array in which each pixel has one Fabry-Perot etalon channel to a selective specific wavelength. As a result, no moving part is required.

A. Emadi et al. [2.8] reported a continuous bandpass filter which has been intentionally wedged in one direction. This linear variable optical filter (*LVOF*) is fabricated using the reflow of photoresist and transferred the wedge shape into the silicon by etching process. The *LVOF* can be fabricated by other methods and is

commercially available [2.9].

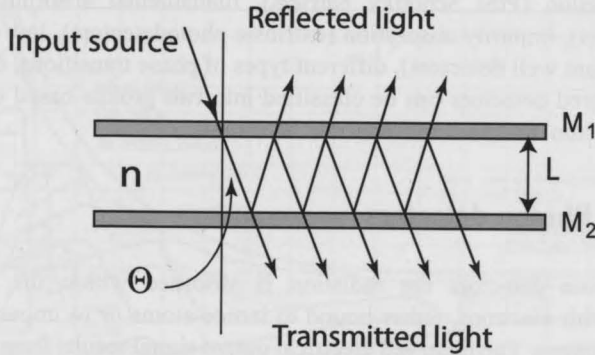


Fig. 2-5. Fabry-Perot etalon [2.4].

2.3.3.3 Metamaterial

The metamaterial is defined as a substance that acquires its electromagnetic properties from imbedded physical structures instead of from its chemical composition. Therefore they are artificial materials engineered to have properties that may not be found in nature. We propose to use metamaterial to perform the spectral selection function. The idea is to simply integrate the dispersive element and the detection function in the detector array such that the number of components can be reduced to achieve the low-cost requirement for mass production. It is also possible to combine with an external optical filter, for instance *LVOF*, in the system to realize a high resolution microspectrometer. The principle of the metamaterial based-spectrometer is discussed in the next chapter.

2.4 Detection of Infrared radiation

Infrared radiation was discovered by Herschel using a mercury-glass thermometer to detect the sunlight that had been dispersed by a prism [2.10]. From the history of the development in the *IR* detector technology, a simple theorem can be declared: All physical phenomena in the range of about 0.1-1 eV (12-1.2 μm in wavelength) can be proposed for infrared detectors [2.11]. Those applications of the effects are thermoelectric power (thermocouples), change in electrical conductivity (bolometers), gas expansion (Golay cell), pyroelectricity

(pyroelectric detectors), photon drag, Josephson effect (Josephson junctions), internal emission (PtSi Schottky barriers), fundamental absorption (intrinsic photodetectors), impurity absorption (extrinsic photodetectors), low dimensional solids (quantum well detectors), different types of phase transitions, etc [2.12]. In general, infrared detectors can be classified into two groups based on operating principle: Photon detectors and Thermal detectors.

2.4.1 Photon detectors

In photon detectors the radiation is absorbed within the material by interaction with electrons, either bound to lattice atoms or to impurity atoms or with free electrons. The observed electrical output signal results from the changed electronic energy distribution. The photon detectors show a selective wavelength dependence of response per unit incident radiation power. They exhibit both good signal-to-noise performance and a very fast response. Photon detectors for long-wavelength operation (beyond about 3 μm) are generally cooled to avoid a detection limit by high leakage current by thermal generation of charge carriers. The thermal transitions compete with the optical ones, making non-cooled devices very noisy. Cooling requirements are the main obstacle to the more widespread use of *IR* systems based on the semiconductor photo detectors, making them bulky, heavy, expensive and inconvenient to use [2.13].

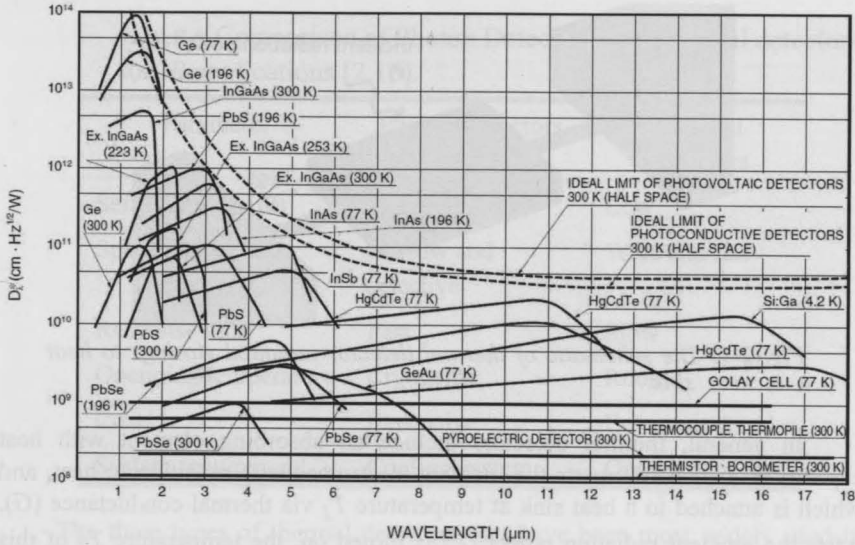


Fig. 2-6. Comparison of the detectivity D^* of various commercially available infrared detectors when operated at the indicated temperature. Chopping frequency is 1000 Hz for all detectors except the thermopile (10 Hz), thermocouple (10 Hz), thermistor bolometer (10 Hz), Golay cell (10 Hz) and pyroelectric detector (10 Hz). Each detector is assumed to view a hemispherical surrounding at a temperature of 300 K. Theoretical curves for the background-limited D^* (dashed lines) for ideal photovoltaic and photoconductive detectors and thermal detectors are also shown. [2.14] year:2005

2.4.2 Thermal detectors

Another group of infrared detectors is the thermal detectors. The incident radiation is absorbed to change the material temperature, and the resulting change

in some physical properties is used to generate an electrical output.

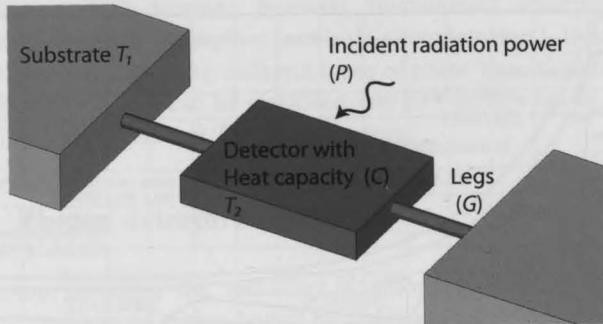


Fig. 2-7. The schematic of thermal detector mounted via legs to heat sink.

In general, thermal detectors include an absorbing element with heat capacity (C) which converts the incident electromagnetic radiation to heat, and which is attached to a heat sink at temperature T_1 via thermal conductance (G). After the incident radiation power (P) is turned on, the temperature T_2 of this absorbing element initially increases with time at rate $dT_2/dt = P/C$ and approaches the limiting value $T_2 = T_1 + P/G$ with the thermal time constant $\tau = C/G$. When the radiation is turned off, the temperature is reduced again to T_1 with the same time constant τ . Thermal detectors are frequently used in combination with an optical chopper to give a periodic response to a signal which is modulated at a frequency $\omega \approx 1/\tau$. The signal does not depend upon the band gap structure of the detector material in relation for the photonic nature of the incident radiation. Thus, the thermal effects are generally wavelength independent. In contrast to photon detectors, thermal detectors typically operate at room temperature. The heating and cooling of a detector element by absorbed radiation is a relatively slow process, which results in a modest sensitivity and slow response relative to photon detectors [2.15]. Nevertheless, it has found wide spread use in consumer applications, where high sensitivity or fast response is not required. The comparison between photo and thermal detectors is shown in Table 1.

TABLE 1. Comparison of Photon Detectors and Thermal detectors for IR applications [2.16].

Parameter	Photon Detectors	Thermal Detectors
Sensitivity	High	Low
Spectral response	Narrow and selective	Wide and flat
Response time	Fast	Slow
Operating temperature	Cryogenic	Room
Cost	Expensive	Economical
System requirement	Cooling system	Optical chopper

The three types of thermal detectors that have been most widely used in infrared systems are elaborated in the following sub-section. These and other types of thermal detectors are presented in Table 2.

TABLE 2. Thermal detectors [2.17].

Detector type	Operating principle	Change due to temperature variation
Bolometer:(Metal Semiconductor Superconductor Ferroelectric Hot electron)	Change in electrical conductivity	Resistance
Thermocouple /Thermopile	Voltage generation, caused by change in temperature of the junction of two dissimilar materials	Voltage
Pyroelectric	Change in spontaneous electrical polarization	Capacitor
Golay cell /Gas microphone	Thermal expansion of a gas	Mechanical displacement

2.4.2.1 Bolometer

Advanced bolometers use surface micro-machined bridges on *CMOS* processed wafers, where the infrared radiation increases the temperature of a material formed on the thermally isolated and suspended bridge, causing a change in its resistance related to its temperature coefficient of the resistance. As a result temperature coefficient resistance (*TCR*), depending on the material, is needed to be as high as possible.

The most popular material used in fabrication of the bolometer is vanadium dioxide, VO_2 [2.18]. Actually more than 95% market of 2D imager uncooled *IR* detectors was taken by VO_2 -based technologies in 2010 [2.19]. The reason is the huge development costs were paid for by US military research. The *DC* sensitivity can be reached several thousands of volts per watt [2.20]. F. Niklaus et

al. reported a good overview on *MEMS* based uncooled *IR* bolometer array [2.21]. Unfortunately, VO_2 is not a standard material in *IC* fabrication and requires dedicated expensive equipment to prevent the contamination of the *CMOS* line. Moreover, the external source applied on the bolometer may cause self-heating which will introduce the inaccuracy measurement. The external source also limits the application where each energy payload is taken into account.

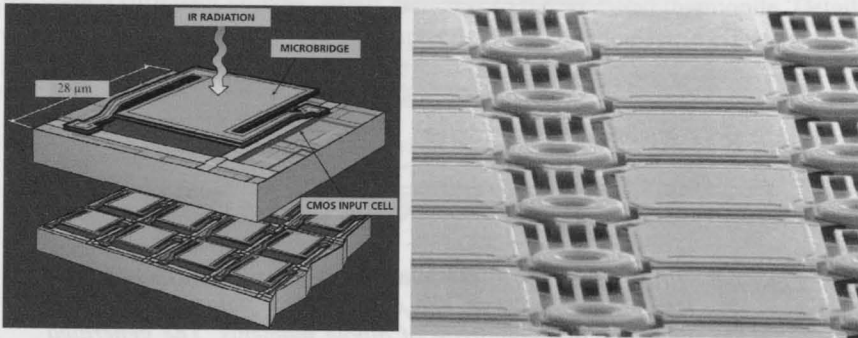


Fig. 2-8. The uncooled microbolometer array [2.22].

2.4.2.2 Pyroelectric detector

Pyroelectricity is the electrical potential created in certain materials by polarization when heated. As a result of a change in temperature, positive and negative charges accumulate or move to opposite ends of the material and hence, an electrical potential results [2.23]. A simple pyroelectric detector is illustrated in Figure 2-9. Overviews of micromachined infrared detectors based on pyroelectric materials are available [2.24][2.25].

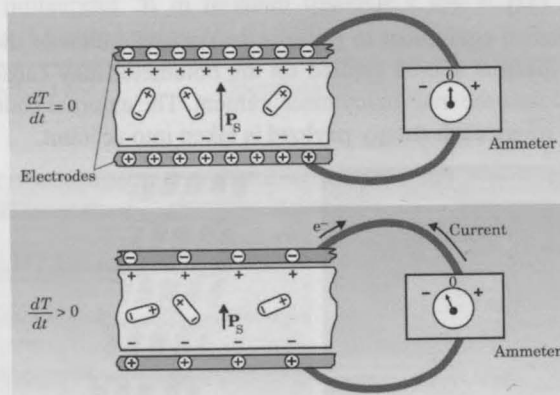


Fig. 2-9. Illustration of a pyroelectric detector. An increase in temperature prompts the spontaneous polarization P_s to decrease the magnitude of dipole moments. The generated electric potential results the current when the load (Ammeter) is mounted [2.26].

According to the report of S. Tadigadapa and K. Mateti [2.24], there are essentially three approaches for realizing piezoelectric MEMS IR devices:

- Deposition of piezoelectric thin films on silicon substrates with appropriate insulating and conducting layers followed by silicon surface or bulk micromachining to realize the micromachined transducers.
- Direct bulk micromachining of single crystal or polycrystalline piezoelectrics and piezoceramics with electrodes added to realize micromachined transducers.
- Integration of micromachined structures in silicon via bonding techniques with bulk piezoelectric substrates.

A good example of a commercially available linear pyroelectric array can be obtained from DIAS Infrared GmbH [2.27]. The array is produced in a hybrid fashion where the read-out circuit and a subcarrier with the pyroelectric chip are placed on a thick-layer wiring carrier. The resulting array has up to 256 elements and a responsivity up to 65 kV/W. However, the noise equivalent power (NEP) is less favourable due to the high impedance of pyroelectric films.

2.4.2.3 Thermocouple/Thermopile-based detector

Two dissimilar materials are connected at two junctions to make a thermocouple as shown in Figure 2-10. When there is a temperature difference, a voltage is generated due to the Seebeck effect in the thermoelectricity. In general, two or more thermocouples are required across the same temperature difference for yield a sufficient voltage output, which is to the so called thermopile. Details of the Seebeck effect are given in chapter 4. Other thermoelectric effects are: the Peltier effect, and the Thomson effect.

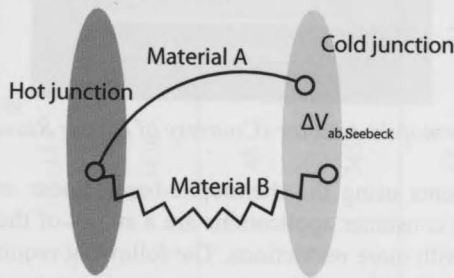


Fig. 2-10. A simple thermocouple.

Forcing an electric current through the thermocouple results in a temperature difference between the two junctions. This effect is referred to as the Peltier effect. The current results in a transfer of heat from one junction to the other, which means one junction cools down while the other one heats up. As a result, this effect can be practically applied as an integrated thermoelectric cooler in a microsystem [2.28].

The Thomson effect describes the heating or cooling of a current-carrying conductor in case of a temperature gradient. Any current-carrying conductor, with a temperature difference between two points, will either absorb or release heat, depending on the material. However, there is still no prominent application in micro-electronics so far.

A good example of a supplier of thermopile-based IR detector arrays is Dexter Research [2.29]. Figure 2-11 shows a 2 x 16 staggered element silicon-based thermopile array.

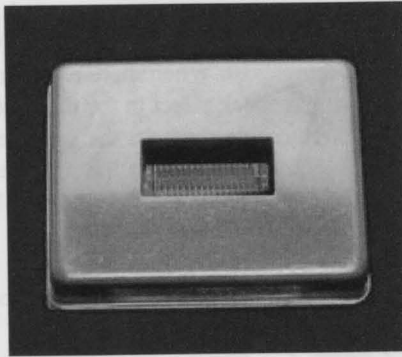


Fig. 2-11. Thermopile detector (Courtesy of Dexter Research, USA).

The requirements using the thermopile-based linear array for use in the spectroscopy in the consumer applications are a subset of the space application, which is typically with more restrictions. The following requirements are used in the space application [2.30]:

- Uncooled detector array
- Flat and broadband response
- No requirement of electrical bias
- Reduction of mass, size and cost
- Stability with substrate temperature
- Linear Response
- Calibrated response for radiometry
- Radiation hard
- CMOS compatibility

Except for the radiation hardness, these requirements are also relevant to the thermopile array for terrestrial use. Table 3 reveals the typical performance specifications of some commercially available linear thermopile arrays.

TABLE 3. Performance of available thermopile linear array. [2.31]

Array	Thermopile Material	Encaps. Gas	Pixel Size (mm), Nr. of pixels	Re (k Ω)	D* (10 ⁶ cmHz ^{1/2} W ⁻¹)	Sensitivity (V/W)	Time constant (ms)	Thermal cross-talk (%)	TCR (%K ⁻¹)
SLA32 [2.29]	PolySi/Al	N ₂	0.5×0.65	76	0.7	15	7	negligible	-0.04
JPL [2.32]	BiTe/BiSbTe	vacuum	0.24×0.48, 21	130	10	1450	85	-	-0.4
TPL64 [2.33]	BiSb/Sb	N ₂	0.45×1.5, 64	9	2.8	45	43	28	-0.6
					16	245	150	-	
IRSLA [2.31]	nPolySi/pPolySi	N ₂	0.45×2, 64	75	1.2	65	31	17	-0.04
					4.5	245	75	-	

It has been shown from the table that the thermopile detectors have low impedance, while pyroelectric detectors have very high impedance. Therefore usually an amplifier or an impedance converting buffer is required to make them functionally usable. The low impedance of the thermocouple is an advantage, because the associated circuitry is less susceptible to disturbance from extraneous radiation and electrical noise. Another point of view is that thermopile detector output is proportional to incident radiation, while the output of the pyroelectric detectors is proportional to the rate of change in the incident radiation. Therefore, the thermopile detector is *DC* coupled, whereas the pyroelectric detector is *AC* coupled.

The often-mentioned self-generating effect of the thermopile (no external electric power source required) is of limited value, because of the relatively low thermo-electrical sensitivity and the high-gain amplifier is required.

2.5 Commercially available mini- or micro-spectrometer on market

One of commercially available miniaturized *FTIR* is from Carinthian Tech Research AG [2.34]. This device employed a resonantly driven micromirror, suspended on two long springs, driven by interlocking comb-structured electrodes, and contained in a vacuum chamber. The spectrometer covers a spectral range from 2 to 6 μm , using a thermoelectrically cooled Mercury Cadmium Telluride (*MCT*) detector with a spectral resolution of 48 nm at 4 μm . It has a footprint of $140 \times 120 \times 120 \text{ mm}^3$ and a mass of about 1.5 kg.

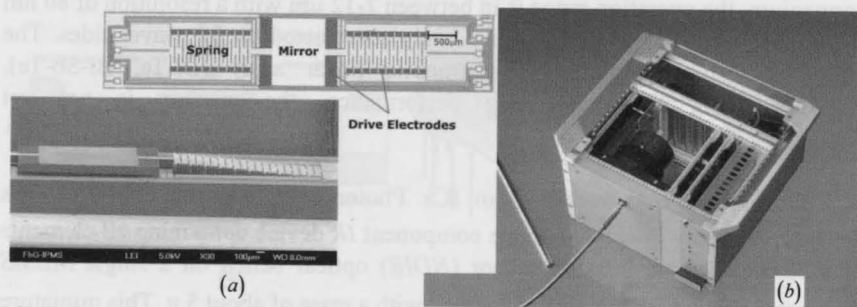


Fig. 2-12. (a) A translational micromirror component, using two long bending springs [2.35] for use in (b) a miniaturized FTIR spectrometer (Courtesy of CTR, Villach, Austria)

A compact mid infrared (MIR) spectrometer from Wilks Enterprise employs an uncooled 64-element pyroelectric array and an LVOF, resulting a monolithic, no-moving-parts design. Two standard spectral ranges are offered: 2.5-4.8 μm and 5.4-10.8 μm . The spectral range is limited and defined by the LVOF. This instrument has a built-in attenuated total reflectance sample interface and features a resolution of 40 nm at 4 μm . The volume is $152 \times 165 \times 70 \text{ mm}^3$ with the weight of 1.5 kg.

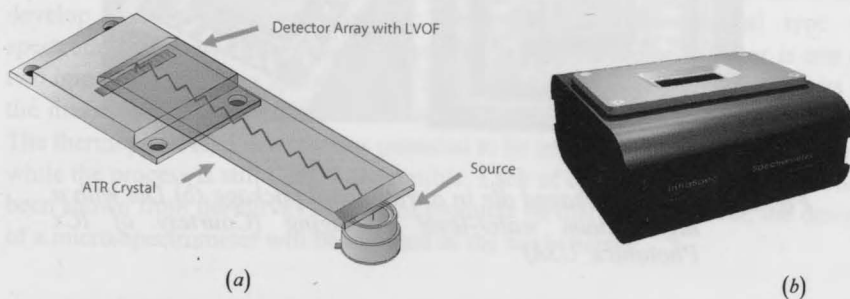


Fig. 2-13. (a) Optical diagram of the optical head [2.36] for use in (b) a portable MIR spectrometer (Courtesy of Wilks Enterprise Inc. East Norwalk, CT USA)

ICx Photonics [2.37] uses a slab waveguide spectrograph design, using either silicon or germanium. The spectrograph that is based on silicon can operate

in the 3-5 μm range with a spectral resolution of 20 nm at 4 μm . In case of germanium, the operation range is in between 7-12 μm with a resolution of 80 nm at 10 μm . The grating was lithographically constructed on the waveguides. The detection system employs 64 thermopile linear array (Bi-Te, Bi-Sb-Te). Notwithstanding the outstanding performance, the product is not yet commercially available.

One interesting product from ICx Photonics is the one chip CO_2 gas detector. A highly integrated single component IR device containing all elements of a Non-dispersive infrared sensor (NDIR) optical bench on a single MEMS bolometer chip which has size of 2.9 cm^2 with a mass of about 5 g. This miniature device generates narrowband infrared radiation tuned to a specific gas by using a photonic crystal rather than a conventional optical filter. The emitter provides tuned output with 85% of the blackbody power at the CO_2 wavelength and suppresses emission at other bands for high CO_2 selectivity and power efficiency. The resulted device can detect CO_2 in a range of 0-100% with a detection limit of about 100 ppm.

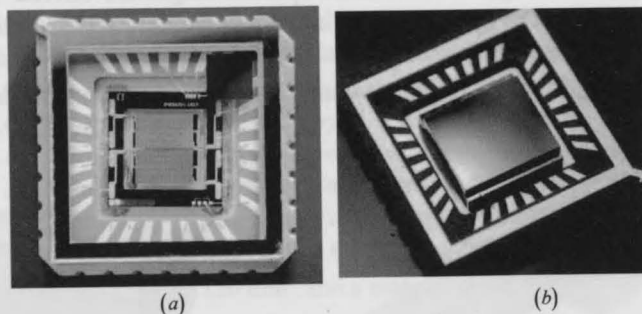


Fig. 2-14. (a) Unpackaged die in a traditional package (b) Die with a high-vacuum wafer-level packaging (Courtesy of ICx Photonics, USA)

Infratec GmbH [2.38] offers a tiny MIR spectrometer that is based on a single pyroelectric detector and a tunable Fabry-Perot interferometer in a TO-8 package. The operating principle is illustrated in Figure 2-15(a). The micromachined Fabry-Perot element is used for scanning over a range of wavelengths by simply adjusting the control voltage. The bandwidth of these filters is typically in the range of 60-100 nm. The tuning range is from 3-4.1 μm and 3.9-5 μm . Although the tuning range is limited by pull-in and also the spectral

bandwidth is limited, the advantage is the compact system.

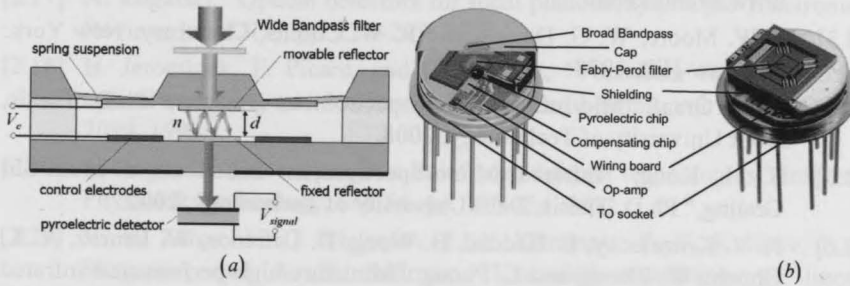


Fig. 2-15. (a) Schematic overview of the tunable Fabry Perot filter based spectrometer and (b) the system in TO-8 package (Courtesy of InfraTec GmbH, Dresden, Germany)

2.6 Conclusion

The interaction between IR and target matters has been generally clarified. Spectrograph acquired from spectrometer can be used to analyze the activity from a specific target. The reduced volume, weight and cost are favourable for either the space and consumer application. Therefore, this is a drive to research and develop on the micro-spectrometer. Excluding the conventional type of spectrometer, a new type using metamaterial is purposed. The detector is one of two important parts in a spectrometer. The thermal detectors have some merits in the mass production albeit the less sensitivity compared with photon detectors. The thermopile-based detector has potential to be integrated in a complete system while the process is still CMOS compatible. Lack of completed micro-system has been shown from the survey of current products on market. Moreover, the design of a micro-spectrometer will be initiated in the next chapter.

2.7 References

- [2.1] R. F. Wolffenbuttel, "MEMS-based optical mini- and microspectrometers for the visible and infrared spectral range," *Journal of Micromechanics and Microengineering*, vol. 15, p. S145, 2005.

- [2.2] G. Neece. How to Configure a Microspectrometer. Available: <http://www.avantes.com/>
- [2.3] J. W. Moore, W. G. Davies, and R. W. Collins, Chemistry. New York: McGraw-Hill, 1978.
- [2.4] G. de Graaf, "Mid-Infrared Microspectrometer Systems," Ph.D. Thesis, Delft University of Technology, 2008.
- [2.5] S. H. Kong, "Infrared Micro-Spectrometer Based on a Multi-Slit Grating," Ph.D. Thesis, Delft University of Technology, 2002.
- [2.6] R. V. Kruzelecky, E. Haddad, B. Wong, D. Lafrance, W. Jamroz, A. K. Ghosh., W. Zheng, and L. Phong, "Miniature high-performance infrared spectrometer for space applications," in the 5th International Conference on Space Optics (ICSO 2004), 2004, pp. 203-210.
- [2.7] J. H. Correia, G. de Graaf, S. H. Kong, M. Bartek, and R. F. Wolffenbuttel, "Single-chip CMOS optical microspectrometer," Sensors and Actuators A: Physical, vol. 82, pp. 191-197, 2000.
- [2.8] A. Emadi, H. Wu, S. Grabarnik, G. De Graaf, K. Hedsten, P. Enoksson, J. H. Correia, and R. F. Wolffenbuttel, "Fabrication and characterization of IC-Compatible Linear Variable Optical Filters with application in a micro-spectrometer," Sensors and Actuators A: Physical, vol. 162, pp. 400-405, 2010.
- [2.9] JDS Uniphase Corporation. Available: <http://www.jdsu.com/>
- [2.10] W. Herschel, "Experiments on the Refrangibility of the Invisible Rays of the Sun," Philosophical Transactions of the Royal Society, vol. 90, pp. 284-292, 1800.
- [2.11] P. R. Norton, "Infrared detectors in the next millennium," vol. 3698, pp. 652-665, 1999.
- [2.12] G. T. Kovacs, Micromachined Transducers Source Book McGraw-Hill Higher Education, 1998.
- [2.13] T. Deguchi, "Unique Pyroelectric Elements Lead to Size Drops in IR Image Sensors," Journal of Electronic Engineering, vol. 30, 1993.
- [2.14] Hamamatsu Photonics. Characteristics and use of infrared detectors. Available: http://sales.hamamatsu.com/assets/applications/SSD/Characteristics_and_use_of_infrared_detectors.pdf
- [2.15] C.-C. Hsieh, C.-Y. Wu, F.-W. Jih, and T.-P. Sun, "Focal-plane-arrays and CMOS readout techniques of infrared imaging systems," Circuits and Systems for Video Technology, IEEE Transactions on, vol. 7, pp. 594-605, 1997.

- [2.16] D. M. Rowe, *Modern Thermoelectrics*. London: Prentice Hall, 1983.
- [2.17] A. Rogalski, "Optical detectors for focal plane arrays," *Opto-Electronics Review*, vol. 12(2), pp. 221-245, 2004.
- [2.18] H. Jerominek, F. Picard, and D. Vincent, "Vanadium oxide films for optical switching and detection," *Optical Engineering*, vol. 32, pp. 2092-2099, 1993.
- [2.19] A. Rogalski, "Recent progress in infrared detector technologies," *Infrared Physics & Technology*, vol. 54, pp. 136-154, 2011.
- [2.20] V. Y. Zerov, V. G. Malyarov, I. A. Khrebtov, Y. V. Kulikov, I. I. Shaganov, and A. D. Smirnov, "Uncooled membrane-type linear microbolometer array based on a VOx film," *J. Opt. Technol.*, vol. 68, p. 428, 2001.
- [2.21] F. Niklaus, C. Vieider, and H. Jakobsen, "MEMS-based uncooled infrared bolometer arrays: a review," vol. 6836, p. 68360D, 2007.
- [2.22] M. Kohin and N. R. Butler, "Performance limits of uncooled VOx microbolometer focal plane arrays," vol. 5406, pp. 447-453, 2004.
- [2.23] L. Pardo, J. Ricote, R. Jiménez, and B. Jiménez, "Pyroelectricity in Polycrystalline Ferroelectrics," in *Multifunctional Polycrystalline Ferroelectric Materials*. vol. 140, ed: Springer Netherlands, pp. 573-616, 2011.
- [2.24] S. Tadigadapa and K. Mateti, "Piezoelectric MEMS sensors: state-of-the-art and perspectives," *Measurement Science and Technology*, vol. 20, p. 092001, 2009.
- [2.25] M. Paul, "Micromachined infrared detectors based on pyroelectric thin films," *Reports on Progress in Physics*, vol. 64, p. 1339, 2001.
- [2.26] S. B. Lang, *Pyroelectricity: From Ancient Curiosity to Modern Imaging Tool* vol. 58: AIP, 2005.
- [2.27] DIAS Infrared GmbH. Available: <http://www.dias-infrared.com/>
- [2.28] D. D. L. Wijngaards, S. H. Kong, M. Bartek, and R. F. Wolffenbuttel, "Design and fabrication of on-chip integrated polySiGe and polySi Peltier devices," *Sensors and Actuators A: Physical*, vol. 85, pp. 316-323, 2000.
- [2.29] Dexter Research Center. Data sheets and application Notes. Available: <http://www.dexterresearch.com/>
- [2.30] S. Gaalema, S. V. Duyne, J. L. Gates, and M. C. Foote, "Thermopile detector radiation hard readout," vol. 7780, p. 778002, 2010.
- [2.31] A. Levin, W. Baer, S. Harrigan, J. Zewicke, and R. S. Toth, "Thermopile linear array for spectroscopy applications," vol. 7680, pp. 76800J-8, 2010.

- [2.32] M. C. Foote, T. R. Krueger, J. T. Schofield, D. J. McCleese, T. A. McCann, E. W. Jones, and M. R. Dickie, "Space science applications of thermopile detector arrays," vol. 4999, pp. 443-447, 2003.
- [2.33] U. Dillner, E. Kessler, V. Baier, A. Berger, T. Eick, D. Behrendt, and H. Urban, "A 64-pixel linear thermopile array chip designed for vacuum environment," Proceedings of IRS², pp. 295-300, 2006.
- [2.34] Carinthian Tech Research AG. Available: <http://www.ctr.at/>
- [2.35] M. Kraft, A. Kenda, T. Sandner, and H. Schenk, "MEMS-based compact FT-spectrometers - a platform for spectroscopic mid-infrared sensors," Sensors, 2008 IEEE, pp. 130-133, 2008.
- [2.36] Wilks Enterprise Inc. Available: <http://www.wilksir.com/>
- [2.37] ICx Technologies™. Available: <http://photonics.icxt.com/>
- [2.38] InfraTec GmbH. Available: <http://www.infratec.de/>

Design and Analysis of the Thermo-Electric Detector: Radiant-to-Thermal Effect

3

3.1 Introduction

Since the thermal detector array is an essential component in the *IR* microspectrometer, as is discussed in the previous chapter, optimization approaches should be provided in order to efficiently design a suitable thermopile detector array. A thermopile based detector is an optical tandem transducer [3.1]. Radiant flux is first converted into heat and subsequently into an electrical signal via the selected thermo-electric effect. This chapter emphasizes particularly the optical to the thermal conversion. Efficient heating of the absorber requires a high absorption coefficient in the spectral range of interest. A switchable thin-film absorber using materials composed of magnesium and titanium to achieve on/off function is reported [3.2]. However, the materials used in the *IC* compatible process, such as polysilicon (*PolySi*), silicon oxide (SiO_2) and silicon nitride (*SiN*), have very low absorption in the near *IR* range. For this reason an absorber should be implemented for the purpose of improving sensitivity. According to *IR* detection and chip technology, the perfect absorber for the thermal detector should satisfy the requirements as below [3.3]:

- High and constant absorption over a wide spectral range
- Minimum heat capacity

- High thermal conductivity
- High-term stability and reproducibility

Several solutions are available, each with specific advantages and disadvantages.

Absorbers discussed in this chapter are: 1. Based on a black layer with a special attention to carbon nanotubes (*CNTs*). 2. Absorbers realized by metamaterial as a new type of absorber is proposed. 3. The impedance matching absorber composed of several thin film layers. The particular advantage of the third technique is the combination with clean-room processing after the deposition of absorber.

3.2 Opto-thermal conversion

3.2.1 Metal black absorber

The use of deposits of metallic smokes as an absorber for *IR* detectors was first demonstrated in the 1930s [3.4]. The process has remained relatively unchanged until the 1950s [3.5]. Measurements with a number of metallic smokes indicated that gold (*Au*) "black" might have a high ratio of (*IR* absorption/thermal mass). This is an important property for *IR* detectors designed to respond to rapid variations of incident radiation. The absorbance is high in the spectral range close to the resonance wavelength where the *Au* particles cause strong scattering or absorption, which depends on the size of the *Au* particles. The absorption can be more than 90% in the mid *IR* spectral range.

Generally, the gold black layer is fabricated by evaporation. The quality of the gold black obtained by evaporating gold in an inert atmosphere relies upon other issues such as: the gas pressure, the purity of the gas, the distance between the source and the surface of deposition, the mass of the detector, the rate of gold evaporation, and the rate of heat conduction from the detector element [3.6]. The resulting gold black layer is porous and thus fragile and may be crushed or scratched easily and removed by blowing air. It is also destroyed when wetted and is difficult to produce at constant quality. Recent progress in the fabrication of black gold has demonstrated to deposit gold black on a thin, freestanding,

pyroelectric detector [3.6] and to be patterned by a lift-off technique in an *IR* focal plane array [3.7]. Besides the low pressure evaporation process, the high-intensity femtosecond laser pulses [3.8] has been shown to be a suitable tool for surface structuring achieving the gold black as shown in the Figure 3-1.

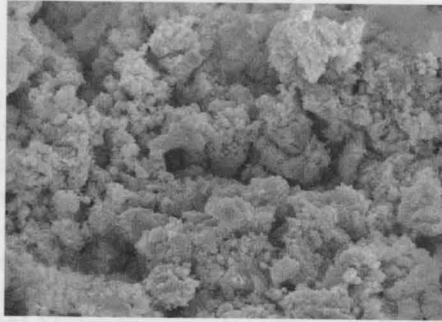


Fig. 3-1. SEM image of the structural surface of black Au [3.8].

One disadvantage of using porous metals depends on the fact that their absorption coefficient is in good approximation proportional to their mass per unit area. This results in a relatively high thickness needed for a high absorption, thermal mass and conductance on the device [3.9]. Another major shortcoming is the *IC* compatibility infringement. The wafer is typically not allowed to re-enter the clean room after sputtering with black *Au*, hence, it cannot be further processed, for instance for thin-film encapsulation. Nevertheless, gold black has provided broad and uniform absorptance, relatively low thermal mass represented as the material density shown in Table 1.

TABLE 1. Comparison of density of materials.

Gold [kg/m ³]	Gold Black [3.10] [kg/m ³]	Poly Silicon [kg/m ³]	Silicon Nitrite [kg/m ³]
19300	60	2330	3100

There are alternatives to gold black for *IR* detector absorber coatings. Proprietary paints such as 3M black and Catalac black are useful and appropriate for some applications requiring a very wide spectral response [3.11]. Other metal blacks such as silver black have been used to enhance the *IR* sensitivity of pyroelectric detectors. Silver black is comparable to gold-black; the spectral response of pyroelectric detectors coated with silver-black reduces by

approximately 2% as the wavelength decreases from 2.5 to 1 μm . Platinum-black is deposited using a wet (electrochemical) process and is being used as a coating for pyroelectric detectors by GEC Marconi¹.

3.2.2 Carbon Nanotubes-based absorber

The carbon nanotube (*CNT*) based absorber can be designed and grown to feature high absorption efficiency in the terahertz and near *IR* band, because of the carbon π band's optical transitions, and is for this reason used in many conventional black materials, such as carbon black and graphite [3.12]. The absorptivity is up to 0.85 with moderate reflection at the air-dielectric interface [3.13]. The absorptivity can be even higher by using nano-structures [3.14]. Optical thin films consisting of nanorods have a lower refractive index and, consequently, a lower reflectance than dense materials [3.15]. Other advantages are high thermal conductivity and damage resistance, which make them promising candidates as coatings for thermal detectors [3.16].

Previous reports on *CNT* coatings, use either single wall [3.17] or multiwall [3.18] structures, as an alternative for metal-black coatings. These 2 μm thick nanotube coatings show a comparable high and spectrally homogeneous absorption depth ranging from 600 to 1800 nm. However, the deposition technique requires that the detector is heated up to 1175 $^{\circ}\text{C}$ which exceeds the Curie temperature of the pyroelectric material used for high performance detectors, and also makes it incompatible with photolithographic patterning processes. Moreover the absorption typically has a dip at around 2.5 μm [3.19].

1. GEC Marconi Materials Technology Ltd, Caswell, Towcester, Northants NN12 8EQ, UK

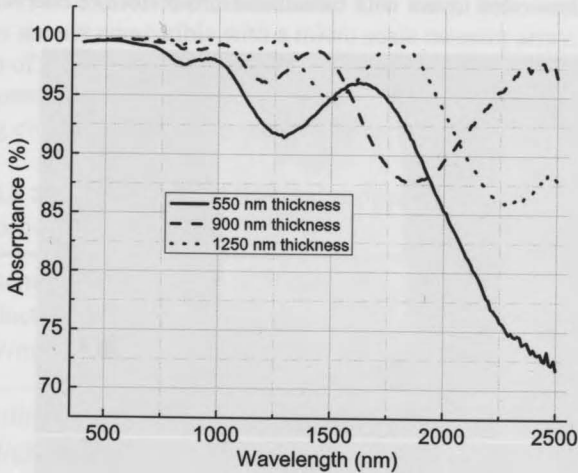


Fig. 3-2. Measured spectral absorptance of CNT with different thickness.

The original contribution projected in this thesis is based on vertically aligned CNTs, which can be deposited directly on metal catalyst coated substrates via Chemical vapour deposition (CVD). CVD is a technique used in semiconductor industry to deposit thin films of highly pure material on a substrate. This is done by thermal decomposition of gases in a reactor chamber at a certain pressure and temperature [3.20]. The merit of using metal catalyst by CVD is to grow the vertically aligned CNT forest as shown in Figure 3-3 and was grown in DIMES [3.21].

A forest of vertically aligned CNTs behaves very similarly to a blackbody [3.22] since it shows a comparable high and spectrally homogeneous absorptance ranging from 0.2 to 200 μm wavelength. Low reflectance is achieved by having the refractive index of material between the CNTs and air satisfy Fresnel's law. It is difficult to achieve low reflectance in case of a solid materials, which typically have an index of relatively higher than 1.4.

A vertically aligned CNTs forest has a low refractive index and can resemble an aerogel due to low density (high sparseness) and flat top surface. Therefore, the film porosity provides the adjustment between the refractive index

of air and the refractive index of substrate [3.23]. It can be used for the fabrication of graded refractive-index layers with broadband anti-reflective characteristics as well.

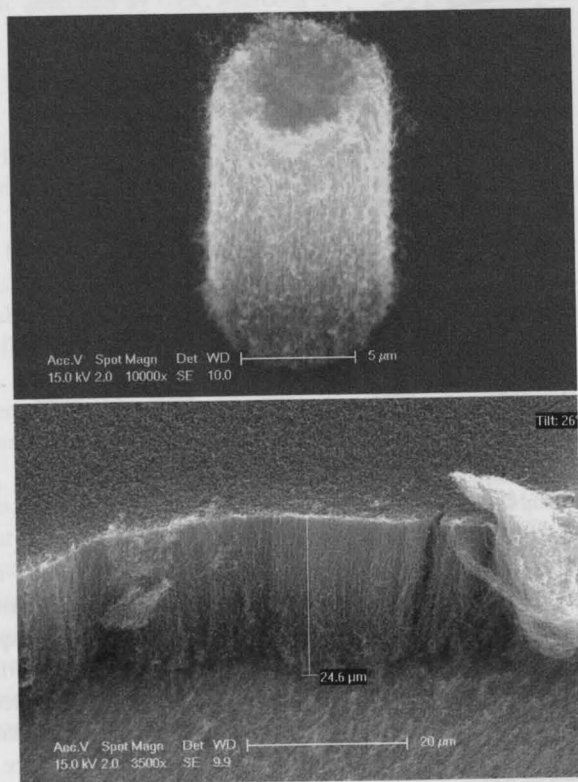


Fig. 3-3. (a) SEM images of nanotubes grown on 3 nm Fe at 600 °C patterned by Lift-off process (b) Growth at 650 °C [3.21].

Table 2 lists the properties of *CNTs* as compared to conventional black coatings [3.17]. The table indicates that *CNTs* can be a promising candidate as an absorber for *IR* applications. Up to date, most reports concentrate on the characterization of *CNT* film on bulk substrate. A suspended single-wall *CNTs* based bolometer was reported [3.24]. High growing temperature and non-uniform spectral response are still issues. The vertically aligned *CNTs* growth on Lithium Tantalate, the most popular material for pyroelectric detectors, is also investigated [3.25]. The 16 μm thick film has a spectrally constant absorptance from the

visible to the *IR* wavelength range. The issues are still the high growth temperature and millimeter dimensions. The thick film and relatively large dimensions are not compatible with a micro scale detector array. Furthermore the integration of *CNT* deposition with a *CMOS-MEMS* process is still at its infancy. Another potential advantage of *CNTs* presently investigated is the use in energy scavenging on the condition that the *CNT* is doped [3.26].

TABLE 2. Comparison of thermal properties of various coatings for absorber [3.17].

Thermal conductivity [W/mK]	CNTs	100-1000
	Black Au	0.03
	Black Carbon	0.003
Specific heat [J/gK]	CNTs	600
	Black Au	130
Damage threshold heat [mJ/cm ²]	CNTs	547
	ceramic pyro	250
	Ni on Cu, Ni on Sapphire	150
	Black Au	38

3.2.3 Metamaterials as an absorber

A newly developed narrowband *IR* absorber using metamaterials is presented here. The metamaterial is defined as a substance that acquires its electromagnetic properties from embedded physical structures instead of from its chemical composition. Methods for tuning the perfect absorber to absorb at different frequencies will be explored in the following section. The implementation of the narrowband metamaterial absorber in *IR* spectroscopy is discussed at the end of this section.

Metamaterials can be defined as follows: a composite material whose micro (or nano) structure is artificially designed such that the effective macroscopic response of the structure to a given excitation is not readily encountered in nature [3.27]. It is fascinating because the "unusual" electromagnetic characteristic can be tailored to meet requirements by design. An example is a design with a

negative index of refraction, which is interesting in a variety of optical applications such as lenses, beam steerers, couplers, modulators, band-pass filters and invisible cloaks. Similar to matter which is made up of atoms, the metamaterial is made up of unit-cells and known as meta-atom [3.28]. By using artificially designed and fabricated structural units, the concept can be scaled up similar to conventional continuum materials. A prerequisite in an electromagnetic metamaterial is that a unit-cell should be much smaller than the driving wavelength of light. Some reports research further as to propose a rule of thumb to clearly discriminate metamaterial devices via an effective homogeneity condition [3.29]:

$$p \leq \lambda/4 \quad (3-1)$$

where p is the average size of a unit cell.

With all the potential applications discussed above, what can we do with metamaterial on the *IR* microspectrometer? The answer is to thoroughly utilize the imperfection of metamaterial and accurately turn out the perfect absorber implemented on the thermal *IR* detector. The recent study discloses the trade-off between bandwidth and loss in the metamaterial. This is a non-essential result for the conventional application, like a superlens. However, the customized design can cause a high loss and thus yield a narrow band absorber. This can be used in the thermal detector in the *LVOF* based microspectrometer. The requirements and issues to achieve a good *IR* metamaterial absorber are discussed in following subsections.

3.2.3.1 Metamaterial & Photonic crystal

What is the difference between metamaterials and photonic crystals, since both of them can provide negative refraction? In general metamaterials are realized by metallic structures to provide a negative permittivity and use resonant structures to supply a negative permeability (hence constitute inductor-capacitor tank circuits) with a scale much smaller than the wavelength to provide a negative refraction, while photonic crystals exhibit negative refraction as a consequence of bandfolding effects [3.30]. Moreover, photonic crystals can be described as classical diffractive components, whose cellular dimensions are typically integer multiples of a half-wavelength ($p \cong n \times \lambda/2$). Consequently, it cannot be equivalent to a medium with single value refractive index [3.31].

3.2.3.2 The refractive index

Many laws and equations of electrodynamics and optics apply. The case of non-magnetic materials with permeability $\mu = 1$ is considered here. Therefore, the well known Snell's law expresses the refractive index n as:

$$n = \sqrt{\varepsilon} \quad (3-2)$$

where the ε is the relative permittivity of material.

When the magnetic response of the metamaterial needs to be included, the refractive index of an electromagnetically sensitive material depends on both the permittivity and the permeability, through the relation:

$$n = \pm \sqrt{\varepsilon\mu} \quad (3-3)$$

The refractive index is negative when both permittivity and the permeability are smaller than zero. However, how is it related to the absorption of light in the material? The permittivity and the permeability becomes complex in lossy media and can be characterized as an effective medium through [3.32]

$$\varepsilon = \varepsilon' + i\varepsilon'', \mu = \mu' + i\mu'' \quad (3-4)$$

In a metamaterial, the imaginary part of above equation can be manipulated [3.33]. This enables the creation of loss components of the optical constants (ε'' and μ'') and draw out much potential for the creation of exotic and useful materials as an absorber.

3.2.3.3 The impedance matching

The Fresnel equations (or Fresnel conditions) describe the behaviour of light when moving among media of differing refractive indices. The reflectance R of a material described by the macroscopic form of Maxwells' equations in case of an angle of incidence θ from the normal surface, for both transverse electric (TE) and transverse magnetic (TM) polarizations to vacuum are determined by the modified conventional Fresnel equations. Since μ is not equal to one, both ε and μ

contribute to R :

$$R_{TE} = \frac{\left| \frac{\cos \theta - \sqrt{\epsilon\mu - \sin^2 \theta}}{\mu} \right|^2}{\left| \frac{\cos \theta + \sqrt{\epsilon\mu - \sin^2 \theta}}{\mu} \right|^2} \quad (3-5)$$

$$R_{TM} = \frac{\left| \frac{\epsilon \cos \theta - \sqrt{\epsilon\mu - \sin^2 \theta}}{\epsilon \cos \theta + \sqrt{\epsilon\mu - \sin^2 \theta}} \right|^2}{\left| \frac{\epsilon \cos \theta + \sqrt{\epsilon\mu - \sin^2 \theta}}{\epsilon \cos \theta + \sqrt{\epsilon\mu - \sin^2 \theta}} \right|^2} \quad (3-6)$$

Therefore, minimum reflectance is achievable at normal incidence if the absorber material impedance $Z = \sqrt{\mu / \epsilon}$ is matched to that of vacuum, i.e., when $\epsilon = \mu$. Assume the transmission of the metamaterial is (almost) zero, the maximum of absorption is reached. Since the thick metal is usually at the bottom of metallic metamaterial stacks, the zero transmission is valid. Therefore, the two criteria for a perfect absorber using metamaterial are:

- Maximize the imaginary (lossy) part of refractive index
- Impedance matching required, i.e. $\epsilon = \mu$

3.2.3.4 The resonance behavior

An engineered metamaterial with simultaneous negative electric permittivity and negative magnetic permeability can exist without violating any physical law. Consequently metamaterial resonator acts as an electric- LC resonator [3.34] supplying electric coupling to the incident electric (E) field within gaps of the structure. The magnetic coupling is created by the anti-parallel currents between the upper metallic cell and the bottom metal film response to the incident Magnetic (H) field.

For appropriately modulating the geometrical parameters (to meet the two absorbing criteria), the electric and magnetic dipole resonances can be well overlapped in the given frequency range, providing the ability to almost completely absorb the electric and magnetic energy. The bandwidth characteristic of resonator is in general not narrow. However, this behavior can be used to alleviate some problems, for instance, the out of band signal of $LVOF$ optical filter.

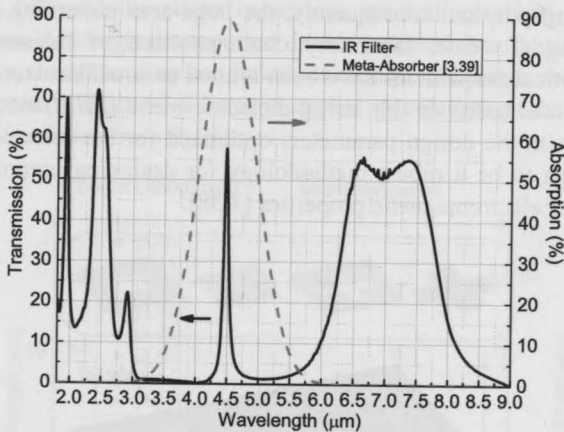


Fig. 3-4. Optical behavior of LVOF IR filter combined with Meta-absorber. The system is illustrated in Figure 4-17 on page 89.

3.2.3.5 Types of metamaterials

There have been several reports of research demonstrating the feasibility of metamaterial absorbers in which the loss portions of the optical constants have been sufficiently exploited rather than the real ones. In the early study phase of metamaterial the use of split-ring resonators (*SRR*), which are basically sub-wavelength sized electromagnets, to effectively generate a negative permeability was purposed [3.35]. When the incident magnetic field is polarized perpendicular to the plane of the rings array, resonating currents are induced in the loop which emulate a magnetic dipole. For the electric field, the negative permittivity is exhibited by the use of the noble metals at excitation frequencies below their intrinsic electric plasma frequency (ω_{pe}). The implementation of *SRR* is reported and demonstrated with such effects at microwave and terahertz frequencies [3.33][3.36].

Extending the operating range of metamaterials based on *SRR* [3.35] to *IR* wavelengths necessarily involves complicated fabrication since nanoscale metallic structures are required to yield resonances. The sub-micron technology to pattern the nano structures can be realized by electron beam (*E beam*)

lithography or focused ion beam milling (FIB) [3.37]. Both techniques suffer from low throughput, and consequently, the large-area patterning is costly and time consuming. To date, laboratory demonstrations of metamaterial based absorbers at optical frequencies have been limited to small structures. Instead of SRR, the structures based on thin metal-dielectric-metal (MIM) stacks illustrated in Figure 3-5 with the design parameters optimized for the selected wavelength has been proven to be a robust methodology for designing complex structures with customized electromagnetic properties [3.38].

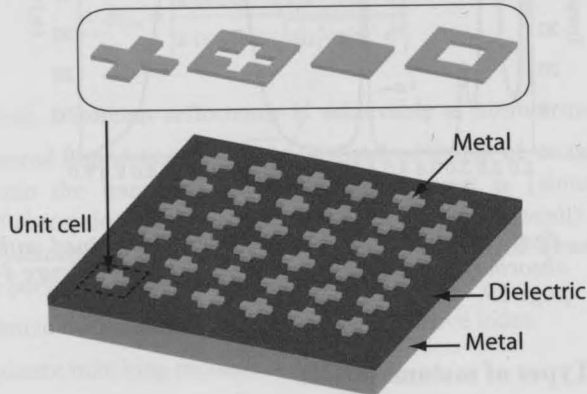


Fig. 3-5. Illustration of metal-dielectric-metal (MIM) stacks meta-absorber. The result of different shape of unit cell needed to be further investigated.

3.2.3.6 Angle dependence & Polarization

As discussed before, scaling up in the frequency domain requires scaling down in the spatial domain. In the nano structure case, the prominent surface plasmonic response of the metal must also be carefully considered in the design. This effect can be efficiently excited in noble metals, such as gold, silver, and copper, due to their free electron like behavior. The requirement for achieving wide-angle absorption is the sub-wavelength unit cell. Recent numerical simulations have found that absorption rapidly drops with incident angle when the unit cell is too large (in the millimeter range) [3.33]. A polarization insensitive metamaterial absorber is achieved by integrating symmetric electric and magnetic resonators into the unit cell with nano structures.

Gold has been widely explored as a suitable metamaterial, however, it may

introduce *IC*-compatibility issues. A recent report [3.39] has demonstrated the use of aluminium (*Al*) metallic stacks to achieve spectral selectivity as well as the high absorption. Although the reported device fabricated in a non-*CMOS* process, the absorption bandwidth of each pixel is large, which makes it a promising approach. Figure 3-6 lists the central wavelength of the meta-absorber versus the unit cell size from literatures.

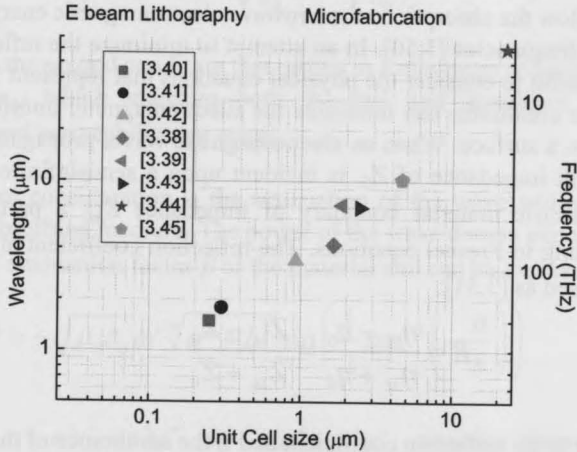


Fig. 3-6. Resonant frequency of the meta-absorber versus unit-cell size.

3.2.4 Microwave absorber

This section introduces a microwave-based absorber with good absorption in *IR* range, while the wafer can remain in a *CMOS* process sequence. The application of microwave absorbing materials has been extensively implemented in the electronic industries, in which communication technologies at microwave frequencies have driven the development and utilization of absorbers and frequency selective surfaces. The principle can be extended into infrared range. The idea of the thin-film *IR* absorber was first calculated in 1956 by solving the Maxwell equations [3.46]. The best absorption can be realized by matching the absorber to the air impedance interface, which is equal to $377 \Omega/\text{sq}$ [3.47]. This was verified using microwave theory [3.48]. Recently, this type of thin-film absorber was applied to a bolometer for use in the far-*IR* spectral range [3.49]. The conditions to achieve the maximum absorption in a spectral range of interest are introduced. The metal/dielectrics/metal absorbing structures are designed,

simulated and the results are experimentally validated.

3.2.4.1 Minimized reflection

Microwave absorbers are typically designed for reflectivity minimization by alternating shape, structure, and the permittivity and permeability of existing materials to allow the absorption of microwave electromagnetic energy at discrete or broadband frequencies [3.50]. In an attempt to minimize the reflection from a surface it is useful to consider the physical equations that represent the reflection process. Three conditions can minimize the Electromagnetic interference (EMI) reflection from a surface. When an electromagnetic wave, propagating through a free space with impedance of Z_0 , is incident upon a semi-infinite dielectric or magnetic dielectric material boundary of impedance Z_M , a partial reflection occurs according to Fresnel equations. The reflection coefficient at the interface can be expressed as [3.51]:

$$R = \frac{\eta_M - \eta_0}{\eta_M + \eta_0} = \frac{Z_M - Z_0}{Z_M + Z_0} \quad (3-7)$$

where R is the reflection coefficient and η the admittance of the propagating medium. The admittance in the equation can be replaced with the intrinsic impedance ($Z = 1/\eta$). The reflection coefficient towards zero when $\eta_M = \eta_0$, which means the material is impedance matched to the incident medium. The intrinsic impedance of free space results as:

$$Z_0 = \frac{E}{H} = \sqrt{\frac{\mu_0}{\epsilon_0}} \approx 377\Omega \quad (3-8)$$

where E and H are the electric and magnetic field vectors and ϵ_0 and μ_0 are the permeability and permittivity of free space.

Perfect impedance matching can also be achieved if the relative electric permittivity and the relative magnetic permeability are equal, which can be

demonstrated by rewriting Eqn (3-7) as:

$$R = \frac{\frac{Z_M}{Z_0} - 1}{\frac{Z_M}{Z_0} + 1}, \quad \frac{Z_M}{Z_0} = \frac{\sqrt{\frac{\mu_M}{\epsilon_M}}}{\sqrt{\frac{\mu_0}{\epsilon_0}}} = \frac{\sqrt{\frac{\mu_r \mu_0}{\epsilon_r \epsilon_0}}}{\sqrt{\frac{\mu_0}{\epsilon_0}}} = \sqrt{\frac{\mu_r}{\epsilon_r}} \quad (3-9)$$

It gives the second condition that results in a minimum reflection coefficient when $\epsilon_M = \mu_M$ which indicates both the real and imaginary parts of the permittivity and permeability are equal.

The third consideration is the attenuation of the wave while it propagates through the absorbing medium. The power of the wave decays exponentially with distance. The attenuation factor β of the material and can be expressed as [3.52]:

$$\beta = -\sqrt{\mu_0 \epsilon_0} \omega^{1/4} \sqrt{a^2 + b^2} \sin \left(\frac{1}{2} \tan^{-1} \left(-\frac{a}{b} \right) \right) \quad (3-10)$$

where $a = \epsilon' \mu' - \epsilon'' \mu''$, $b = \epsilon' \mu'' - \epsilon'' \mu'$, complex form ϵ and μ as expressed in Eqn (3-4). The attenuation factor β should be large in order to get a large attenuation in thin layer of absorbing material. This means that ϵ and μ are large as well. However, this condition contradicts the first condition Eqn (3-7) and needs to be compromised because large values of permittivity and permeability would cause a large reflection coefficient.

To best satisfy these three conditions for perfect absorption with a layer of minimum thickness, resonant absorbers are formed through tuned or quarter-wavelength absorbing materials structured to absorb electromagnetic wave energy at multiple frequencies. Resonant materials generally include Dallenbach layers, Salisbury screens, and Jaumann layers [3.52]. Since only Salisbury screens have the potential to be implemented into the detector array in IR range, it is introduced and discussed step by step.

The Salisbury screen consists of a resistive sheet, an optical distance and a reflector as illustrated in Figure 3-7. The optical distance is of an odd multiple of quarter wavelengths ($\lambda/4$) of incident wave. The resistive sheet is as thin as possible with a resistance of 377Ω , matching that of free space. Thus half of the

incident wave is absorbed and the other half is transmitted. The transmitted wave is reflected by the metal, i.e. reflector with the electrical thickness of a quarter wavelength. Then the phase of the transmitted and reflected wave has 180° or π phase difference which causes cancellation by destructive interference.

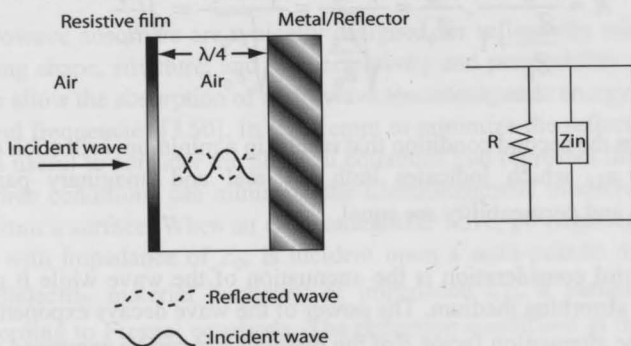


Fig. 3-7. Salisbury screen and its equivalent circuit.

The Salisbury screen can also be expressed in an equivalent circuit by the transmission line theory. The infinitesimally thin resistive film is placed on the surface of dielectric substrate of which thickness is quarter wavelength ($\lambda/4$) in front of a perfectly reflecting metal plate. The structure is equivalent to the parallel circuit composed of sheet resistance of the film (R) and the input impedance of the dielectric substrate (Z_{in}) at a distance $\lambda/4$ in a short circuited transmission line which is given by Eqn (3-11),

$$Z_{in} = Z_0 \sqrt{\frac{\mu_r}{\epsilon_r}} \tanh\left(\frac{i2\pi d}{\lambda_0} \sqrt{\mu_r \epsilon_r}\right) \quad (3-11)$$

where λ_0 is the wavelength in free space and d is the thickness.

At distance $\lambda/4$, electric field is maximum and magnetic field is zero, which makes Z_{in} be infinite as identified in Eqn (3-11). Then the total impedance is equal to sheet resistance of film R by:

$$Z = \frac{R \times Z_{in}}{R + Z_{in}} = R \quad (3-12)$$

Hence, the Salisbury screen works as a perfect absorber for normal

incidence when the spacer thickness is equal to an odd multiple of the quarter wavelength. Similarly, the Salisbury screen can operate as a perfect reflector for spacer thicknesses that are multiples of half wavelengths. This effect occurs only at a single frequency. For this reason, Salisbury screens in their basic form have found little practical usage [3.52].

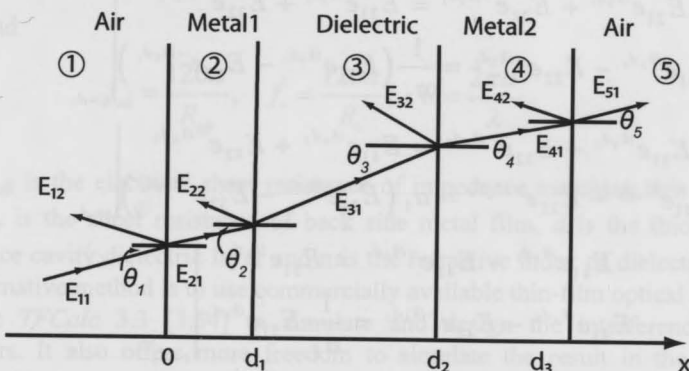


Fig. 3-8. Representation of waves travelling in the metal/dielectric/metal layers in free space [3.46].

3.2.5 Design of the absorber

Commonly, then interferometric thin film absorber includes three stack of layers: impedance matching thin metallic film, resonance cavity and back metallic film layer as being reflector. The system is shown in Figure 3-8. The propagation constants for the thin-films and medium are:

$$k_1 = k_5 = \frac{2\pi}{\lambda}, \quad k_2 = \frac{2\pi}{\lambda}(n_2 + ik_2), \quad k_3 = \frac{2\pi}{\lambda}n_3, \quad k_4 = \frac{2\pi}{\lambda}(n_4 + ik_4) \quad (3-13)$$

Assuming the electric field E is normal to the plane of incidence, the equations including the incident and reflected wave in the various region can be

$$\left[\cos^2(\lambda + \alpha) + \sin^2\left(\lambda + \frac{(1+\lambda)\lambda}{\alpha}\right) \right] \frac{1}{\sin^2} = (\lambda)k$$

expressed as below by applying the boundary conditions [3.46]:

$$\begin{aligned}
 & \left. \begin{aligned} E_{11} + E_{12} &= E_{21} + E_{22} \\ E_{11} - E_{12} &= a_1(E_{21} - E_{22}) \end{aligned} \right|_{x=0} \\
 & \left. \begin{aligned} E_{21}e^{ik_2d_1} + E_{22}e^{-ik_2d_1} &= E_{31}e^{ik_3d_1} + E_{32}e^{-ik_3d_1} \\ E_{21}e^{ik_2d_1} - E_{22}e^{-ik_2d_1} &= \frac{1}{a_2}(E_{31}e^{ik_3d_1} - E_{32}e^{-ik_3d_1}) \end{aligned} \right|_{x=d_1} \\
 & \left. \begin{aligned} E_{31}e^{ik_3d_2} + E_{32}e^{-ik_3d_2} &= E_{41}e^{ik_4d_2} + E_{42}e^{-ik_4d_2} \\ E_{21}e^{ik_2d_1} - E_{22}e^{-ik_2d_1} &= a_3(E_{31}e^{ik_3d_1} - E_{32}e^{-ik_3d_1}) \end{aligned} \right|_{x=d_2} \\
 & \left. \begin{aligned} E_{41}e^{ik_4d_3} + E_{42}e^{-ik_4d_3} &= E_{51}e^{ik_5d_3} \\ E_{41}e^{ik_4d_3} - E_{42}e^{-ik_4d_3} &= \frac{1}{a_4}E_{51}e^{ik_5d_3} \end{aligned} \right|_{x=d_3}
 \end{aligned} \tag{3-14}$$

where

$$a_1 = \frac{k_2 \cos \theta_2}{k_1 \cos \theta_1}, \quad a_2 = \frac{k_2 \cos \theta_2}{k_3 \cos \theta_3}, \quad a_3 = \frac{k_4 \cos \theta_4}{k_3 \cos \theta_3}, \quad a_4 = \frac{k_4 \cos \theta_4}{k_5 \cos \theta_5} \tag{3-15}$$

The transmission T , reflection R and absorption A coefficient can be expressed by:

$$\begin{aligned}
 T &= \left| \frac{E_{51}}{E_{11}} \right|^2; \\
 R &= \left| \frac{E_{12}}{E_{11}} \right|^2; \\
 A &= 1 - R - T;
 \end{aligned} \tag{3-16}$$

Hence, the normal spectral absorbance $A(\lambda)$ of the layer can be calculated as [3.53]:

$$A(\lambda) = \frac{4}{Dn^2} \left[\left(\frac{f_{ab}(f_r+1)^2}{n^2} + f_r \right) \sin^2 \theta + (f_{ab} + f_r) \cos^2 \theta \right] \tag{3-17}$$

where

$$D = \left[\frac{(f_{ab} + 1)(f_r + 1)}{n^2} + 1 \right]^2 \sin^2 \theta + \left[\frac{f_{ab} + f_r + 2}{n} \right]^2 \cos^2 \theta \quad (3-18)$$

and

$$f_{ab} = \frac{120\pi}{R_{ab}}, \quad f_r = \frac{120\pi}{R_r}, \quad \theta = \frac{2\pi d}{\lambda} \quad (3-19)$$

R_{ab} is the electrical sheet resistance of impedance matching thin metallic film, R_r is the sheet resistance of back side metal film, d is the thickness of resonance cavity dielectric layer and n is the refractive index of dielectric layer. An alternative method is to use commercially available thin-film optical software package *TFCalc* 3.3 [3.54] to simulate and design the interference based absorbers. It also offers more freedom to simulate the result in the case of complex structure or stack layers. Therefore, it has been simulated and optimized by *TFCalc*.

TABLE 3. Different metallic thin films for absorber [3.55].

Metal	Thickness (nm)	Sheet resistance (Ω)
Titanium(evap.)	4	430-480
Platinum/Titanium nitride (sputt.)	2/6	190-260
Nickel	3.6	350-377
Titanium nitride (sputt.)	18	298-395

There are some choices to apply the metallic film for impedance matching thin layer as shown in Table 3. To maintain the *CMOS* compatibility, metals which would induce trap levels in silicon are not considered. Although Titanium (*Ti*) could have long term reliability problems because of the oxidation, *Ti* is chosen as the metallic layers of the absorber. The optical properties of *Ti* up to 1.2 μm are measured by using ellipsometry on a test sample. Figure 3-9 shows the measured refractive index and extinction coefficient of *Ti* for wavelengths up to

1.2 μm . The properties are in agreement with the literature [3.56].

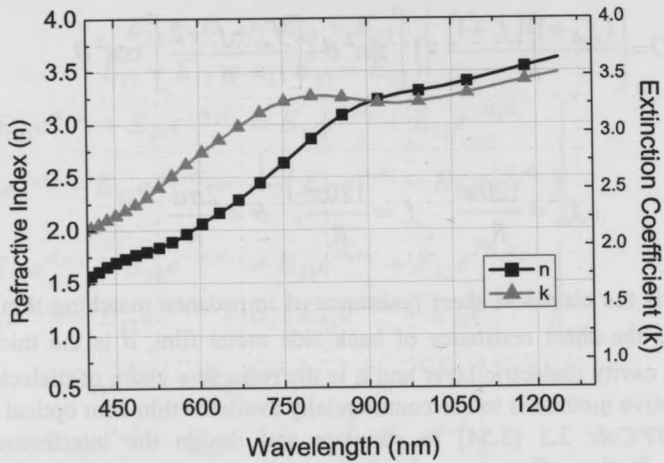


Fig. 3-9. Optical properties of sputtered Ti.

The absorber consists of one dielectric centre layer with thin-film metallic layers on either side as similar to Salisbury screens. Two sets of absorbers have been designed and fabricated, one with SiO_2 and one with silicon carbide (SiC) as spacing layer. Absorbers based on SiO_2 have a relatively thick lower Ti layer of 300 nm thickness, whereas the upper layer is much thinner and taken as the variable in the experiments. The reason for selecting such a thin thickness is to try to match the impedance of free space. The maximum absorption wavelength can be well controlled by changing the thickness of the spacing. The thickness variation of the thick lower layer does not significantly affect the wavelength response of the absorber since it is performed as a reflector. Designing the center layer optical thickness at a quarter of the resonance wavelength at 1.2 μm (i.e. SiO_2 layer thickness is 200 nm), while using 4 different values for the thin Ti layer thickness, results in the simulated absorption as shown in Figure 3-10.

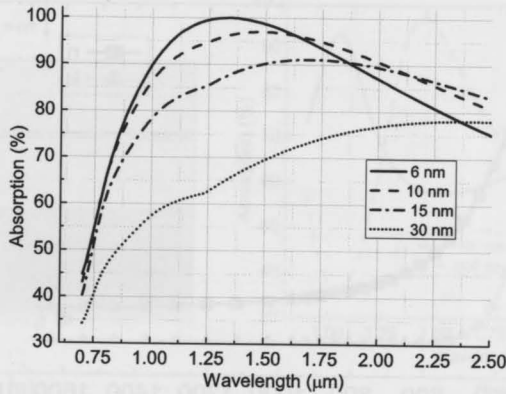


Fig. 3-10. Simulation results of absorption with different values of the thickness of the Ti free space impedance matching layer.

The above figure indicates that a maximum absorption is achieved with the 6 nm Ti layer at 1.3 μm when using actual optical properties. The shift of maximum wavelength from 1.2 μm to 1.3 μm with a thicker Ti layer thickness is due to the phase shift in the thin Ti layer. The maximum absorption wavelength also differs for other absorbers for the same reason.

Plasma Enhanced Chemical Vapour Deposition (PECVD) SiC has also been used as the dielectric spacing layer. SiC is preferred because of the high resistance to HF attack during sacrificial etching. Another advantage of using SiC for the spacing layer is the decreased process complexity, since it is also used for the protective coating. Figure 3-11 shows the optical properties of PECVD SiC from literature [3.57].

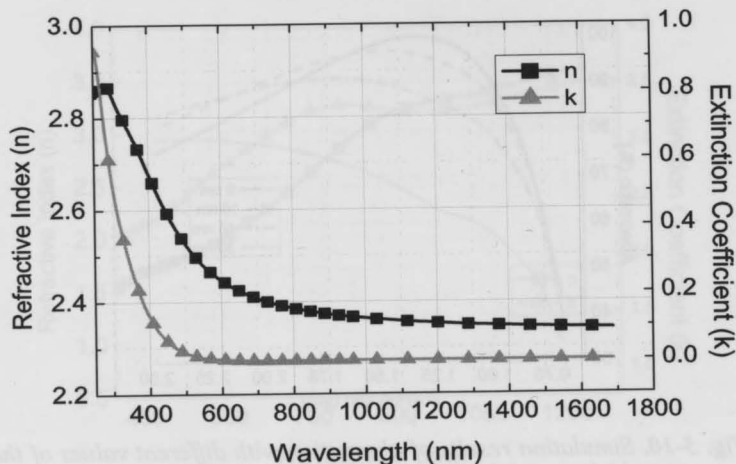


Fig. 3-11. Optical properties of PECVD SiC.

The thickness of the *Ti* layer, which is the reflector in the absorber stacks, is limited to 100 nm by practical fabrication considerations. To protect the top thin *Ti* layer, another *SiC* layer is introduced and covers the entire absorber stacks. Figure 3-12 (a) represents the configuration of the test wafers and (b) shows the simulated IR absorption in a 4-layered *Ti* (100 nm)/*SiC* (200 nm)/*Ti* (10 nm)/*SiC* stack. The thickness of the *SiC* spacing layer has been optimized and the spectral effect of *SiC* protective layer has been taken into account as well. Two different

thicknesses of 100 nm and 200 nm are chosen for the SiC protective layer.

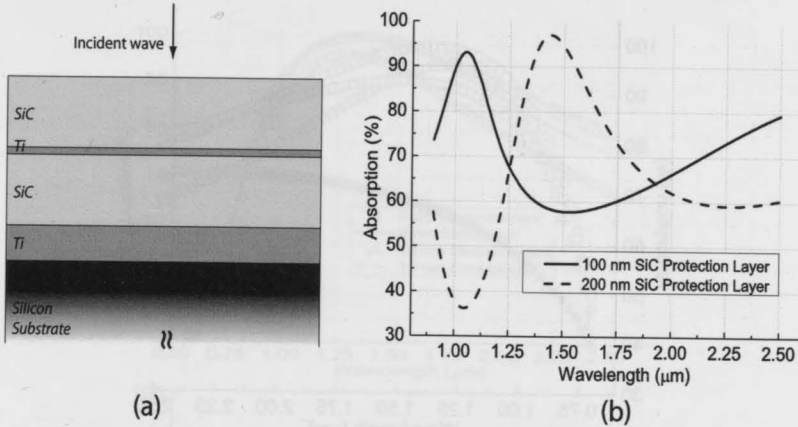


Fig. 3-12. Simulation of thin film stacks absorber protected by additional SiC layer with 100 and 200 nm thickness.

3.2.6 Experimental results

Thin-film Ti absorber layers of the same thickness as used in the simulations have been deposited by sputtering on different silicon wafers. A PerkinElmer LAMBDA 950 spectrophotometer has been used for the measurement. The reflectance from the wafers and transmission through the wafers have been accurately measured. Transmission through the wafers is measured to be negligible for all the wafers and the absorption can be easily calculated. Figure 3-13 shows the absorption calculated from the reflectance measurements on the wafers with SiO_2 spacing layer.

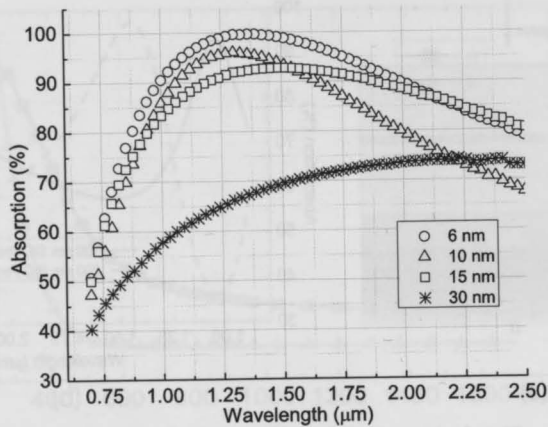


Fig. 3-13. Measured results of absorption on four samples with a SiO₂ spacing layer.

Figure 3-14 shows the comparison between the simulation and measured results. The deviations in the longer wavelength range are due to errors introduced by the extrapolation of the optical properties of *Ti* from the ellipsometric measurements at short-wavelengths. The interference absorber with the thin 6 nm *Ti* layer shows almost perfect absorption, but is more spectrally selective. The absorber with 15 nm *Ti* layer shows more than 70% absorption in the 1 μm to 3 μm spectral range with less absorption variation. The choice depends on the application. It is necessary to consider the wavelength response of the absorbers while calibrating the fabricated thermopiles.

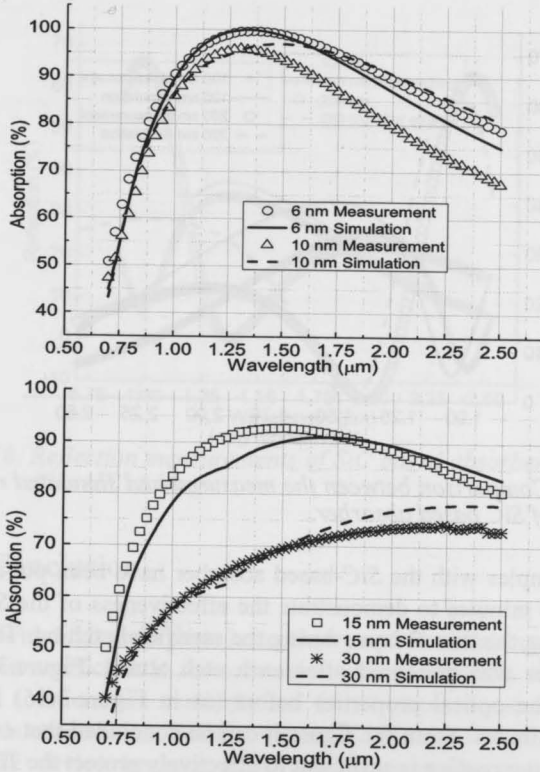


Fig. 3-14. Comparison of measured and simulated results with different thickness of the top Ti layer with SiO_2 spacing layer.

Figure 3-15 shows a comparison between the reflection measurements and simulation for the two different values of the thickness as the SiC protective layer. The deviation at longer wavelength can be explained by the following reason. Extrapolated data is being practiced in the simulation tool for wavelength above 1.2 μm by using the simple linear fit.

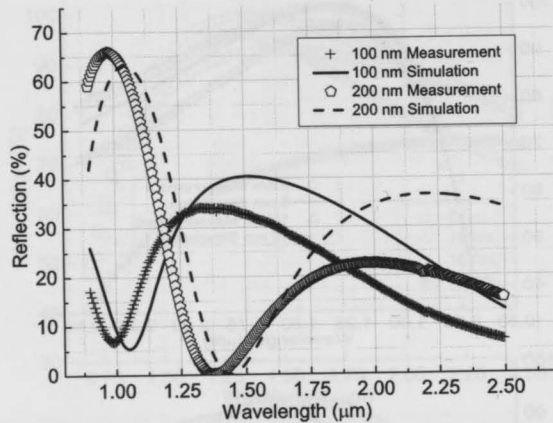


Fig. 3-15. Comparison between the measured and simulated reflection of SiC based absorber.

Several samples with the SiC-based absorber have been put in 73% liquid phase HF for 10 minutes to demonstrate the effectiveness of the SiC protective layer in protecting the thin Ti layer during the sacrificial etching. The reflectance from the samples was measured after each etch attack. Figure 3-16 allows a comparison of the optical properties before (as in Figure 3-15) and after HF etching for 10 minutes. From the figure it can be concluded that even a 100 nm thick SiC protective coating is sufficient to effectively protect the Ti layers during etching.

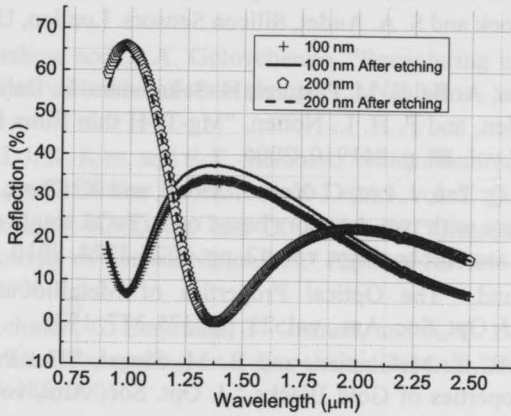


Fig. 3-16. Reflection measurements of SiC based absorber, before and after HF etching.

3.2.7 Conclusion

A layer with high absorption is necessary and essential in order to achieve a high absorption coefficient in the spectral range of interest in a thermal detector array. Several solutions are available and the advantages and disadvantages are analyzed in this chapter. The interference based (microwave) absorber is used for our thermopile device because it is best to meet the requirement of IC-compatibility and post-processing demand.

The design and test of the interference filter based absorbers for use a thermopile array for an IR microspectrometer have been explained. Even though absorbers based on SiO_2 have better spectral response, SiC is still preferred owing to its high resistance to HF etching. The experiments successfully validate the simulations, which imply that the simulation tools and our material data can be used.

3.3 References

- [3.1] S. Middlehoek and S. A. Audet, *Silicon Sensors*. London, UK: Academic, 1989.
- [3.2] D. M. Borsa, A. Baldi, M. Pasturel, H. Schreuders, B. Dam, R. Griessen, P. Vermeulen, and P. H. L. Notten, "Mg-Ti-H thin films for smart solar collectors," vol. 88, p. 241910, 2006.
- [3.3] W. Zhang, Q. Tan, J. Liu, C. Xue, J. Xiong, and X. Chou, "Two-channel IR gas sensor with two detectors based on LiTaO₃ single-crystal wafer," *Optics & Laser Technology*, vol. 42, pp. 1223-1228, 2010.
- [3.4] A. H. Pfund, "The Optical Properties of Metallic and Crystalline Powders," *J. Opt. Soc. Am.*, vol. 23, pp. 375-377, 1933.
- [3.5] L. Harris, R. T. McGinnies, and B. M. Siegel, "The Preparation and Optical Properties of Gold Blacks," *J. Opt. Soc. Am.*, vol. 38, pp. 582-588, 1948.
- [3.6] J. Lehman, E. Theocharous, G. Eppeldauer, and C. Pannell, "Gold-black coatings for freestanding pyroelectric detectors," *Measurement Science and Technology*, vol. 14, p. 916, 2003.
- [3.7] M. Hirota, Y. Nakajima, M. Saito, and M. Uchiyama, "120 × 90 element thermoelectric infrared focal plane array with precisely patterned Au-black absorber," *Sensors and Actuators A: Physical*, vol. 135, pp. 146-151, 2007.
- [3.8] A. Y. Vorobyev and C. Guo, "Metallic Light Absorbers Produced by Femtosecond Laser Pulses," *Advances in Mechanical Engineering*, vol. 2010, pp. 1-5, 2010.
- [3.9] W. Lang, K. Kühn, and H. Sandmaier, "Absorbing layers for thermal infrared detectors," *Sensors and Actuators A: Physical*, vol. 34, pp. 243-248, 1992.
- [3.10] D. J. Advena, V. T. Bly, and J. T. Cox, "Deposition and characterization of far-infrared absorbing gold black films," *Appl. Opt.*, vol. 32, pp. 1136-1144, 1993.
- [3.11] W. L. Wolfe and G. J. Zissis, *The Infrared Handbook*. Ann Arbor: Environmental Research Institute of Michigan, 1989.
- [3.12] E. A. Taft and H. R. Philipp, "Optical Properties of Graphite," *Physical Review*, vol. 138, p. A197, 1965.

- [3.13] Y. S. Touloukian, *Thermophysical properties of matter; [the TPRC data series; a comprehensive compilation of data]*. New York: IFI/Plenum, 1970.
- [3.14] M. Gershow and J. A. Golovchenko, "Recapturing and trapping single molecules with a solid-state nanopore," *Nat Nano*, vol. 2, pp. 775-779, 2007.
- [3.15] J. Q. Xi, J. K. Kim, and E. F. Schubert, "Silica Nanorod-Array Films with Very Low Refractive Indices," *Nano Letters*, vol. 5, pp. 1385-1387, 2005.
- [3.16] S. Berber, Y.-K. Kwon, and D. Tománek, "Unusually High Thermal Conductivity of Carbon Nanotubes," *Physical Review Letters*, vol. 84, p. 4613, 2000.
- [3.17] J. H. Lehman, C. Engtrakul, T. Gennett, and A. C. Dillon, "Single-wall carbon nanotube coating on a pyroelectric detector," *Appl. Opt.*, vol. 44, pp. 483-488, 2005.
- [3.18] J. H. Lehman, R. Deshpande, P. Rice, B. To, and A. C. Dillon, "Carbon multi-walled nanotubes grown by HWCVD on a pyroelectric detector," *Infrared Physics & Technology*, vol. 47, pp. 246-250, 2006.
- [3.19] M. E. Itkis, S. Niyogi, M. E. Meng, M. A. Hamon, H. Hu, and R. C. Haddon, "Spectroscopic Study of the Fermi Level Electronic Structure of Single-Walled Carbon Nanotubes," *Nano Letters*, vol. 2, pp. 155-159, 2002.
- [3.20] S. D. Senturia, *Microsystem Design*: Kluwer Academic Publishers, 2000.
- [3.21] S. Vollebregt, R. Ishihara, J. Derakhshandeh, W. Wien, J. van der Cingel, and K. Beenakker, "Patterned growth of carbon nanotubes for vertical interconnect in 3D integrated circuits," 2010.
- [3.22] K. Mizuno, J. Ishii, H. Kishida, Y. Hayamizu, S. Yasuda, D. N. Futaba, M. Yumura, and K. Hata, "A black body absorber from vertically aligned single-walled carbon nanotubes," *Proceedings of the National Academy of Sciences*, vol. 106, pp. 6044-6047, 2009.
- [3.23] J.-Q. Xi, M. F. Schubert, J. K. Kim, E. F. Schubert, M. Chen, S.-Y. Lin, W. Liu, and J. A. Smart, "Optical thin-film materials with low refractive index for broadband elimination of Fresnel reflection," *Nat Photon*, vol. 1, pp. 176-179, 2007.
- [3.24] M. E. Itkis, F. Borondics, A. Yu, and R. C. Haddon, "Bolometric Infrared Photoresponse of Suspended Single-Walled Carbon Nanotube Films," *Science*, vol. 312, pp. 413-416, April 21, 2006.

- [3.25] J. Lehman, A. Sanders, L. Hanssen, B. Wilthan, J. Zeng, and C. Jensen, "Very Black Infrared Detector from Vertically Aligned Carbon Nanotubes and Electric-Field Poling of Lithium Tantalate," *Nano Letters*, vol. 10, pp. 3261-3266, 2010.
- [3.26] C. Hu, C. Liu, L. Chen, C. Meng, and S. Fan, "A Demo Opto-electronic Power Source Based on Single-Walled Carbon Nanotube Sheets," *ACS Nano*, vol. 4, pp. 4701-4706, 2010.
- [3.27] B. Ung, "Metamaterials: a metareview," *École Polytechnique de Montréal*, Montréal 2009.
- [3.28] G. Dolling, M. Wegener, C. M. Soukoulis, and S. Linden, "Negative-index metamaterial at 780 nm wavelength," *Opt. Lett.*, vol. 32, pp. 53-55, 2007.
- [3.29] C. Caloz and T. Itoh, *Electromagnetic metamaterials: transmission line theory and microwave applications*. New Jersey: John Wiley & Sons, Hoboken 2006.
- [3.30] P. V. Parimi, W. T. Lu, P. Vodo, and S. Sridhar, "Photonic crystals: Imaging by flat lens using negative refraction," *Nature*, vol. 426, pp. 404-404, 2003.
- [3.31] M. Qiu, "Effective index method for heterostructure-slab-waveguide-based two-dimensional photonic crystals," *Applied Physics Letters*, vol. 81, pp. 1163-1165, 2002.
- [3.32] D. R. Smith and J. B. Pendry, "Homogenization of metamaterials by field averaging (invited paper)," *J. Opt. Soc. Am. B*, vol. 23, pp. 391-403, 2006.
- [3.33] N. I. Landy, S. Sajuyigbe, J. J. Mock, D. R. Smith, and W. J. Padilla, "Perfect Metamaterial Absorber," *Physical Review Letters*, vol. 100, p. 207402, 2008.
- [3.34] D. Schurig, J. J. Mock, and D. R. Smith, "Electric-field-coupled resonators for negative permittivity metamaterials," *Applied Physics Letters*, vol. 88, p. 041109, 2006.
- [3.35] J. B. Pendry, A. J. Holden, D. J. Robbins, and W. J. Stewart, "Magnetism from conductors and enhanced nonlinear phenomena," *Microwave Theory and Techniques, IEEE Transactions on*, vol. 47, pp. 2075-2084, 1999.
- [3.36] H. Tao, N. I. Landy, C. M. Bingham, X. Zhang, R. D. Averitt, and W. J. Padilla, "A metamaterial absorber for the terahertz regime: design,

- fabrication and characterization," *Opt. Express*, vol. 16, pp. 7181-7188, 2008.
- [3.37] J. Valentine, S. Zhang, T. Zentgraf, E. Ulin-Avila, D. A. Genov, G. Bartal, and X. Zhang, "Three-dimensional optical metamaterial with a negative refractive index," *Nature*, vol. 455, pp. 376-379, 2008.
- [3.38] Z. H. Jiang, Q. Wu, X. Wang, and D. H. Werner, "Flexible wide-angle polarization-insensitive mid-infrared metamaterial absorbers," *Antennas and Propagation Society International Symposium (APSURSI)*, 2010 IEEE, pp. 1-4, 2010.
- [3.39] T. Maier and H. Brueckl, "Multispectral microbolometers for the midinfrared," *Opt. Lett.*, vol. 35, pp. 3766-3768, 2010.
- [3.40] Y. Avitzour, Y. A. Urzhumov, and G. Shvets, "Wide-angle infrared absorber based on a negative-index plasmonic metamaterial," *Phys. Rev. B*, vol. 79, p. 045131, 2009.
- [3.41] J. Hao, J. Wang, X. Liu, W. J. Padilla, L. Zhou, and M. Qiu, "High performance optical absorber based on a plasmonic metamaterial," *Applied Physics Letters*, vol. 96, pp. 251104-3, 2010.
- [3.42] W. Zhu and X. Zhao, "Metamaterial absorber with dendritic cells at infrared frequencies," *J. Opt. Soc. Am. B*, vol. 26, pp. 2382-2385, 2009.
- [3.43] X. Liu, T. Starr, A. F. Starr, and W. J. Padilla, "Infrared Spatial and Frequency Selective Metamaterial with Near-Unity Absorbance," *Physical Review Letters*, vol. 104, p. 207403, 2010.
- [3.44] Y. Q. Ye, Y. Jin, and S. He, "Omnidirectional, polarization-insensitive and broadband thin absorber in the terahertz regime," *J. Opt. Soc. Am. B*, vol. 27, pp. 498-504, 2010.
- [3.45] G. Biener, A. Niv, V. Kleiner, and E. Hasman, "Metallic subwavelength structures for a broadband infrared absorption control," *Opt. Lett.*, vol. 32, pp. 994-996, 2007.
- [3.46] P. A. Silberg, "Infrared Absorption of Three-Layer Films," *J. Opt. Soc. Am.*, vol. 47, pp. 575-578, 1957.
- [3.47] A. D. Parsons and D. J. Pedder, "Thin film infrared absorber structures for advanced thermal detectors," *Journal of Vacuum Science Technology A: Vacuum, Surfaces, and Films*, vol. 6, pp. 1686-1689, 1988.
- [3.48] H. Bosman, Y. Y. Lau, and R. M. Gilgenbach, "Microwave absorption on a thin film," *Applied Physics Letters*, vol. 82, pp. 1353-1355, 2003.
- [3.49] F. Niklaus, C. Jansson, A. Decharat, J.-E. Kallhammer, H. Pettersson, and G. Stemme, "Uncooled infrared bolometer arrays operating in a low to

- medium vacuum atmosphere: performance model and tradeoffs," *Infrared Technology and Applications XXXIII*, vol. 6542, p. 65421M, 2007.
- [3.50] X. C. Tong, "Absorber Materials," in *Advanced Materials and Design for Electromagnetic Interference Shielding*, ed: CRC Press, pp. 237-255, 2009.
- [3.51] P. A. Chatterton, *EMC : electromagnetic theory to practical design* / Paul A. Chatterton and Michael A. Houlden. Chichester ; New York :: Wiley, 1992.
- [3.52] P. Saville, "Review of Radar Absorbing Materials," Defence R&D Canada 2005.
- [3.53] K. C. Liddiard, "Application of interferometric enhancement to self-absorbing thin film thermal IR detectors," *Infrared Physics*, vol. 34, pp. 379-387, 1993.
- [3.54] TFCalc™ Software Spectra Inc., "www.sspectra.com," 3.3 ed.
- [3.55] A. Roncaglia, F. Mancarella, and G. C. Cardinali, "CMOS-compatible fabrication of thermopiles with high sensitivity in the 3-5 [μ]m atmospheric window," *Sensors and Actuators B: Chemical*, vol. 125, pp. 214-223, 2007.
- [3.56] SOPRA Database; www.sopra-sa.com.
- [3.57] G. Pandraud, H. T. M. Pham, P. J. French, and P. M. Sarro, "PECVD SiC optical waveguide loss and mode characteristics," *Optics & Laser Technology*, vol. 39, pp. 532-536, 2007.

Thermo-Electric Effect and Design of the Detector Array

4

4.1 Introduction

It is necessary to convert the heat, which is from the absorbed incident light, as described in the previous section, into an electrical signal. The electrical signal encoded the intended information can be efficiently processed using microelectronic circuits. The conversion from the thermal into the electrical domain is described by thermoelectricity. The thermoelectricity refers to the physical effects that is used to convert a temperature difference into an electric potential or the other way around. Those physical effects are: Seebeck effect, Peltier effect, and the Thomson effect. The Peltier effect and the Thomson effect are briefly described in the chapter 2 at page 21, only the Seebeck effect is elaborated in this chapter. A figure of merit Z is used to characterize the suitability of the thermoelectric material and can be expressed in terms of Seebeck coefficient, thermal conductivity and internal resistance. Various thermoelectric materials are discussed. Polysilicon is selected as the material of the thermopile, because it is the standard *CMOS* material and has an acceptable Seebeck coefficient.

The design and analysis of a single *TE* element (pixel) is given and further extended to an array. The array is designed and intended to use in either grating or

LVOF-based microspectrometer.

4.2 Thermal parameters

4.2.1 The Seebeck effect

An electrical potential difference V is generated within any isolated conduction material that is subjected to a temperature gradient ΔT . The physical phenomenon is called the absolute Seebeck effect. The absolute Seebeck coefficient $\alpha_{Seebeck}$ is defined accordingly as the instantaneous rate of change of V with respect to the temperature at a given temperature T_0 [4.1]:

$$\alpha_{Seebeck} = \left. \frac{dV}{dT} \right|_{T_0} \quad (4-1)$$

When two different materials are joined together at one point and a temperature difference is maintained between the joined and non-joined parts of the materials, an open-circuit voltage develops between the non-joined parts of this thermocouple as illustrated in Figure 4-1. The resulting voltage ΔT is proportional to the temperature difference between hot and cold junctions, and to the difference in Seebeck coefficient of the thermocouple materials a and b :

$$\Delta V = \alpha_{ab} \Delta T = (\alpha_{a,Seebeck} - \alpha_{b,Seebeck}) \Delta T \quad (4-2)$$

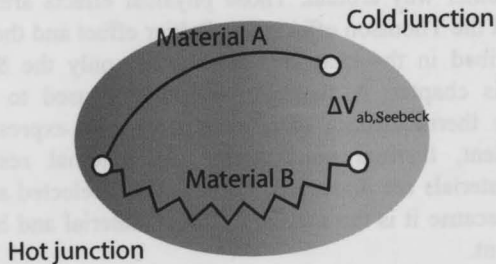


Fig. 4-1. Illustration of simple thermocouple structure.

The Seebeck coefficient of a material can be approximated for the range of

interest used in sensors and at room temperature as a function of electrical resistivity ρ [4.2]:

$$\alpha_{\text{Seebeck}} = m \cdot k \cdot \ln \frac{\rho}{\rho_0} \cdot \frac{1}{q} \quad (4-3)$$

where $\rho_0 = 5 \times 10^{-6} \Omega\text{m}$, $m = 2.6$, q is the elementary charge and k is the Boltzman constant.

In a semiconductor, the electrical resistivity is inverse proportional to the doping concentration. Eqn (4-3) indicates that higher doping in the semiconductor results in a lower Seebeck coefficient. Nevertheless, as compared to metals, semiconductor materials have the best potential using in a thermocouple or thermopile and to satisfy the demands of miniaturization and mass production as stated in below [4.3]:

- Semiconductors offer a higher Seebeck coefficient than metals.
- Strong dependence of the Seebeck coefficient on the concentration of mobile charge carriers and the charge carrier mobility resulting in the main characteristics of semiconducting thermopiles can be tuned by doping.
- Micromachining technology used in semiconductor allows the thermal capacity to be reduced effectively and thus performance is improved.
- Possible integration into a conventional IC process like the CMOS process.

4.2.2 The thermal conductivity

The thermal conductivity λ is the property of a material that describes its ability to conduct heat. It appears primarily in Fourier's Law for the heat conduction. According to Fourier's law, the heat transfer rate or heat flux q between the bodies is found by the relation:

$$q = \lambda A \frac{\Delta T}{L} \quad (4-4)$$

where λ is the thermal conductivity of the material, A is the cross sectional area, L is the distance between bodies and ΔT is the temperature difference.

It has been shown that the thermal conductivity λ is inverse proportional to

the temperature difference ΔT in the case of constant heat flux. For a maximum Seebeck output voltage, the thermal conductivity should be as small as possible. A low thermal conductivity would produce high figure of merit Z as shown in the Eqn (4-5). Hence, it is critical to characterize the thermal conductivity λ of each thin film layer in the process for drawing the high performance of thermoelectric detector array as well as the microspectrometer. *IC* compatible thin-film materials include *SiN*, *PolySi* and metal layer which is the aluminium in the low temperature fabrication process. The thermal conductivities of *PolySi* layers depend on the deposition process details, including the grain size, shape, the concentration and type of dopant atoms [4.4].

4.2.3 Figure of merit of a thermoelectric material

The thermoelectric efficiency of a material can be estimated by defining the figure of merit Z :

$$Z = \frac{\alpha_{Seebeck}^2}{\rho\lambda} \quad (4-5)$$

Materials with a high figure of merit Z have a high Seebeck coefficient, low thermal conductivity and low internal resistance. Consequently, they effectively transform heat into an electrical voltage and have simultaneously low noise power. For an optimal *SNR* of a thermocouple, the figure Z has to be maximized [4.5].

A comparison between some thin-films and microelectronics compatible materials is summarized in Table 1 [4.6]. Polysilicon has an acceptable performance among other materials and is the well-known material in a *CMOS* process line. Notwithstanding, as discussed earlier, the Seebeck coefficient and electrical resistivity parameters used to estimate such comparative value can vary strongly with the doping type and carrier density.

TABLE 1. Seebeck coefficient, thermal conductivity, electrical resistivity and figure of merit of some thin-films and microelectronics compatible materials [4.6].

Material	Seebeck coefficient α ($\mu\text{V/K}$)	Thermal conductivity λ (W/(Km))	Electrical resistivity ρ ($10^{-6} \Omega\text{m}$)	Figure of merit Z ($10^{-6}/\text{K}$)
$\text{Bi}_{0.5}\text{Sb}_{1.5}\text{Te}_3$ ($p=3 \times 10^{19} \text{cm}^{-3}$)	230	1.05	17	2963
Sb_2Te_3	130	2.8	5	1200
$\text{Bi}_{0.87}\text{Sb}_{0.13}(n)$	-100	3.1	7.1	454
$\text{Al}_{0.45}\text{Ga}_{0.55}\text{As}$ ($n=10^{17} \text{cm}^{-3}$)	-670	10.9	130	317
Sb	48.9	24	0.42	237
CuNi	-35.1	19.5	0.52	121
PolySi($n=3 \times 10^{19} \text{cm}^{-3}$)	-121	29.4	8.9	56
$\text{Al}_{0.15}\text{Ga}_{0.85}\text{As}$ ($n=10^{17} \text{cm}^{-3}$)	-350	16.9	180	40.3
Silicon	$\pm 100-1000$	144	35	40
n-Poly AMS	-65	29	8	17.9
GaAs ($n=10^{17} \text{cm}^{-3}$)	-300	44.1	150	13.6
p-Poly AMS	135	29	55	12.1
Al	-3.2	238	0.028	1.53
Au	0.1	314	0.023	0.0014

4.3 Design a thermoelectric detector element (pixel)

The design and analysis of single *TE* element (pixel) based on both analytical modeling and numeral method will be given here. Using a

micromachining technology, the *TE* element is deposited on a thin film bridge or cantilever such that the vertically thermal leakage through the substrate is minimized. The details of the micromachining technology are discussed in detail in the following chapter. Thus, the performance of a single element is evaluated precisely according to the thin films structure.

4.3.1 Analytical modeling

4.3.1.1 Thermal modeling of cantilever structure

Two structures are used for the device: the bridge and the cantilever (half bridge) as illustrated in Figure 4-2. To simplify the process, the thermal sensor under the consideration in this chapter is a cantilever or half bridge which is the reduced model from the structure of full bridge due to symmetry. The cantilever length is denoted by L and its width by W . It consists of N thermocouples of n type *PolySi* and p type *PolySi* with widths and thickness of w_1, t_1, w_2, t_2 , respectively. The total thickness of the dielectric layers is denoted by t_d . The thermal conductivity, the specific heat and the density of each layer are denoted by λ, c , and ρ with the corresponding indices ($1, 2$ and d). The differential equation describing the static heat balance in the thermally isolated structures, which is practiced by the micromachining technology, is presented as [4.7]:

$$\alpha \left(\frac{\partial^2 T}{\partial x^2} + \frac{\partial^2 T}{\partial y^2} + \frac{\partial^2 T}{\partial z^2} \right) + \frac{\Phi_s}{\rho c_p} = 0 \quad (4-6)$$

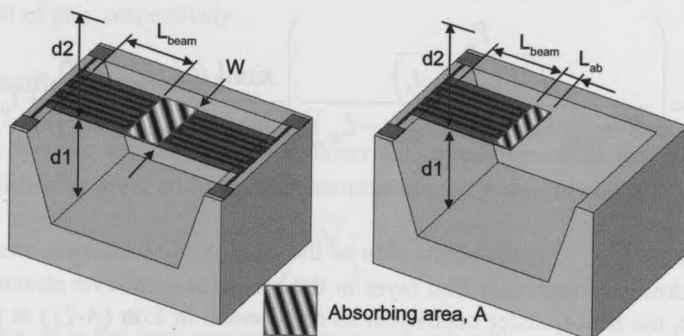


Fig. 4-2. Illustration of the thermopiles on the full bridge (left) or cantilever (right) forming a single TE element.

The analytical solution, which demonstrates the temperature distribution along the bridge or cantilever, can be derived from the general heat conduction equation with some conditions and assumptions:

- It is assumed that the thermal insulation at the side edges of the microstructures is perfect.
- It is assumed that the temperature variation of thin film stacks can be ignored because a very thin membrane is utilized to support the thermopile.
- It is assumed that the temperature of substrate is always considered a constant value.
- The perfect absorber is assumed such that the inward optical flux is fully converted into the heat flux.

The first assumption is reasonable when the temperature distribution can be seen constant along others axis due to the micro-sensing pixel. Both cantilever structure and bridge structure have the physical geometries at which heat energy would flow toward the substrate of the device. The temperature difference ΔT between the substrate and absorber is in agreement with the third assumption. Including these assumptions, the three dimensional physical model can be reduced to one dimensional model, as presented in appendix A. The analytical

solution is expressed as:

$$T(x) = \left(\frac{\frac{P_{in}}{\beta \cdot W (\sum \lambda_s \cdot t_s)}}{\beta \cdot L_{beam} + \coth(\beta \cdot (L_{beam} - L_{ab}))} \right) \frac{\sinh(\beta \cdot (L_{beam} - x))}{\sinh(\beta \cdot (L_{beam} - L_{ab}))} + T_0 \quad (4-7)$$

where $\sum \lambda_s \cdot t_s$ is the summation of the product of the thermal conductivity and thickness of each thin film layer in the bridge or cantilever structure and β refers to the heat transfer coefficient as represented in Eqn (A-21) at page 145. While $x =$ (temperature at the interface of the absorber and the beam), the above equation can be advanced simplified into:

$$T(L_{ab}) = \frac{P_{in}}{\left(4\epsilon\sigma T_0^3 + \lambda_{gas} \left(\frac{1}{d_1} + \frac{1}{d_2} \right) \right) L_{ab} W + W (\sum \lambda_s t_s) \beta \coth(\beta L_{beam})} + T_0 \quad (4-8)$$

4.3.2 Figure of merit of a thermal detector

Sensitivity or Responsivity

The sensitivity (responsivity) of a thermopile element in the IR detector can be calculated from:

$$S_v = \frac{\Delta V}{P_{in}} \left[\frac{V}{W} \right] \quad (4-9)$$

where ΔV is the Seebeck voltage of the thermopile and P_{in} is the incident radiation flux.

Combined the Eqn (4-8) and Eqn (4-9), the sensitivity of a TE element can be expressed as:

$$S = \frac{\Delta V}{P_{in}} = \frac{N\alpha_{Seebeck} \Delta T}{P_{in}} = \frac{N\alpha_{Seebeck}}{\left(4\epsilon\sigma T_0^3 + \lambda_{gas} \left(\frac{1}{d_1} + \frac{1}{d_2} \right) \right) L_{ab} W + W (\sum \lambda_s t_s) \beta \coth(\beta L_{beam})} \quad (4-10)$$

where N and α are the numbers of thermocouples and the Seebeck coefficient of pair, respectively.

Specific detectivity D^*

The specific detectivity, which allows the comparison of IR detectors with different absorber areas and sensor technologies, can be determined by:

$$D^* = D\sqrt{A\Delta f} = \frac{S\sqrt{A\Delta f}}{u_{noise}} [cm\sqrt{Hz}W^{-1}] \quad (4-11)$$

where Δf is the measurement frequency bandwidth and u_{noise} is the noise voltage of the thermopile IR detector. Since Johnson noise dominates the u_{noise} , it can be written as:

$$u_{noise} = \sqrt{4kTR_{el}\Delta f} [V\sqrt{Hz}] \quad (4-12)$$

where k is the Boltzmann constant, R_{el} is the electrical resistance of the detector and T is the absolute environment temperature.

R_{el} can be expressed as:

$$R_{el} = N \left(\rho_n \frac{L}{A_n} + \rho_p \frac{L}{A_p} \right) [\Omega] \quad (4-13)$$

where N is the number of thermopiles. ρ_n and ρ_p are specific electrical resistivities of the thermopile on either n or p type material. A_n and A_p are cross sectional areas of the thermopile.

Noise Equivalent Power (NEP)

The NEP represents the incident radiation flux at the sensor producing a signal voltage equal to the total normalized rms noise voltage:

$$NEP = \frac{u_{noise}}{S_v} [W\sqrt{Hz}] \quad (4-14)$$

4.3.3 Numerical modeling method

The physical model is solved in numerical way by applying the finite element method (*FEM*). The physical phenomena can be mathematically modeled in terms of partial differential equations (*PDE*). In resolving *PDEs*, the primary challenge is to create an equation that approximates the equation to be studied. The physical problem, in our case, can be mathematically established by considering the heat conduction differential equation, as presented in Eqn (4-19) and boundary and initial conditions. The equations under considerations are generally complicated and finding their solutions in closed form or by purely analytical means is impractical. The solution approach is based either on eliminating the time dependence in the differential equation completely, which leads to a steady state problem, or rendering the *PDE* into an equivalent ordinary differential equation, which is then solved using other standard techniques such as finite differences [4.8].

COMSOL [4.9] is a general-purpose finite element analysis software package. Finite element method decomposes a complex system into extremely small pieces that are called elements. The software implements equations that govern the behaviour of these elements and solves them all. The results can either be presented in data, or graphical forms. This type of analysis method is typically used for the optimization in a system which is too complicated to analyze by hand. Especially, for three-dimensional structures which normally suit with the reality, it offers more accurate results than the analytical model.

The typical modeling steps as follows:

- Creating the geometry in 2D or 3D structure
- Meshing the geometry
- Defining the physics parameters as initial or boundary conditions
- Calculating the well-defined model
- Interpreting the solutions
- Post-processing the solutions in graphs or export for later usage

Yet *FEM* needs massive computational power which consumes ample time. It is also important to interpret the numerical results into physical meanings. In the following sections, the *FEM* will be used to validate the results from the analytical model.

4.4 Design the thermoelectric detector array for a grating based microspectrometer

4.4.1 The optical system

The structure of the compact planar IR spectrometer is shown in Figure 4-3. The spectrometer consists of two glass plates aligned parallel to each other. All spectrometer optical components, including the input slit and the diffraction grating work in reflection. The incident light is reflected by a metal strip, which is thus acting as a slit, and is redirected towards the diffraction imaging grating fabricated on the upper glass plate. The diffracted light is finally projected on a chip that contains an array of thermoelectric elements.

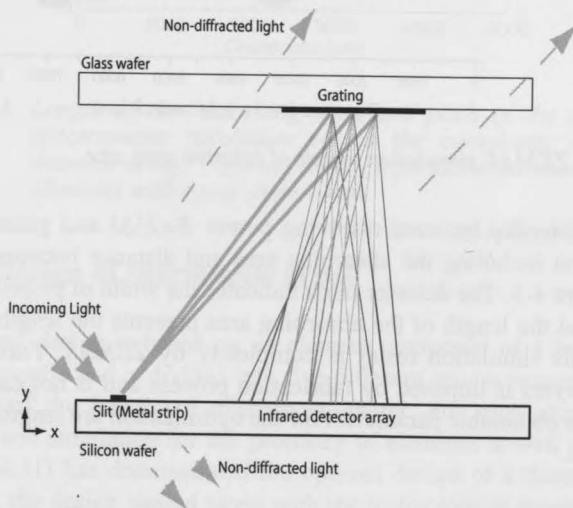


Fig. 4-3. Structure of the planar diffraction imaging grating based IR microspectrometer.

The diffraction imaging grating is basically composed of a pattern of concentric circular grooves in a reflective metal with varying pitch. The grating can be developed to yield maximum spectral resolution at a specified design wavelength. As a consequence the spectral resolution decreases at wavelengths away from this design target, which in this design is at $2.25 \mu\text{m}$. Perfect imaging is in principle achieved at this particular wavelength, as is confirmed by the center

beam incident on the detector array in the figure. The commercial optical design software *ZEMAX* [4.10] was used for the diffraction grating design and for calculation of the spectral resolution at different wavelengths. The result can be generally presented in the form of a spot diagram as shown in Figure 4-4. When the input slit of the spectrometer is illuminated by a monochromatic light source, the spot in this diagram provides an estimation of the full width of the image formed by the optical system. Since it would be pointless to have a detector pitch better than this resolution, the information in Figure 4-4 determines the position-dependent pitch of the elements in the detector array.

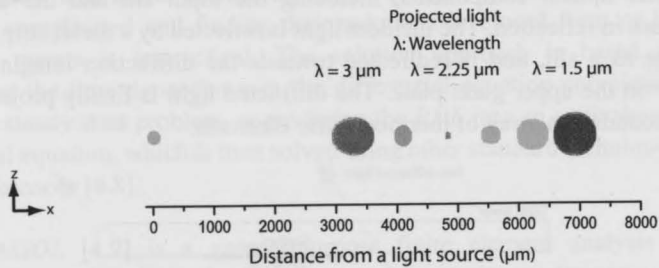


Fig. 4-4. *ZEMAX* simulation result of relative spot size.

The relationship between resolving power $R = \lambda/\Delta\lambda$ and geometry of each sensing element including the absorbing area and distance between elements is shown in Figure 4-5. The detector pitch indicates the width of projected light spot on detector and the length of the absorbing area presents the length of projected light spot. This simulation result is completely by *ZEMAX*. Furthermore, the thickness of layers is imposed by fabrication process and is not easily changed. As a result, the obtainable parameters for the optimization are length and width of the thermopile.

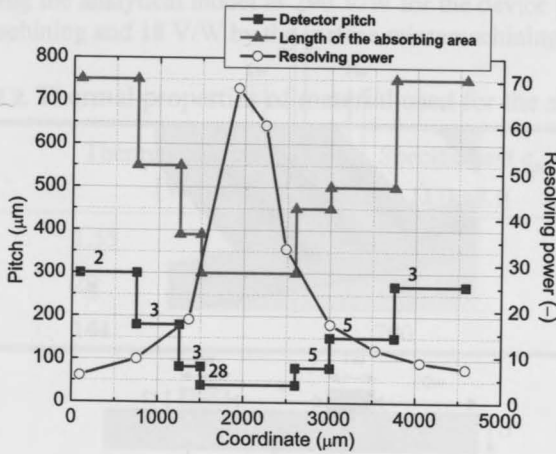


Fig. 4-5. Length of the absorbing area and pitch of the array and spectrometer resolution versus the coordinate along the detector array. Figures on the graph show the number of the elements with equal dimensions.

4.4.2 Design of thermopile array

The array design is based on an element composed of a bridge structure with the thermopile and is divided into five different groups according to optical requirements of the integrated microspectrometer. For each group a separate optimization and simulation for the geometry of elements is well executed. S.H. Kong et al. [4.11] has demonstrated the optimal design of a thermopile device. Nevertheless, the design should along with the technological constraints so as to keep a rational yield of the device after fabrication. Accordingly, the strategy of design here is to optimize the detector under the consideration of the technological constraints.

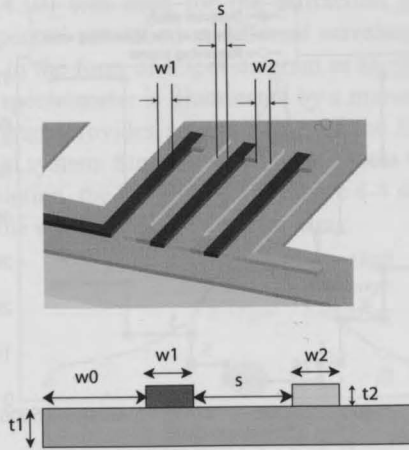


Fig. 4-6. Structure of thermopile on a SiN membrane.

The design begins with the part of highest optical resolution of 68, group 1, in the middle of the array. Group 1 has 28 elements and the distance between elements is $40\ \mu\text{m}$. The length of absorbing area is defined as $300\ \mu\text{m}$ and results from the optical imaging. Since the design is executed by using a bridge structure, the length of the absorbing area should be one half, namely $150\ \mu\text{m}$, in the cantilever analytical model. The bridge structure is implemented by the fabrication of a gap between elements on the rectangular membrane. The $4\ \mu\text{m}$ gap can be achieved by reactive ion etching (RIE). Therefore, the effective width of bridge is $36\ \mu\text{m}$. Since the minimum feature size of implantation is described as $2\ \mu\text{m}$, the width of thermal legs is chosen at $4\ \mu\text{m}$ for safety. Referring to Figure 4-6, the space between legs is determined and fixed at $2\ \mu\text{m}$.

There is also a $2\ \mu\text{m}$ wide space among the rim of membrane and the first thermocouple leg and the last one. Considering all required dimensional constraints, the number of thermocouples in the half-bridge can only be 2.5 (5 for the full bridge structure). The generated voltage is expected to be low since it is proportional to the number of thermocouples. There are two additional layers deposited on the $700\ \text{nm}$ thick SiN membrane. One is the $300\ \text{nm}$ PolySi that constitutes the thermocouple and the other one is the $100\ \text{nm}$ SiN that insulates the conduction between metal and PolySi. The thermal parameters used for the

simulation are orderly listed in Table 1 on page 67 and Table 2. The sensitivity is calculated using the analytical model as 290 V/W for the device practiced by the bulk micromachining and 18 V/W by the surface micromachining.

TABLE 2. Thermal properties of material used for the simulation.

	Thermal conductivity λ [W/(mK)]	Specific heat c_p [J/(kgK)]	Density ρ [kg/m ³]
SiN	1.55	170	2440
PolySi	29	700	2330
Silicon	144	700	2330

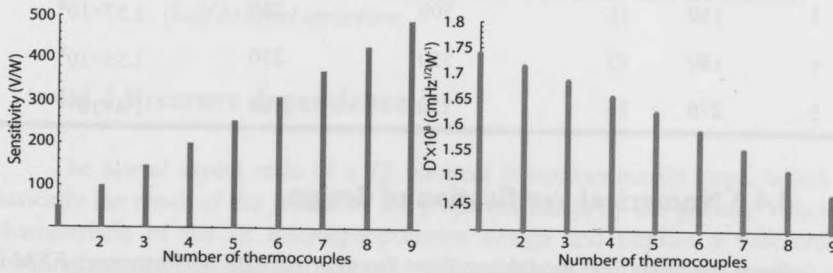


Fig. 4-7. Sensitivity (left) and detectivity (right) as a function of number of thermocouples of the half-bridge structure.

For other groups, which have lower optical resolution, the design procedure is almost the same. The number of thermocouples can be increased though, which makes it possible to generate bigger voltage and hence augment the sensitivity. Figure 4-7 compares the relation between number of thermocouples and Sensitivity for the group 2 of thermopiles realized by the bulk micromachining. However, with the increased number of thermocouples, the total resistance of thermopile is also increased. This implies higher noise and thus lower detectivity as drawn in the Eqn (4-11).

The specific detectivity D^* for thermopiles with a variable number of thermocouples of group 2 type of thermopiles is calculated and the result is shown in Figure 4-7. The number of thermocouples is chosen to be 4 for group 2,

which gives a width of 6 μm and specific detectivity of $1.63 \times 10^8 \text{ cmHz}^{1/2}\text{W}^{-1}$ for the device applied by the bulk micromachining. The simulated performance of a single *TE* element realized by bulk micromachining in each group is summarized in Table 3.

TABLE 3. Simulated performance of *TE* elements in the case of device realized by bulk micromachining.

Group	Pitch (μm)	Number of thermocouples (half bridge)	Absorber length (μm)	Sensitivity (V/W)	D^* ($\text{cmHz}^{1/2}\text{W}^{-1}$)
1	40	2.5	300	290	1.55×10^8
2	80	4	450	200	1.63×10^8
3	150	11	500	260	1.57×10^8
4	180	13	550	250	1.55×10^8
5	270	16	750	180	1.4×10^8

4.4.3 Numerical verification of design

Since the analytical model conducts the approximate performance, *FEM* is used for the verification and for finalizing the design parameters. Commercial *FEM* software, *COMSOL*, simulates the temperature gradient along the thermopile length from the defined three-dimensional model. Figure 4-8 represents the *3D FEM* simulation result of the temperature distribution along an element in group 1 thermopiles. The model can be reduced to half of bridge structure because of the symmetry. It is 36 m wide and 591 μm long (150 μm length of absorber, 341 μm the effective length of thermopile and 100 μm substrate).

A power of 0.27 μW is radiated to the surface of absorber. On the other side of the element, the temperature of the substrate is fixed to 300 K. The figure indicates a temperature difference between hot and cold junctions of the thermopile of about 0.126 K, which is equivalent to a sensitivity of 289 V/W for the device completed by the bulk micromachining. The simulation results show a reduced sensitivity as compared to the analytical model, which is due to the fact that the *3D FEM* analysis also considers convection and radiation in the complex

coordinate system.

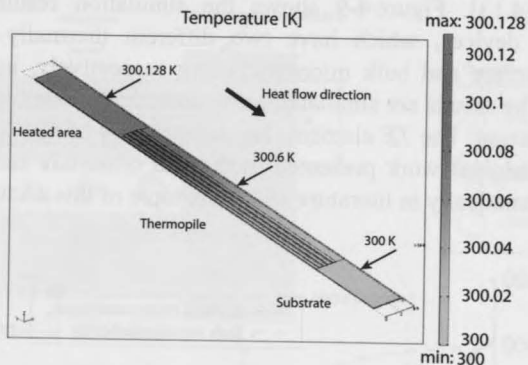


Fig. 4-8. FEM simulation result of a group 1 element with a cantilever (half bridge) structure.

4.4.4 Pressure dependence

The lateral aspect ratio of a *TE* element is extraordinarily large, which is basically the result of the format of the projected image by the grating. This is a characteristic of the *IR* microspectrometer design and implies a vast cross-sectional area among adjacent elements within the array and results in a relatively large heat exchange among elements in this lateral direction by the thermal diffusion even in case of the bulk silicon removed, which is referred to as the thermal cross-talk. Therefore, heat exchange by conduction through the membrane support should be eliminated, which is achieved by cutting trenches in between *TE* elements.

The shape of the resulting *TE* element is a bridge (absorption at middle) or a cantilever (absorption at tip) structure. A maximum optical revolving power implies a minimum element pitch. Hence, the spacing between two *TE* elements should be minimized for the optical performance. Nevertheless, the heat flux from one element to neighbouring element by the conduction through the surrounding gas increases with the decreasing gap. Consequently, a proper design is able to combine the high spectral selectivity of the *IR* microspectrometer with low thermal cross-talk between neighbouring *TE* elements.

The problem of thermal cross-talk is suitable for the detrimental effect of a

thermal shunt on sensitivity in conventional single-element thermopile-based devices [4.12][4.13]. Figure 4-9 shows the simulation results on improved sensitivity for devices, which have two different thermally isolated cavity realizing by surface and bulk micromachining respectively, in a low-pressure environment. The results are simulated using analytical modeling as discussed in the previous section. The TE elements has a sensitivity of 490 V/W at 0.1m Bar pressure. The original work presented in thermal cross-talk issue has not been addressed systematically in literature and is the topic of this section.

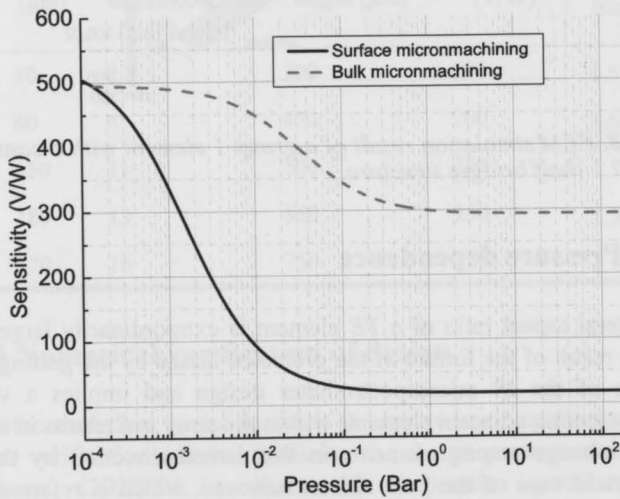


Fig. 4-9. Analytical simulation results of sensitivity versus air pressure of the group 1 TE element with 4 μm distance to substrate (surface micromachining) and 525 μm distance to substrate (bulk micromachining).

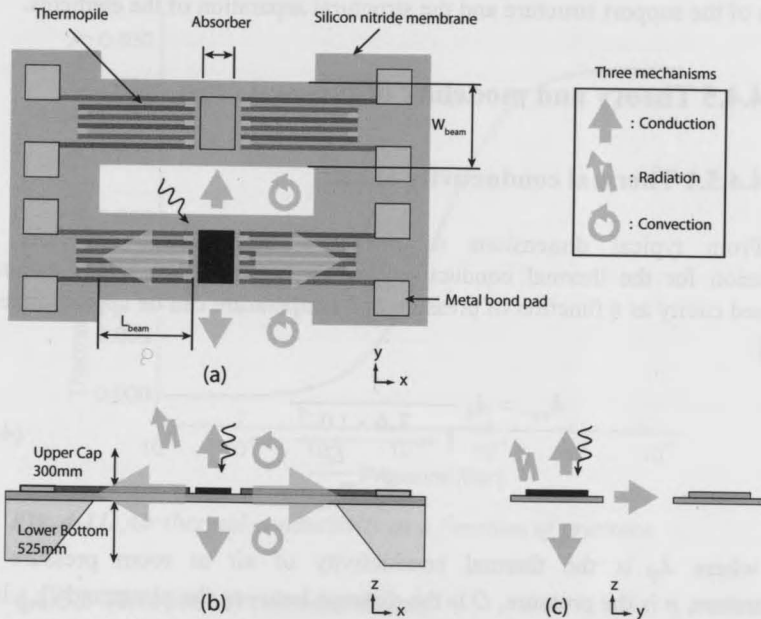


Fig. 4-10. Heat transfer mechanisms in the thermopile bridge-shaped detector. (a) Two bridges are illustrated and the below bridge has the absorbed heat flux to transfer. (b) and (c) are the cross-sectional view.

Figure 4-10 illustrates the configuration of the detector. The SiN bridge structure acts as the support structure for the thermopile, which is formed by the n-p type *PolySi* thermocouples. The thermocouples convert the thermal energy from the projection light of grating via absorber (middle of bridge) into the voltage with Seebeck effect. Conduction, convection and radiation are the three mechanisms of loss. The thermal transfer from the these three mechanisms acting on the *TE* element is resented schematically as well in Figure 4-10. All these loss mechanisms should be considered while analyzing the sensitivity of a single element. Because of the aspect ratio of an element (small gap as compared to sidewall area) only heat exchange between adjacent elements by the conduction and convection is included entirely. The *TE* array is within an *IC*-compatible package. Therefore, the volume around an element is small and the effect of gas pressure on the performance of detector has to be considered. As is shown in this analysis, the gas conductivity determines the residual thermal cross-talk and,

consequently, the lower limit of what can actually be achieved by the optimized design of the support structure and the structural separation of the elements.

4.4.5 Theory and modeling of thermal cross-talk

4.4.5.1 Thermal conductivity of air

From typical dimensions of packaged MEMS-based detectors, the expression for the thermal conductivity of air between two plates within an enclosed cavity as a function of pressure and temperature can be approximated as [4.14]:

$$\lambda_{air} = \lambda_0 \frac{1}{1 + \frac{7.6 \times 10^{-5}}{p \cdot \frac{D}{T_{avg}}}} \quad (4-15)$$

where λ_0 is the thermal conductivity of air at room pressure and temperature, p is the pressure, D is the distance between the plates and T_{avg} is the average temperature of the plates. When assuming a plate spacing of 10 μm , an average temperature of 300K and $\lambda_0 = 0.0284 \text{ Wm}^{-1}\text{K}^{-1}$, a pressure-dependent thermal conductivity of air results as shown in the Figure 4-11.

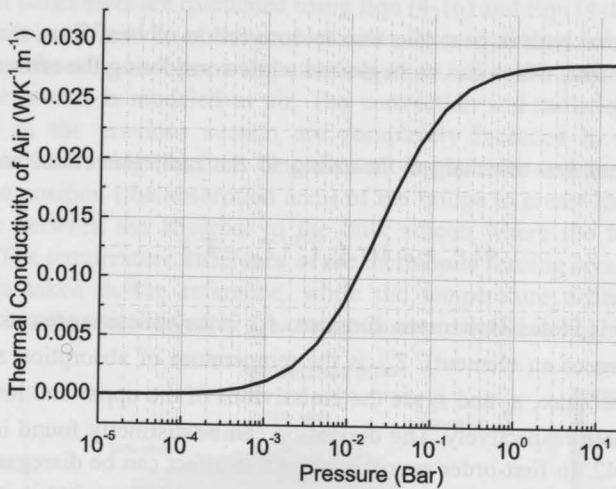


Fig. 4-11. Air thermal conductivity as a function of pressure.

4.4.5.2 Theoretical considerations

The operation of the infrared thermopile detector is based on the Seebeck effect. Radiation incident on the detectors heats up the absorption region and results in temperature gradient, which yields a Seebeck voltage. Analytical solutions for the heat conduction, which include convection and radiation losses, have been developed by assuming the direction of heat transfer in only one direction [4.14][4.15]. There are three paths for the heat flow generated from radiant energy in the middle of the bridge-shaped thermo-electric detector. The first path is the heat conduction through the solid materials that comprise the suspension. The equivalent thickness and equivalent thermal conductivity of multi-layers bridge can be expressed as:

$$t_{eq} = \sum_{s=1}^n t_s \quad (4-16)$$

$$\lambda_{eq} = \frac{1}{t_{eq}} \sum_{s=1}^n \lambda_s \cdot t_s \quad (4-17)$$

where the t_s and λ_s denote the thickness of thin film and the thermal

conductivity of material respectively.

The second path is heat loss due to convection of heat from the detector surface to ambient, which can be neglected while considering the sensor package volume [4.16].

The final loss mechanism is owing to the radiation effect and can be expressed as:

$$4(\varepsilon_u + \varepsilon_l) \sigma A_{ab} T_0^3 (T_{ab} - T_0) \quad (4-18)$$

where σ is Stefan-Boltzmann constant, A_{ab} is the emission area (equal to the absorption area of an element), T_{ab} is the temperature of absorption area, T_0 is ambient temperature, ε_u and ε_l are the emissivities of the upper and lower layers of emission area respectively. The derivation can be distinctly found in Eqn (A-10) at page 142. In first-order approximation this effect can be disregarded while taking account of the small value of the temperature increase, but is included in more accurate calculations.

The dynamic response is governed by the Fourier equations, which is based on the heat transfer theory and is expressed as [4.7]:

$$\frac{\partial T}{\partial t} = \alpha \left(\frac{\partial^2 T}{\partial x^2} + \frac{\partial^2 T}{\partial y^2} + \frac{\partial^2 T}{\partial z^2} \right) + \frac{\Phi_s}{\rho c_p} \quad (4-19)$$

where ρ is the density of (stacked) material, c_p is the specific heat capacity, Φ_s is the heat source per volume V . This equation can be applied in finding a simplified analytical expression of the sensitivity of a single element in a cavity. Notwithstanding, the device structure of a detector array with cross-talk is more complex. The detector array is designed and fabricated to have fixed value of the gap width between elements. This is a 2-dimensional problem with heat flux between several objects. Therefore, the numerical method, the commercially available *FEM* software *COMSOL*, has been utilized to solve the heat transfer equation.

4.4.5.3 Static response

Several layers are stacked during the fabrication of the meander-shaped

thermopile deposited on the top of supporting membrane. Accordingly, the equivalent parameters are calculated using Eqn (4-16) and Eqn (4-17). Symmetry allows the simplification of the problem into three quarter-sized *TE* elements, which significantly reduces computational time. The 10 μm wide spacing between elements is modeled as air. The convection and radiation loss factors described in the previous section are completely included in the boundary conditions of the bridge surface. One element is given the constant heat flux in the middle position (the absorption area) of the bridge to create the temperature difference between the absorber to the bulk silicon where the temperature is constant. The temperature difference of the thermopile sensing area of the heated element is taken as the reference, while the temperature difference of two neighbouring elements indicates the cross-talk as presented in Figure 4-12.

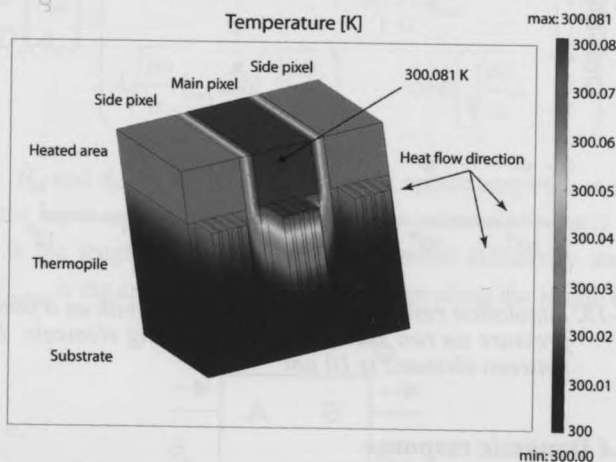


Fig. 4-12. FEM simulation of cross-talk on three *TE* elements.

Another simulation is made by taking the reference and two successive neighbouring elements to simulate the across cross-talk. The simulation result of cross-talk as a function of pressure, while assuming a constant ambient temperature at 300 K, is shown in Figure 4-13. The thermal parameters used for simulation are listed in Table 2. The cross-talk of the main pixel to the first side pixel is crucial and is 5.16% at 1 Bar (room pressure). The cross-talk towards only one side is calculated and the result should be multiplied by two for both sides. The figure exactly demonstrates that the effect is significantly reduced when lowering the air pressure in the chamber in the device package. This is in agreement with the reduced effect of air-conduction on the sensitivity of a single

element. Cross-talk becomes negligible at air pressures below 10^{-5} Bar. The cross-talk toward the next pixel (second in line) is about 0.13% at atmospheric pressure, which is because of the larger distance to the heated element. Thus, this effect can be ignored and only the two directly neighbouring elements need to be considered.

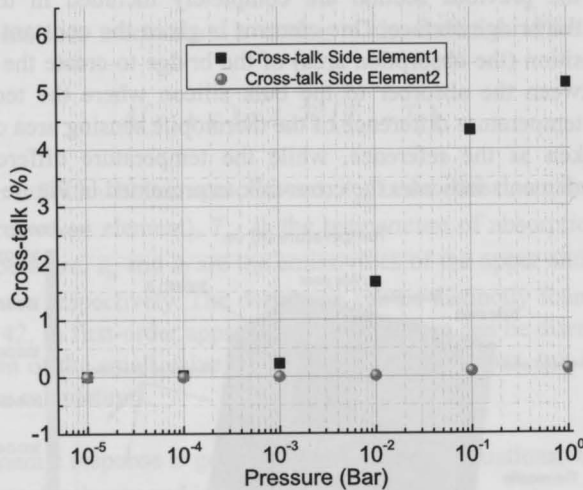


Fig. 4-13. Simulation results of (single side) cross-talk as a function of pressure on two successive neighbouring elements. The gap between elements is $10 \mu\text{m}$.

4.4.5.4 Dynamic response

The dynamic response of a thermal detector array is related to the thermal time constant of the detector and, thus, depends on the equivalent heat capacitance of the bridge with materials on the top and should be computed using:

$$C_{eq} = \sum_{s=1}^n V_s \rho_s c_s \quad (4-20)$$

where V_s , ρ_s , c_s denotes the volume of the material, density of the material and the specific heat capacity of the material.

Although the transient simulation on the heat transfer can be completed by

FEM, the long computational time makes it impractical to use *FEM* for design optimization and the detector element has been expressed in terms of quadrupoles instead. The representation in quadrupoles basically allows a reduction of the dimension of the problem and the one-dimensional heat transfer equation, as is shown in the Eqn (4-19) in the Laplace domain, can subsequently be used [4.17][4.18]. Eqn (4-16), Eqn (4-17), Eqn (4-18) and Eqn (4-20) are used to calculate the equivalent parameters of bridge and are applied to the matrix coefficients (*A B C* and *D* shown in Figure 4-14) in such a way that a linear, passive and isotropic layer result is obtained:

$$\begin{pmatrix} \theta_{in} \\ \phi_{in} \end{pmatrix} = \begin{pmatrix} A & B \\ C & D \end{pmatrix} \begin{pmatrix} \theta_{out} \\ \phi_{out} \end{pmatrix} = \begin{pmatrix} \cosh\left(\sqrt{\frac{j\omega}{\alpha}}L\right) & \frac{1}{\lambda\sqrt{\frac{j\omega}{\alpha}}A_{cross}}\sinh\left(\sqrt{\frac{j\omega}{\alpha}}L\right) \\ \lambda\sqrt{\frac{j\omega}{\alpha}}A_{cross}\sinh\left(\sqrt{\frac{j\omega}{\alpha}}L\right) & \cosh\left(\sqrt{\frac{j\omega}{\alpha}}L\right) \end{pmatrix} \begin{pmatrix} \theta_{out} \\ \phi_{out} \end{pmatrix} \quad (4-21)$$

where θ_{in} and θ_{out} is the input and output Laplace temperature respectively, ϕ_{in} and ϕ_{out} the input and output Laplace heat flux respectively, $j\omega$ is the Laplace variable, L is the length of bridge, α is the thermal diffusivity and expressed by $\lambda/\rho c_p$, A_{cross} is the cross sectional area of bridge along the length coordinate.

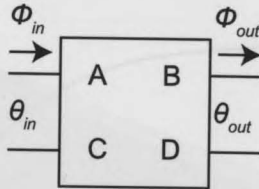


Fig. 4-14. Thermal quadrupole model of single linear passive and isotropic layer.

Since the matrix is linear and reversible, it can be considered the mathematical representation of the transfer function of the network composed of three thermal impedances in a "T" shaped circuit with: $Z_1 = Z_2 = (A-1)/C$, $Z_3 = 1/C$. Each bridge and air gap can be illustrated as a single quadrupole model as shown in the Figure 4-15. Due to symmetry of the configuration, only the part left or right from the main element needs to be considered.

The modulus of the thermal cross-talk is expressed in terms of the temperature increase of the neighbouring element relative to that of the heated element itself. The dynamic response of cross-talk to the side element (Figure 4-15) at 9.3 mBar pressure is shown in Figure 4-16.

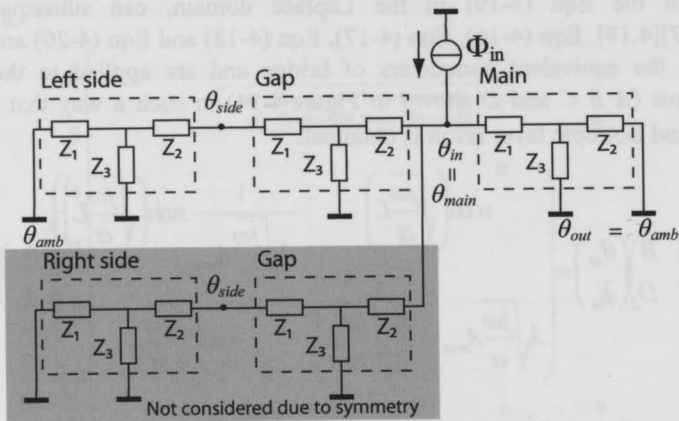


Fig. 4-15. Thermal quadrupole models of neighbouring elements with one gap spacing.

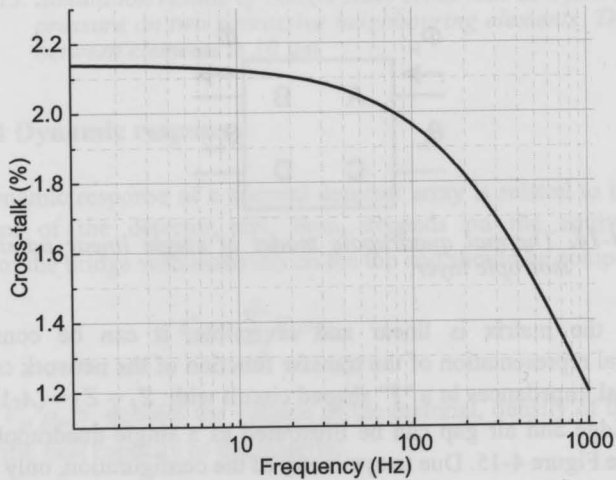


Fig. 4-16. Thermal modulus plot of the cross-talk at 9.3 mBar pressure.

4.5 Design a thermoelectric detector array for LVOF based microspectrometer

The *LVOF* is basically a continuous array of Fabry-Perot optical bandpass filters, arranged along the length of the *LVOF*, using a tapered optical resonance cavity, which results in mapping of the spectrum onto a lateral distribution over the length of the filter as shown in the Figure 4-17. The thermopile array is used to measure this optical intensity distribution. The *LVOF* is fabricated on the top of a silicon substrate in an *IC-compatible* fashion using reflow [4.19]. The taper is the center part of an interference filter and an *LVOF* results when dielectric mirrors are deposited on either side. The taper angle results in the wavelength of the pass-band of the local filter to change along the length of the *LVOF*. Consequently, collimated light passing through the *LVOF* is spectrally filtered and each pixel in the array measures the intensity of only the spectral component associated with its position in the array. Therefore, the resolution of an *LVOF* is high and the system resolution is determined by the pitch of detector array.

A larger size of the single element of the detector would produce higher throughput, which is at the expense of the spectral resolution. Hence, the size and pitch are essentially decided by the specific application. For the first design, the dimension of the *TE* element is practically selected as same as group 1 in the design of the grating-based microspectrometer.

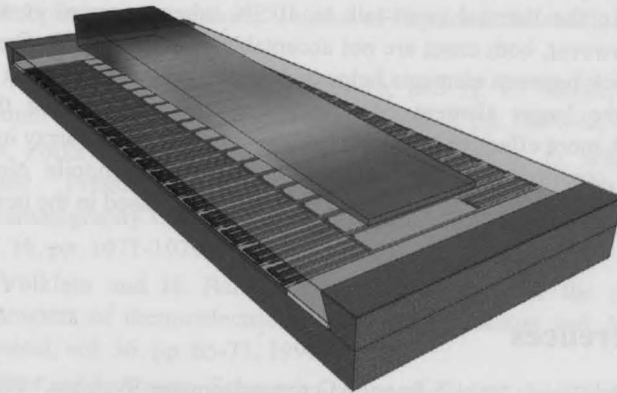


Fig. 4-17. Illustration of the LVOF based IR micro-spectrometer.

4.6 Conclusion

The principle of the thermoelectric effect followed by the theoretical analysis and modeling of the thermopile array for use in a miniaturized infrared microspectrometer are discussed in this chapter. A high figure of merit Z of the thermoelectric material is essential for high TE performance. Polysilicon is the thermoelectric material of choice and applied in the following chapters because of its acceptable figure Z and $CMOS$ compatibility.

The design of the thermopile detector array is dictated by the optical properties of the dispersive element of the spectrometer. Two types of dispersive element are proposed: grating and $LVOF$. For the grating-based design, the final device structure is on the basis of an analytical and numerical model and is planned for the application in the 1.5–3 μm wavelength range. Taking account of the constraints of a spectral pattern imposed by the microspectrometer diffractive imaging grating, the main dimension of sensing elements could not be fixed.

After determining the size and number of thermocouples in each thermopile, the performance can be estimated by the analytical model. Subsequently, simulations have been performed using $COMSOL$. The resolving power is maximum at the centre element of the array $R=68$ and the calculated sensitivity is $S = 289 \text{ V W}^{-1}$, when assuming a perfect blackbody absorber in the case of bulk micromachining. A spacing of 4 μm between elements limits the cross-talk of adjacent elements to 19% theoretically, whereas a gap spacing of 10 μm results in the thermal cross-talk to 10.3% when operated at atmospheric pressure. However, both cases are not acceptable in a practical device operation. A wider trench between elements helps to decrease cross-talk, but not efficiently. Moreover, the larger element pitch in the array would reduce the spectral selectivity. A more effective solution is to properly operate the array in a vacuum, which also contributes to the sensitivity of each thermopile element. The technology implication of an evacuated device are discussed in the next chapter.

4.7 References

- [4.1] G. de Graaf, "Mid-Infrared Microspectrometer Systems," Ph.D. Thesis, Delft University of Technology, 2008.

- [4.2] A. W. Van Herwaarden and P. M. Sarro, "Thermal sensors based on the seebeck effect," *Sensors and Actuators*, vol. 10, pp. 321-346, 1986.
- [4.3] A. Graf, M. Arndt, and G. Gerlach, "Seebeck's effect in micromachined thermopiles," *Proc. Est. Acad. Sci., Eng.*, vol. 13 pp. 338-53, 2007.
- [4.4] A. D. McConnell, S. Uma, and K. E. Goodson, "Thermal conductivity of doped polysilicon layers," *Microelectromechanical Systems, Journal of*, vol. 10, pp. 360-369, 2001.
- [4.5] F. Völklein, A. Wiegand, and V. Baier, "High-sensitivity radiation thermopiles made of Bi-Sb-Te films," *Sensors and Actuators A: Physical*, vol. 29, pp. 87-91, 1991.
- [4.6] R. P. Ribas, "Maskless Front-Side Bulk Micromachining Compatible to Standard GaAs IC Technology," TIMA-CMP, Grenoble Cedex, France.
- [4.7] D. M. Rowe, *Handbook of Thermoelectrics*. Boca Raton., USA: CRC Press, 1994.
- [4.8] A. Schaufelbühl, "Thermal imagers in CMOS technology," Ph.D. Thesis, Physical Electronics Laboratory, Swiss Federal Institute of Technology (ETH), Zürich, 2002.
- [4.9] COMSOL Multiphysics 3.2; www.comsol.com.
- [4.10] ZEMAX, "Optical Design Program, User's Guide, Version 9.0 ", ed. Tucson, AZ: Focus Software, Inc., 2000.
- [4.11] S. H. Kong, "Infrared Micro-Spectrometer Based on a Multi-Slit Grating," Ph.D. Thesis, Delft University of Technology, 2002.
- [4.12] A. W. van Herwaarden and P. M. Sarro, "Performance of integrated thermopile vacuum sensors," *Journal of Physics E: Scientific Instruments*, vol. 21, p. 1162, 1988.
- [4.13] A. W. van Herwaarden, P. M. Sarro, and H. C. Meijer, "Integrated vacuum sensor," *Sensors and Actuators*, vol. 8, pp. 187-196, 1985.
- [4.14] J. A. Potkay, G. R. Lambertus, R. D. Sacks, and K. D. Wise, "A Low-Power Pressure- and Temperature-Programmable Micro Gas Chromatography Column," *Microelectromechanical Systems, Journal of*, vol. 16, pp. 1071-1079, 2007.
- [4.15] F. Völklein and H. Baltes, "Optimization tool for the performance parameters of thermoelectric microsensors," *Sensors and Actuators A: Physical*, vol. 36, pp. 65-71, 1993.
- [4.16] D. Pitts and L. Sissom, *Schaum's Outline of Theory and Problems of Heat Transfer*. New York: McGraw- Hill, 1998.

- [4.17] D. Maillet, S. André, J. C. Batsale, A. Degiovanni, and C. Moyne, *Thermal Quadrupoles: Solving the Heat Equation through Integral Transforms*. New York: Wiley, 2000.
- [4.18] S. Andre, B. Remy, D. Maillet, A. Degiovanni, and J.-J. Serra, "Modulated photothermal radiometry applied to semitransparent samples: Models and experiments," *Journal of Applied Physics*, vol. 96, pp. 2566-2575, 2004.
- [4.19] A. Emadi, H. Wu, S. Grabarnik, G. de Graaf, and R. F. Wolffenbuttel, "Vertically tapered layers for optical applications fabricated using resist reflow," *Journal of Micromechanics and Microengineering*, vol. 19, p. 074014, 2009.

Micromachining Technology for the Thermo-Electric Detector

5

5.1 Introduction

This chapter gives an overview of the basic micromachining techniques that are used for fabrication of the thermoelectric detector in the *IR* microspectrometer. Moreover, this chapter serves on an introduction to the processing discussed in subsequent chapters. Among semiconductor materials, the most frequent applicable material is silicon owing to well-known mechanical and electrical properties and the well-developed technology, which makes silicon an excellent material for integrated microsystems. Since the micro-technology has been developed for decades, the final goal is to combine micro-scale sensor and the readout realized in a *CMOS* process. In general the planar wafer is processed into three-dimensional structures by micromachining technologies after the standard *IC* fabrication procedures to enable the addition of three-dimensional structures.

Micromachining involves lithography and the selective removal of a material by using etching techniques [5.1]. A combination of etchants and materials is used to make the etching process selective to one region or orientation. The thermoelectric detector array is fabricated by selecting the proper micromachining technique depending on the application. Two basic groups of

micromachining technologies are available: bulk and surface micromachining. Each has its specific advantages and disadvantages.

5.2 Bulk micromachining

The schematic configuration is shown in Figure 5-1(a). The bulk micromachining example demonstrates a mechanical support or masking material layer, taking the silicon nitride for instance, deposited on a flat and polished silicon substrate which is subsequently removed. This mechanical structure could be used as a sensor or be placed on an independently processed chip to form an assembled device. To free-standing the structure, the bulk silicon should be removed to achieve the thermal insulation in the thermoelectric application. The etching techniques are categorized as: dry and wet etching.

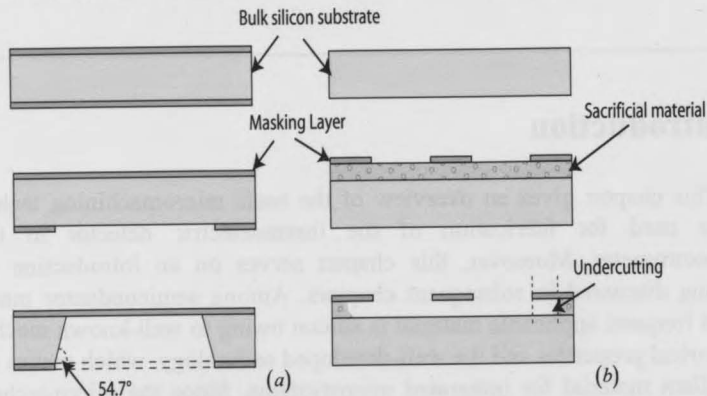


Fig. 5-1. Schematic of bulk micromachining (a) and surface micromachining (b).

In dry etching, two distinctly different etch mechanisms are encountered. During the sputter etch process, ions of inert gases for example argon are accelerated to the surface such that atoms are knocked off due to momentum transfer. The etch products are not volatile and the process is not selective. On the other hand, volatile products are formed and the process is selective in the chemical etching process. A combination of sputter etch and chemical etch processes is used in *RIE*. Inert gases, reactive gases containing fluorine, chlorine, bromine, or oxygen are applied. Ions are accelerated toward the surface to make

the surface more reactive. It results in the straight vertical side wall compared to wet etching [5.2]. Since the *MEMS* structure is released by wet etching in our application, techniques that has been implemented are discussed in the following section.

5.2.1 Wet etching of silicon

Wet etching covers the techniques that remove materials by soaking the wafer or sample in an etch bath that contains the liquid chemical etchant. These techniques offer relatively fast etch rates at low cost. The features and targets of the etching depth can be determined in a number of ways. The process can be stopped after a predetermined time period if the etching rates are predictable. Another practical way is to use etch stops which give more precise results. These depend on the combinations of material used, which necessarily include materials that are etched much more slowly than the material to be etched. Among anisotropic etchants are, for instance, ethylenediamine (*EDA*) and Tetramethylammonium hydroxide (*TMAH*). A popular etchant is potassium hydroxide (*KOH*) [5.3]. The benefits are the high etching rate, the good selectivity, the low toxicity and the low cost. The general etch mask for *KOH* is nitride which provides the longer etching periods. Anisotropic etch at different rates in different crystallographic orientations which give better control over the resulting shape as shown in Figure 5-1.

5.3 Surface micromachining

The mechanical layers are formed typically on top of sacrificial layers. An often used sacrificial layer is silicon dioxide that are subsequently removed in the case of surface micromachining. This procedure allows for fabricating for example cantilevers as illustrated in the Figure 5-1(b). With surface micromachining, thin layers are formed as a stack on top of the wafer surface, whereas bulk micromachining uses the whole depth of the silicon wafer and also involves removing significant portions of the substrate material.

5.3.1 Wet etching of oxide

Wet etching covers the techniques that remove materials by soaking the sample or wafer in a container which comprises the liquid chemical etchant. These techniques provide the benefits rapidity, simplicity and low cost. Another advantage results from the rounding of sharp anisotropic corners avoiding stress concentration considerably lowered the yield. The common sacrificial (unwanted) materials in *CMOS-MEMS* are silicon and oxide. Since oxide is used as sacrificial material in our application, the oxide removing technique is addressed.

A very selective chemical for SiO_2 is *HF*. *HF* is universally used as a buffered solution in industry application. The consequence is the slower etch rate but constant and less aggressive action on the oxide. The etch rate at room temperature can range from 100 to 250 nm/minute depending on the actual density of the oxide. For instance a compact structure can be thermally grown and a less compact oxide can be grown by chemical vapour deposition. The slow etch rate of oxide would result in long time in the case of our thermoelectric array release. The industry standard is buffered hydrofluoric acid solution (*BHF*) which has a relatively low etch rate of oxide, but the advantage is the low etch rate of metal. However, this metal etch rate cannot be ignored in case of a long sacrificial releasing time. Another option of releasing structure is using 73% concentration *HF* [5.4]. *HF* at 73% concentration is used as the etchant, because it provides a relatively slow etch rate of aluminium. The actual etch rate was determined by initial tests and was found to be 1740 nm per minute. After sacrificial etching, the wafer or sample should be prepared for the next process step by rinsing and drying. Moreover, stiction is an issue at that stage.

5.4 Methods to prevent stiction

Surface microstructures have large lateral dimensions compared with the thickness and distance (gap) from the substrate. The large surface-area-to-volume ratios of surface and bulk micromachined micro mechanisms enlarge the effect of surface and interfacial forces [5.5]. Stiction is a term that has been applied to the unintentional adhesion of compliant microstructure surfaces when restoring forces are unable to overcome surface tension and interfacial forces such as capillary, chemical, van der Waals and electrostatic attractions. Figure 5-2 shows the optical micrograph of *MEMS* bridge device with/without stiction under the

optical microscope. The center part of bridge is stuck to the bottom of the silicon wafer while both ends of the bridge remain standing. As a result, the interference pattern, also called meniscus, is shown in between the center and end part. Therefore, the release process plays a crucial role for *MEMS* devices fabricated by surface micromachining. The commonly distinguished techniques are: evaporation drying [5.6], freeze-drying (sublimation) [5.7], super critical CO_2 drying [5.8], wet release [5.9], flash release [5.10], and vapour *HF* release [5.11]. The following sections present the freeze-drying and vapour *HF* techniques used for releasing the *IR* thermoelectric detector array.

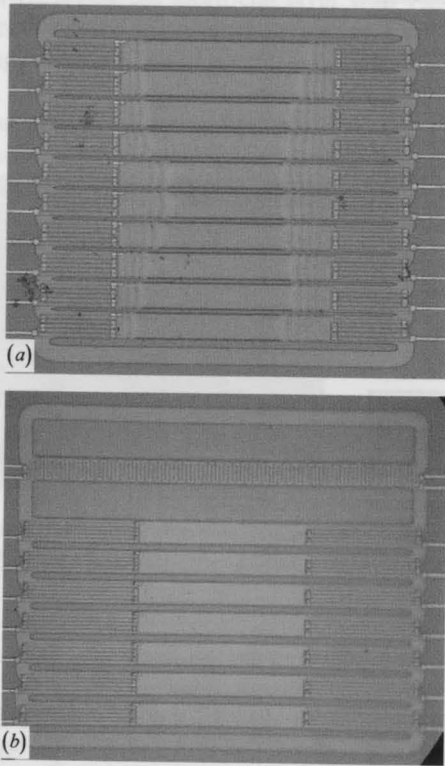


Fig. 5-2. *MEMS* bridges with stiction (a) and free standing (b).

5.4.1 Freeze-drying

An elegant way to solve the stiction problem is based on freeze drying. The

freeze drying method was developed for MEMS device using chemical Cyclohexane, which freezes at about 7 °C, as the final rinsing agent [5.7]. Freezing and subsequent sublimation are readily accomplished by placing the substrate under a nitrogen flow on a regulated Peltier element with a temperature below the freezing point. The total time for the freeze-sublimation process depends on the geometry of the sample and is typically 15-30 minutes for the structures described in this thesis.

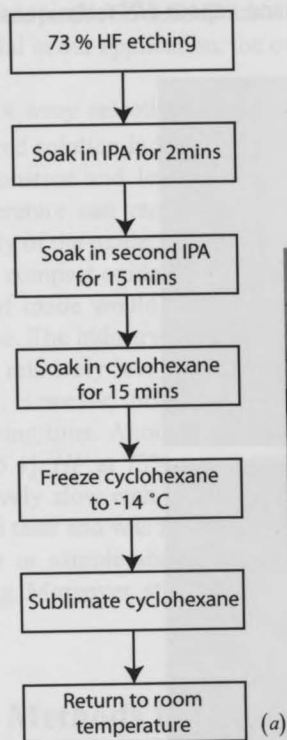
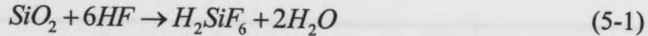


Fig. 5-3. Procedure of freeze-drying (a) and Peltier set-up (b).

The procedures are shown in Figure 5-3 and can be explained as follows: after sacrificial-layer etching in a high concentrated 73% HF solution, a dilution rinse in Isopropyl alcohol (IPA) is performed to remove the etchant. The samples should be immersed in the solution while placed from one beaker to another one. The samples are moved to second beaker with IPA to keep the hydrophobic wafer surface wet for 15 minutes using a magnetic spinner. The samples are placed in

cyclohexane, the final rinsing agent using a magnetic spinner. The *IPA* serves as an intermediate mixing agent. After rinsing the wafer in cyclohexane, it is placed on a Peltier element that has already been cooled to $-14\text{ }^{\circ}\text{C}$. A nitrogen flow aids the sublimation process by removing cyclohexane vapours and preventing condensation of water. The set-up shown in Figure 5-3 is installed in *MEMS* laboratory of *DIMES*. After sublimation is finished, the Peltier element is raised to room temperature, which completes the fabrication of the free-standing structures.

The notion of removing the sacrificial layer with vapour phase etching is very attractive, since it circumvents the whole sequence of etching, rinsing steps, and elaborate drying procedure. Another advantage is that no meniscus is formed during the release. Since the sacrificial material is oxide, only the removal of oxide with vapour etching is addressed. During the etching process, the condensation of water on the etching surface renders the process not so dry, and dilutes the *HF*. The consequence is the increased etch rate of metal used at the electrical interconnection. The condensation cannot simply be avoided since water molecules are produced on surface as the result of the chemical reaction for oxide etching described as [5.12]:



This problem can be solved by heating the sample during vapour *HF* etching and preventing excessive water condensation. The heat can be applied to the wafer via conduction or radiation. In the radiation approach, the lamp is placed at some distance to warm the sample [5.13]. Here, the resistive heater is used to generate the heat to remove the condensation of water. In the *MEMS* laboratory of *DIMES*, the free-standing *MEMS* structure is released by vapour etching.

Figure 5-4 schematically illustrates our experimental apparatus. An aqueous solution of 73% *HF* is kept in a Teflon beaker and vaporized to induce a chemical reaction with silicon oxide. A dish made of metal or Teflon is used to cap the *HF* vessel to keep the *HF* vapor inside. A resistive heater is utilized in order to warm up the sample and to control the temperature during this process. For better uniformity of etching, the sample is set upside down to the *HF* vapor. The sample can be fixed on the dish by photoresist or scotch tape.

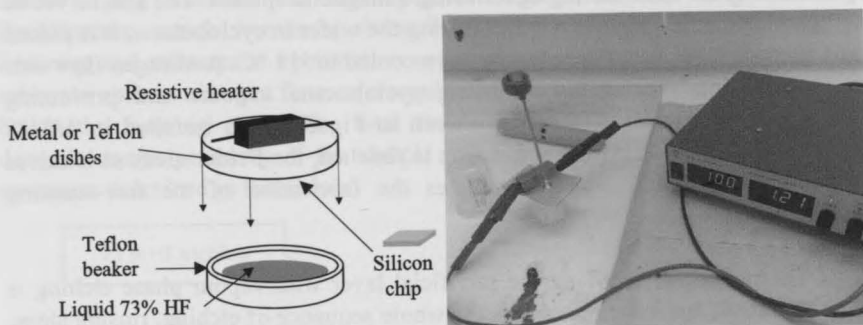


Fig. 5-4. Schematic illustration of the vapour HF set-up.

As mentioned earlier, the purpose of removing the generated water is to significantly reduce the etch rate of the metal used at the absorbers and the electrical interconnection. The oxide etching rate is 600 nm per minute at a temperature of 30 °C. Higher temperatures would decrease the etch rate dramatically.

5.5 Conclusion

Several standard micromachining techniques are discussed in this chapter and would be further developed in the following chapters. By using bulk micromachining the thermoelectric detector can be released by removing the excess silicon under the device. Since the removed silicon is part of the substrate, the thermal insulation is superior than the case of device etched by surface micromachining. Unfortunately, drawbacks of using bulk micromachining are: long etching time and the stress concentration at the interface between silicon and the device which could lower the yield of whole process. Moreover, the wafer is typically not possible to re-enter the clean room to be further processed, for instance for thin-film encapsulation.

The devices released by surface micromachining can be further processed under the subject of IC compatibility issues. The comparison of both micromachining techniques is shown in Table 1. Because of the surface tension and capillary force, stiction is introduced and should be prevented. Both freeze-drying and vapour HF etching techniques are applied and results in high yield

after the process. The comparison of freeze-drying technique and vapour *HF* is shown in Table 2.

TABLE 1. Comparison of bulk and surface micromachining for thermoelectric detector array.

	Bulk micromachining	Surface micromachining
Integration with CMOS electronics	challenge	possible
Etching time	long	short
Post-processing	not possible	possible
Device performance	high	low

TABLE 2. Comparison of freeze-drying and vapour *HF* for prevent stiction.

	Freeze-drying	Vapour <i>HF</i> using labware
Type	liquid phase	vapour phase
Etching time	short	long
Reproducibility	good	moderate
Over process complexity	high	possibly low
Stiction free yield	high	high

5.6 References

- [5.1] G. T. Kovacs, *Micromachined Transducers Source book* McGraw-Hill Higher Education, 1998.
- [5.2] M. J. Madou, *Fundamentals of microfabrication: the science of miniaturization*: CRC Press, 2001.

- [5.3] D. B. Lee, "Anisotropic Etching of Silicon," *Journal of Applied Physics*, vol. 40, pp. 4569-4574, 1969.
- [5.4] P. T. J. Gennissen and P. J. French, "Sacrificial oxide etching compatible with aluminum metallization," in *Solid State Sensors and Actuators, 1997. Transducers '97 Chicago., 1997 International Conference on, 1997*, pp. 225-228 vol.1.
- [5.5] R. Maboudian, W. R. Ashurst, and C. Carraro, "Tribological Challenges in Micromechanical Systems," *Tribology Letters*, vol. 12, pp. 95-100, 2002.
- [5.6] T. Abe, W. C. Messner, and M. L. Reed, "Effects of elevated temperature treatments in microstructure release procedures," *Journal of Microelectromechanical Systems*, vol. 4, pp. 66-75, 1995.
- [5.7] R. Legtenberg and H. A. C. Tilmans, "Electrostatically driven vacuum-encapsulated polysilicon resonators Part I. Design and fabrication," *Sensors and Actuators A: Physical*, vol. 45, pp. 57-66, 1994.
- [5.8] C.-J. Kim, J. Y. Kim, and B. Sridharan, "Comparative evaluation of drying techniques for surface micromachining," *Sensors and Actuators A: Physical*, vol. 64, pp. 17-26, 1998.
- [5.9] S. Pamidighantam, W. Laureyn, C. Rusu, K. Baert, R. Puers, and H. A. C. Tilmans, "A wet release process for fabricating slender and compliant suspended micro-mechanical structures," *Sensors and Actuators A: Physical*, vol. 103, pp. 202-212, 2003.
- [5.10] S. Deladi, V. Svetovoy, G. J. M. Krijnen, and M. C. Elwenspoek, "Flash release—an alternative for releasing complex MEMS devices," *Journal of Micromechanics and Microengineering*, vol. 14, p. 1659, 2004.
- [5.11] Y. I. Lee, K. H. Park, J. Lee, C. S. Lee, H. J. Yoo, C. J. Kim, and Y. S. Yoon, "Dry release for surface micromachining with HF vapor-phase etching," *Journal of Microelectromechanical Systems*, vol. 6, pp. 226-233, 1997.
- [5.12] J. H. Lee, H. H. Chung, S. Y. Kang, J. T. Baek, and H. J. Yoo, "Fabrication of surface micromachined polysilicon actuators using dry release process of HF gas-phase etching," in *Electron Devices Meeting, 1996. IEDM '96., International*, pp. 761-764, 1996.
- [5.13] Y. Fukuta, H. Fujita, and H. Toshiyoshi, "Vapor Hydrofluoric Acid Sacrificial Release Technique for Micro Electro Mechanical Systems Using Labware," *Japanese Journal of Applied Physics*, vol. 42, p. 3690, 2003.

TE Detector Array Fabricated by Bulk Micromachining

6

6.1 Introduction

This chapter discusses about the fabrication of a *TE* detector array for integrated *IR* microspectrometer based on an imaging diffraction grating in the 1.5-3 μm wavelength range using bulk micromachining. The detector array design should take technological limitations into account and should be adapted to the wavelength dependent resolution of the spectral pattern produced by the diffraction grating. Based on these optical specifications and fabrication limitations, the geometry and materials of detector array are determined and further optimized using the analytical model presented in chapter 4.

The structures for the sensing element in the array are cantilever-type and bridge-type. A nitride membrane structure fabricated by using *MEMS* technologies enables an effective thermal insulation, which highly contributes to the sensitivity of the detector. Optimal parameters have been used in the layout of a single detector from the results of the analytical model and the *FEM*. Other dimensions are dictated by the specified optical resolution. The device is fabricated using a *CMOS* process, followed by *KOH* wet-etching and subsequent *RIE* to separate the elements.

6.2 IC-compatible fabrication of the thermopile array

The fabrication was done in *DIMES* facility of TUDelft with a standard *CMOS* process followed by a backside bulk-micromachining step. Six masks are used for the front side processing of the wafer and one additional mask for the micromachining from the backside of the wafer. The process sequence is shown simplified in Figure 6-1.

Wafer processing started with the deposition of 700 nm of low stress *SiN* film formation and then several process steps followed. Firstly, a 300 nm low-stress *PolySi* layer was grown by low pressure chemical vapor deposition (*LPCVD*). Secondly, Boron was implanted at 40 keV and $5 \times 10^{15}/\text{cm}^2$ to realize p-type *PolySi*. After the cleaning procedure, n-type *PolySi* was formed by Phosphorous doping (40 keV and $7.5 \times 10^{15}/\text{cm}^2$). Thirdly, *RIE* was applied to remove *PolySi* from the backside and unwanted *PolySi* from the front side. In the next step, 100 nm low-stress *SiN* was deposited by *LPCVD* to make the insulation between metal contacts and *PolySi*. Aluminium was deposited and patterned on top to define the connection of thermocouples and bonding pads. Finally, the wafer was processed with *KOH* wet etching to make the membranes for the better thermal insulation.

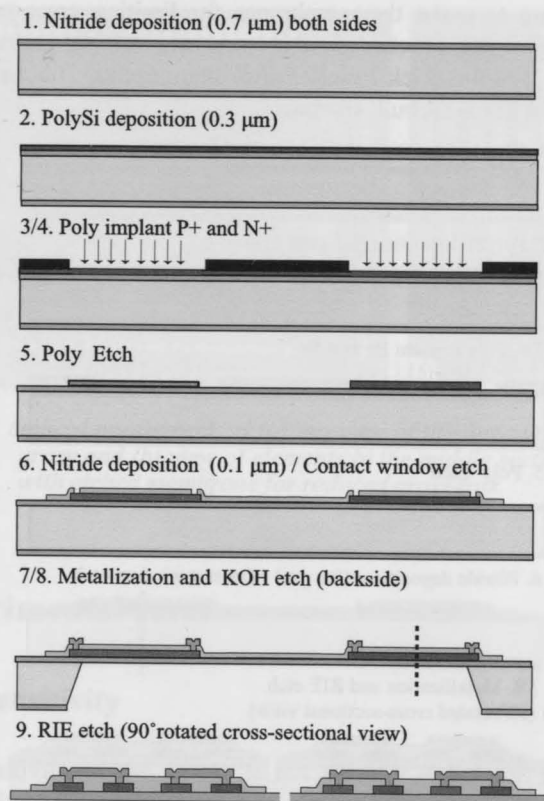


Fig. 6-1. Post-CMOS fabrication sequence (cross-sectional view).

RIE was used to realize the gap between thermopiles for limiting thermal cross-talk. The total stress of wafer is a tensile stress with 2190 Mpa. The yield of bridges etched-cut of the membrane is strongly affected by this stress level. Therefore, the fabrication sequence is modified to keep 21 μm silicon underneath *SiN* membrane shown in Figure 6-2. The modified fabrication sequence is stated as followed: After the metallization step, the next is to cut the 10 μm wide trench between elements, which was etched to 21 μm depth. A silicon layer of variable thickness up to 21 μm was left underneath the bridges and used for experimenting with the compromise between the improved mechanical strength at larger thickness versus the loss of sensitivity due to the increased thermal conductivity

through the bridge suspension. In the final step the wafers were processed with *KOH* wet etching to make the membranes for limiting cross-talk. The final detector array has sandwiched bridge structure which includes 100 nm passivation *SiN*, 300 nm thick *PolySi-PolySi* thermopiles, 700 nm thick nitride layer and up to 20 μm thick bulk silicon.

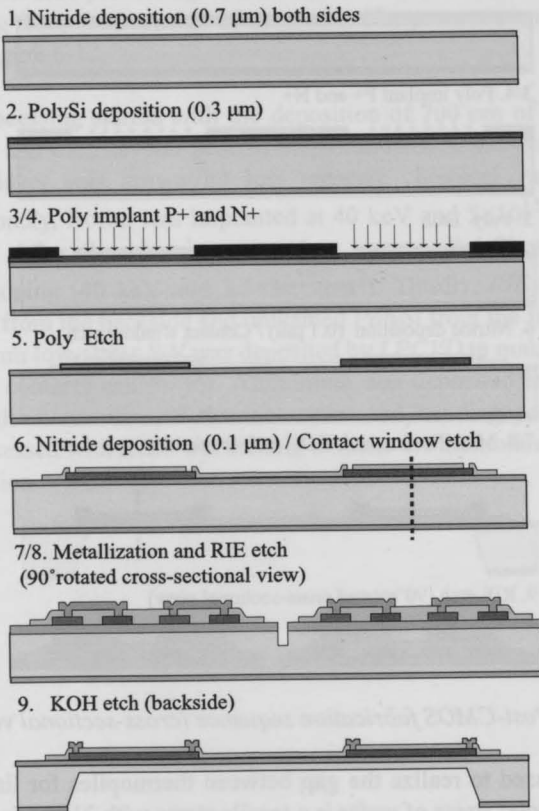


Fig. 6-2. Modified fabrication sequence.

The yield of structures fabricated by using the modified process is significantly improved. The disadvantage is the reduced sensitivity, since the thermal conductivity of remaining silicon contributes to the total thermal conductivity of membrane. Figure 6-3(a) shows the completed scaled thermopile array and (b) shows the bridges in the middle section of the array with dimension of $650 \times 36 \mu\text{m}^2$ and 10 μm wide trenches in between the bridges.

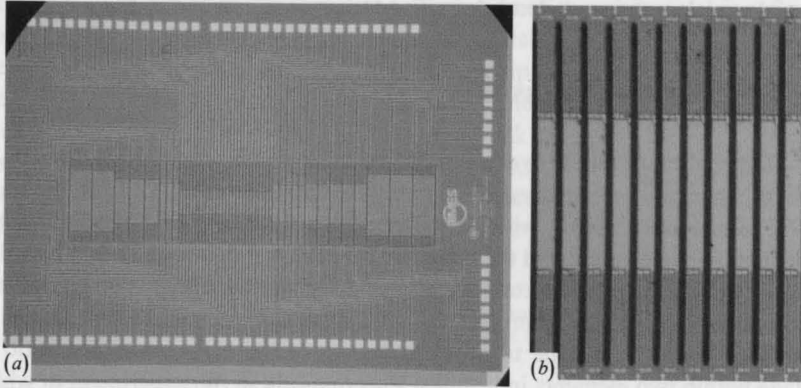


Fig. 6-3. Optical micrograph of (a) top view of the unequally sized TE array and (b) view of elements in the middle section of array with etched membrane for reduced cross-talk.

6.3 Experimental results

6.3.1 Sensitivity

The sensitivity of the device is not actually tested for several reasons. Firstly, the estimated performance of the device is low, because of the existence of the excess silicon underneath of *SiN* thin film membrane. The result is high thermal leakage (low thermal resistance) from the middle of the bridge to the substrate. Thermal resistance of material can be presented by thermal conductivity and dimension of material. In silicon, the thermal conductivity is of $148 \text{ Wm}^{-1}\text{k}^{-1}$ while *SiN* has only $1.6 \text{ Wm}^{-1}\text{k}^{-1}$ [6.1]. Since the wet etching is stopped earlier, the thickness of silicon is at least 20 times higher than *SiN*. Therefore, the excess of silicon has much lower thermal resistance and contributed to the overall thermal resistance of the original design.

The second reason is lack of proper *IR* light source at that time. Unfortunately, our instrument set-up has insufficient optical power at this time. Therefore, the Seebeck output of the thermopile is less than the noise level of the

system for the proper measurement. As a result, the sensitivity of the device along spectral wavelength is not clearly examined.

6.3.2 Thermal cross-talk

Thermal cross-talk between two *TE* elements in the array with 4 and 10 μm wide trenches has been measured in a vacuum chamber using a 14 μm diameter He-Ne laser spot (*FWHM*), which is chopped at a frequency of 2 Hz. The spot is projected on one element and the resulting Seebeck voltage is measured by using a HP 34420A nano-voltmeter. Simultaneously, the Seebeck voltage of the neighbouring element is recorded. The first experimental result is measured by the bridge with 4 μm wide trenches as shown in the Figure 6-4. The ratio of voltage within two elements indicates a 9% cross-talk in the experiment in which the simulation gives the cross-talk of 9,5% theoretically.

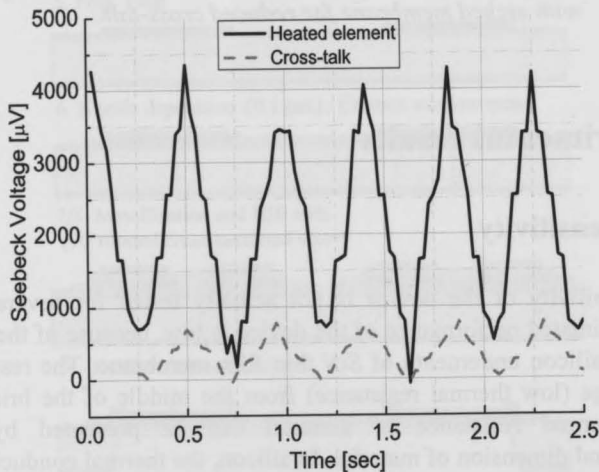


Fig. 6-4. Cross-talk measurement result of two neighbouring bridges with 4 μm trenches.

The experimental results of cross-talk as a function of the air pressure are presented in the Figure 6-5. The results indicate that cross-talk is determined by both thermal heat leakage through the gap to the neighbourhood element and on the optical leakage from the laser spot contributes the cross-talk.

The optical cross-talk is inherent to the measurement techniques. First, the scattering light due to the uncompleted absorption of the main pixel is reflected from the bottom plate of packaging to the side pixels. Secondly, the glass cap of the vacuum chamber directly on the top of the chip results in some scattering in the laser light. The optical light leakage is determined by a separate measurement under the very low air pressure, where the cross-talk caused by the heat transfer is assumed negligible. The corrected result coincides perfectly with the *FEM* simulation result. The deviation at higher pressures is mainly from the convection.

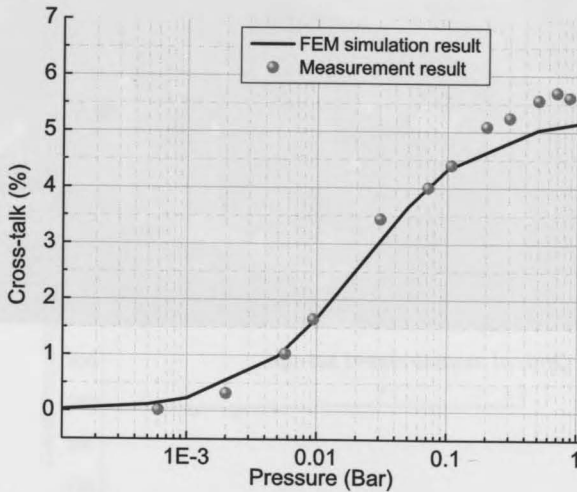


Fig. 6-5. Cross-talk (on single side) measurement of elements with $10\ \mu\text{m}$ trenches under different pressure.

An extension of this measurement technique has made good use of measuring the dynamic thermal response of a single element and the thermal cross-talk between elements. The laser spot is frequency modulated for this purpose. The measurement setup includes He-Ne laser, an optical chopper, a vacuum chamber, lock-in amplifier *SR830* for measuring thermal modulus plot and a digital oscilloscope for recording the thermal time constant to validate the *AC* response. The entire optical measurement set-up is shown in Figure 6-6. The thermal modulus plot of three elements with the heated (illuminated) pixel in the middle at 1 mBar is shown in the Figure 6-7(a). The measured thermal cross-talk (corrected for optical leakage) is 0.4% (single side), which conforms with the simulation. The cut-off frequency of the main pixel and the side pixel in the

TE Detector Array Fabricated by Bulk Micromachining

measurement of the atmosphere pressure is at 240 Hz and 183 Hz respectively. The cut-off frequency of the side pixel is lower than that of the heated pixel, because of the higher thermal resistance of the air gap. The cut-off frequencies are not significantly affected by air pressure, as is demonstrated in Figure 6-7(b).

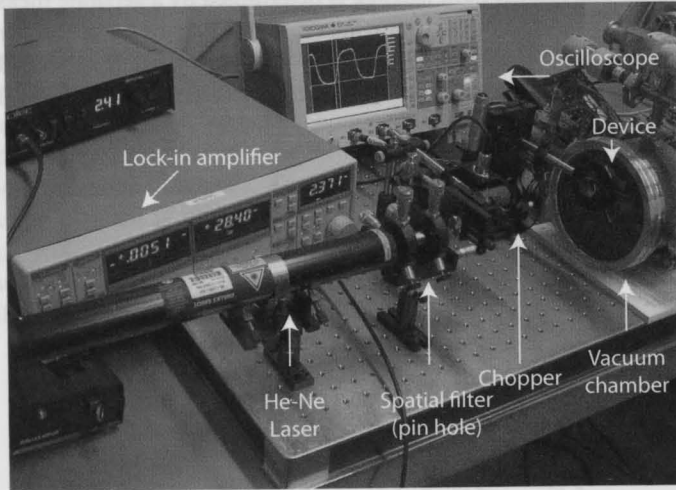


Fig. 6-6. Optical measurement set-up.

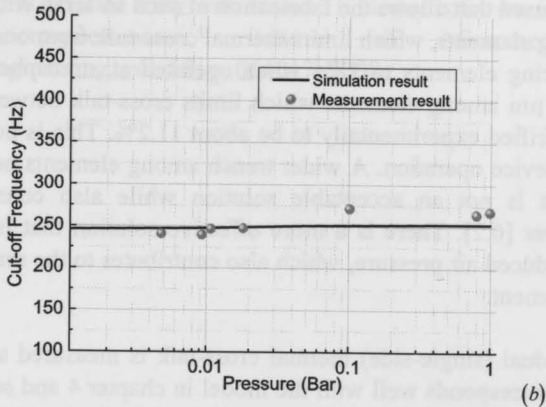
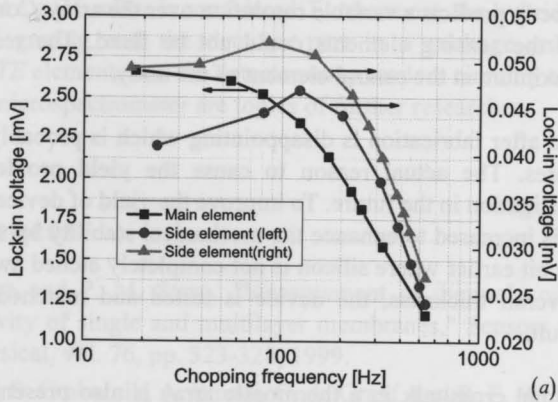


Fig. 6-7. (a) Thermal modulus plot of three elements at 1mBar pressure. (b) Cut-off frequency of heated element under different pressure.

6.4 Conclusion

The design and fabrication of a CMOS compatible thermopile array for use in a miniaturized IR microspectrometer has been presented. The design of the thermopile detector array is dictated by the optical properties of the imaging

grating. The ultimate device structure is based on the analytical and numerical model and is intended for the application in the 1.5-3 μm wavelength range. The modeling correctly predicts a variable resolution over the array. Consequently, the dimensions of the sensing elements could not be fixed. The resolving power reaches the maximum at the central element of the array.

The yield after fabrication is disappointing which is probably due to stress in the structures. The actual reason to cause the yield problem still needs advanced investigation in the future. To improve the yield of device, the thickness of membrane is increased to enhance the mechanical stability by stop *KOH* wet-etching a little bit earlier where silicon is not completely etched away. According to the new overall thickness, the device is tested and matched the modified simulation result.

The thermal cross-talk in a thermopile array is also presented. A process flow has been used that allows the fabrication of such an array with a gap spacing of 4 μm among elements, which limits thermal cross-talk from one element to the two neighbouring elements to 18% when operated at atmospheric pressure. A spacing of 10 μm among elements which limits cross-talk between the adjacent elements is verified experimentally to be about 11.2%. This is not acceptable in the practical device operation. A wider trench among elements helps to decrease cross-talk, but is not an acceptable solution while also considering optical resolving power [6.2]. There is a more effective solution that is to operate the array under reduced air pressure, which also contributes to the sensitivity of each thermopile element.

The residual (single-side) thermal cross-talk is measured at 2 mBar to be 0.6%, which corresponds well with the model in chapter 4 and acceptable in the *IR* microspectrometer. The bandwidth at the given dimensions was at 240 Hz for the radiated main element due to its suspension and at 183 Hz for the side element due to cross-talk. This result is in the nice agreement with the simulations, which also indicate a pressure independent cut-off frequency. Convection losses have been observed at pressure levels beyond 100 mBar.

The measurement results do validate the model, while these reveal a deviation at the higher end of the pressure range, which is due to convection. In future work the convection effect through gap should be thoroughly included and carefully analyzed to have more accurate models. The devices of the slightly different dimensions will be fabricated to advanced study the effects of the

process variations on the performance. The packaging becomes simpler in case the air pressure can be kept at a higher level. Therefore, a design optimization for the operation at e.g. 10 mBar is considered. Furthermore, the hybrid integration of the optimized grating and the detector part in a package and the on-chip integration of *TE* elements and the detector array readout circuitry to yield a fully-integrated *IR* microspectrometer are topics of further researches.

6.5 References

- [6.1] A. Irace and P. M. Sarro, "Measurement of thermal conductivity and diffusivity of single and multilayer membranes," *Sensors and Actuators A: Physical*, vol. 76, pp. 323-328, 1999.
- [6.2] H. Wu, S. Grabarnik, A. Emadi, G. de Graaf, and R. F. Wolffenbuttel, "A thermopile detector array with scaled TE elements for use in an integrated IR microspectrometer," *Journal of Micromechanics and Microengineering*, vol. 18, p. 064017, 2008.

7.1 Introduction

This chapter introduces a membrane array structure, a MEMS device that is tailored to capture infrared energy. The structure is designed and fabricated to achieve good absorption of IR energy. The device is composed of two materials, thin and thick membranes, which are TE elements and is suspended. The thin membrane is used as a detector array, is suspended with a thin membrane, and the thick membrane is suspended with a thin membrane. The device is fabricated with a suspended bridge of MEMS and structures. The device is fabricated with a suspended bridge of MEMS and structures. The device is fabricated with a suspended bridge of MEMS and structures.

The design of this detector array was designed to detect IR energy and used to simulate the performance of the detector array. The structure is shown in Figure 7-1. The comparison between a thin membrane and a thermopile bridge, as compared to the structure with a suspended membrane of a conventional 3-layer thin film structure, the top membrane is the enough (around 1 μm) to perform the good absorption. The top membrane of the top metal layer is not critical when another thin film membrane layer is added on top. The relatively high absorption energy over 1 μm range IR wavelength range. The wide spectral range would make the device

The yield after fabrication is disappointing which is caused by the structure. The actual reason to cause the low yield is not clear. The reason may be the stress of the device or the stress of the substrate. The reason may be the stress of the device or the stress of the substrate. The reason may be the stress of the device or the stress of the substrate.

The residual (single-side) thermal cross-talk is measured at 2 mW to be 0.6%, which corresponds well with the model in chapter 4 and acceptable in the IR microspectrometer. The bandwidth of the given dimensions was at 240 Hz for the radiated main element due to its suspension and at 183 Hz for the side element due to cross-talk. This result is in the good agreement with the simulation, which also indicate a pressure independent out-of-frequency. Convective losses have been observed at pressure levels beyond 100 mbar.

The measurement results by validate the model, while these reveal a deviation at the higher end of the pressure range, which is due to convection. In future work the convection effect through gap should be thoroughly included and carefully analyzed to have more accurate models. The device of the slightly different dimension will be fabricated to advanced study the effects of the

TE Detector Array Fabricated by Surface Micromachining

7

7.1 Introduction

This chapter introduces a thermopile array fabricated in a *CMOS* process that is followed by surface-micromachining. An interference filter based absorber is included to achieve good absorption in *IR* range. The absorber is used, which is composed of two metallic layers and one resonance cavity on top of the *TE* elements and is intended for use in the near *IR* range from 1-4 μm . The infrared detector array is composed of 23 thermopiles, each with 5 thermocouples on a suspended bridge of $650 \times 36 \mu\text{m}^2$ dimensions. The deposition of the thin-film absorber is *CMOS* compatible and is followed by surface micromachining.

The design of this absorber has been discussed in chapter 3 on page 47 and used to simulate the absorptance of thin film stacks on the top of the *TE* element as shown in Figure 7-1. The comparison between different absorbers on top of the thermopile bridge, as compared to the uncoated bridge, is presented. For the case of a conventional 3-layer thin film absorber, the top *Ti* layer should be thin enough (around 5 nm) to perform the good absorption. However, the thickness of the top metallic layer is not critical when another thin-film (protective) dielectric layer is added on top. The relatively high absorption covers from 1.5 μm to 4 μm wavelength range. The wide spectral range would make the microspectrometer

suitable for mid-IR spectroscopy applications. The detector array is released by vapor HF. The residual after HF etching has to be removed in a sublimation process at low pressure. Experimental results and performance of the detector array are amply explained in the last section.

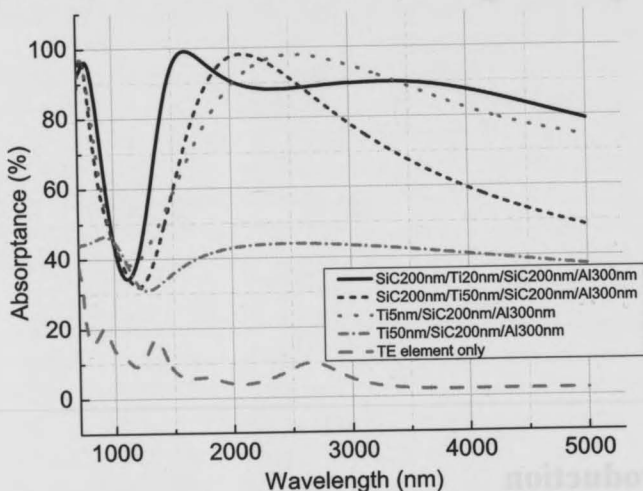


Fig. 7-1. Simulation of the absorptance in the IR spectral range.

7.2 Fabrication of the absorber

The fabrication of the thermopile detector array starts with the deposition of a 4 μm PECVD TEOS layer, which is used as the sacrificial layer. Mechanical layer with 700 nm of low stress SiN film is formed and then several process steps followed. Firstly, a 300 nm low-stress PolySi layer was grown by LPCVD. Secondly, Boron was implanted at 40 keV and $5 \times 10^{15}/\text{cm}^2$ to realize p-type PolySi. After cleaning procedure, n-type PolySi was formed by Phosphorous doping (40 keV and $7.5 \times 10^{15}/\text{cm}^2$). Thirdly, RIE was applied to remove PolySi from the backside and unwanted PolySi from the front side. In the next step, 100 nm low-stress SiN was deposited by LPCVD to make the insulation between metal contacts and PolySi. Finally, the wafer is proceeded for the fabrication of absorber.

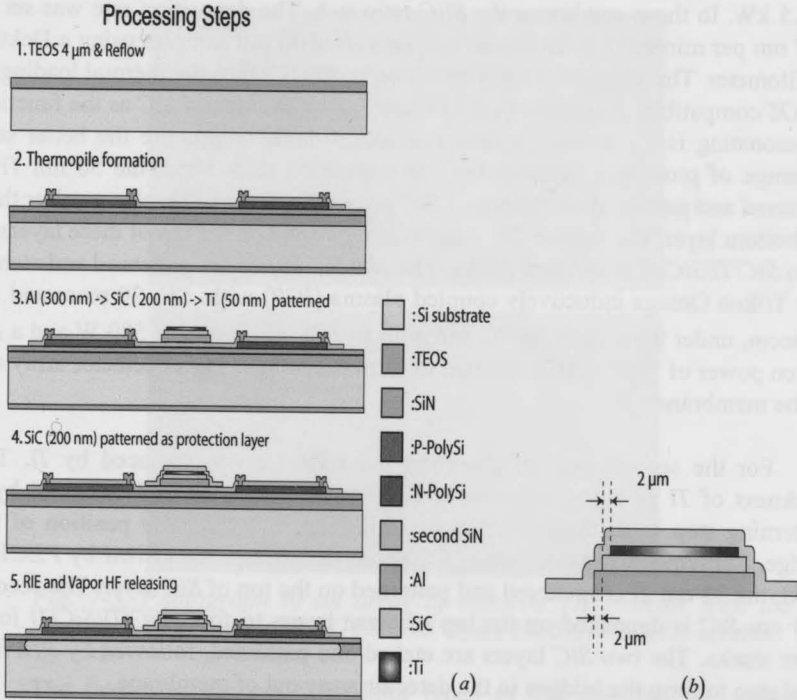


Fig. 7-2. Processing steps for the IR thermopile array with absorber (Dimension not to scale).

The essential steps for realizing the bridge structure and fabrication of absorber are described using Figure 7-2. The CMOS compatible bridge fabrication stops at the second SiN layer of 100 nm thickness and is followed by deposition of the layer stack used for the absorber. The contact hole etching and metalization are completed prior to the sacrificial etching. There are two types of the absorber are deposited on the TE detector array. Each of them has different thickness for reflector and impedance matching metallic layer.

For the first type of absorber 300 nm Al is sputtered, followed by a patterning step to define the thin film in the middle position of the bridge. Subsequently, SiC with a 200 nm thickness is deposited by the Novellus Concept One PECVD system using silane with a 0.1 sccm SiH₄ gas flow and methane with

a 4.11 sccm CH_4 gas flow. The pressure is 2.25 Torr and the frequency power set to 0.5 kW. In these conditions the Si/C ratio is 1. The deposition rate was set to 0.67 nm per minute. The thickness was measured on test samples using a Dektak profilometer. The temperature of deposition is 400 °C, thus the thermal loading is CMOS compatible. As shown in the Figure 7-2(b), the size of SiC as the function of resonating is 2 μm smaller than the bottom layer to procure the better step coverage of protection layer in the last deposition step. Next, the 50 nm Ti is sputtered and patterned on the top of SiC layer. The size of Ti is also smaller than the bottom layer. The second 200 nm SiC is deposited on the top of these layers to form $SiC/Ti/SiC/Al$ four-layer stacks. The two SiC layers are patterned and etched in a Trikon Omega inductively coupled plasma (ICP) with: SF_6 20 sccm and O_2 20 sccm, under 9.5 Torr at 10 °C, and with an ICP-RF power of 500 W and a RF platen power of 50 W. RIE is applied to form the bridges in the detector array out of the membrane.

For the second type of absorber, the reflector was replaced by Ti . The thickness of Ti as being reflector is 100 nm by sputtering and followed by a patterning step to distinctly define the thin film in the middle position of the bridge. Subsequently, a SiC layer of 200 nm thickness is deposited by PECVD. Next, the 30 nm Ti is sputtered and patterned on the top of SiC layer. The second 200 nm SiC is deposited on the top of these layers to form $SiC/Ti/SiC/Ti$ four-layer stacks. The two SiC layers are etched and patterned, followed by RIE in a final step to form the bridges in the detector array out of membrane.

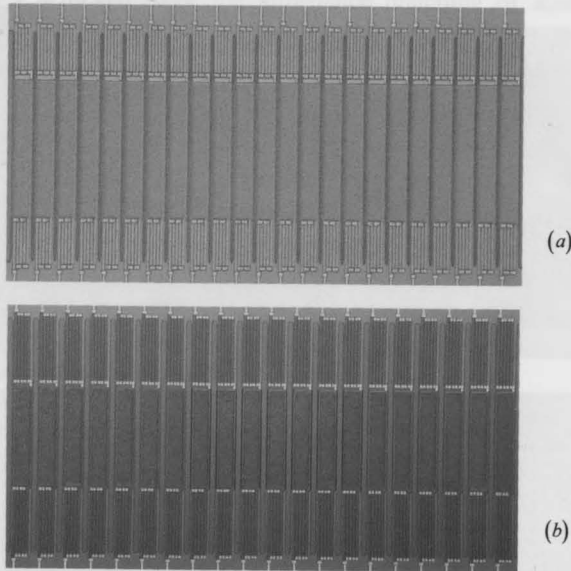


Fig. 7-3. Photograph of an array of infrared TE detector with the absorber: (a) SiC/Ti/SiC/Al layers (b) SiC/Ti/SiC/Ti layers.

The fabricated devices with both types of the absorber are shown in Figure 7-3 before the sacrificial release. The dimension of the detector array are $1.2 \times 0.76 \text{ mm}^2$, with an area of each pixel of $650 \times 36 \text{ }\mu\text{m}^2$ with a $40 \text{ }\mu\text{m}$ pitch for the first type of the absorber and a $46 \text{ }\mu\text{m}$ pitch for the second type. The absorber is deposited in the middle position of bridge with 5 thermocouples at the upper and lower side of bridge. The SEM photo shows the cross section of the first type of absorber in Figure 7-4(a). The thickness of aluminium layer is not uniform, which is due to the fact that annealing is skipped after sputtering of Al. As shown in Figure 7-4(b), two metallic layers with a 200 nm SiC layer form a sandwich structure that is used as the IR absorber.

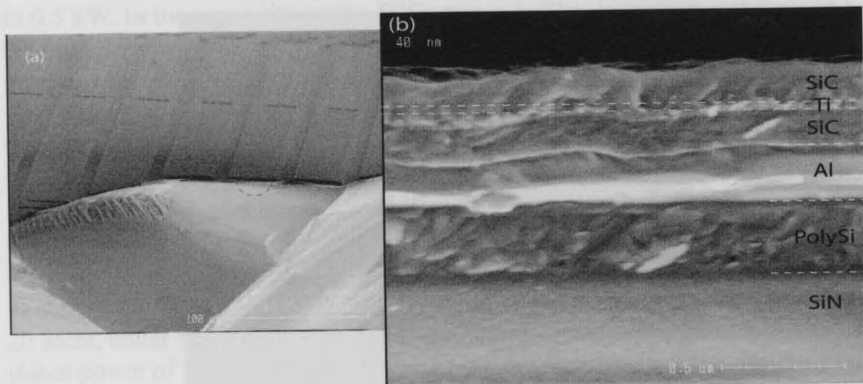


Fig. 7-4. (a) SEM of the clipped bridge with circle shown in (b) SEM detail of the cross-section before structural release of the bridge.

7.3 Sacrificial etching by 73% liquid HF

The sacrificial etching is performed to realize structures with reduced thermal diffusion in the direction normal to the plane in which the *TE* elements are integrated (i.e. vertical). The width of a bridge is $36\ \mu\text{m}$ and the two types of spacing between bridges: 4 and $10\ \mu\text{m}$. *HF* at 73% concentration was used as the etchant, because it provides a relatively slow etch rate of aluminium. The actual etch rate was determined by initial tests and was found to be 1740 nm per minute. The total etching time is set to 10 minutes and 30 seconds by considering the etching rate and the width of the bridge. After that the die is rinsed in *IPA* for several times to remove *HF*. To prepare for freeze drying, the die is immersed in Cyclohexane solution for 10 minutes. Freeze drying is executed to avoid sticking of the released structures. The yield of free-standing structures is better than 90%. Nevertheless, damage due to insufficient coverage by the protection layer, which is 200 nm *SiC*, is observed at the sidewall.

The impedance matching thin *Ti* layer was completely etched due to poor selectivity to *HF*. It is verified by testing the absorber with short etching time: 30 and 60 seconds as shown in Figure 7-5. As a result underetching is observed at

the rim of the absorber, due to the partly removal of the thin Ti layer. The IR absorption is not achieved since the impedance matching of absorber is not obtained.

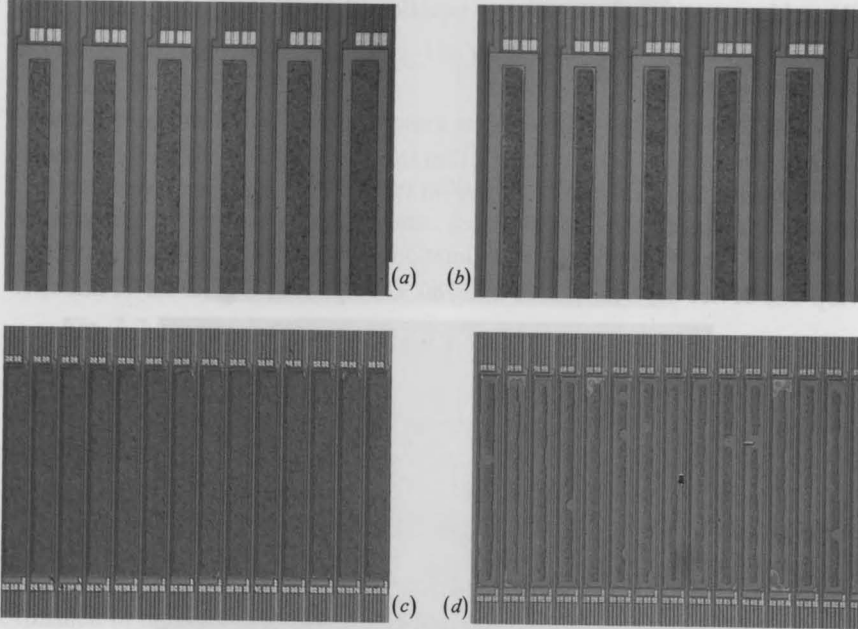
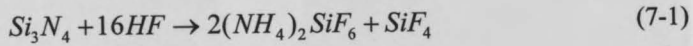


Fig. 7-5. (a) absorber with size smaller than bridge before etching (b) Ti is removed at the edge after 30 sec 73% HF. (c) absorber before etching (d) 80% of Ti is removed after 60 sec in 73% HF.

7.4 Sacrificial etching by vapour HF

Since the thin metallic layer is attached by the liquid etchant, sacrificial etching by vapor HF etching was investigated. A sample was placed above the 73% etchant with the distance of 4 cm in a closed chamber as illustrated in Figure 5-4 on page 100. The device was settled on a heater (at the backside) to evaporate the water during the reaction. It is because the condensation of water would significantly increase the etch rate of metal used at the absorbers and the electrical interconnection. The etch rate is 600 nm per minute at a temperature of

30 °C. The drawback of etching at elevated temperatures is that the etch rate of the sacrificial layer is diminished. One of advantages to use vapor *HF* is to minimize sticking during the structural etching. During the vapor *HF* etching of *SiN*, residues are created according to equation [7.1]:



The residue, $2(\text{NH}_4)_2\text{SiF}_6$, forms a non-transparent film shown in Figure 7-6 and causes an apparent increase in film thickness, which in extreme cases can lead to cracking of the structural layer on the top. More testing is required for a reproducible specification of the etch rate of *SiN* in vapor *HF*. The residue $2(\text{NH}_4)_2\text{SiF}_6$ can be removed by sublimation using a hotplate at vacuum pressure [7.2]. The device has been placed into 180 °C hotplate at 1 mBar for 40 minutes.

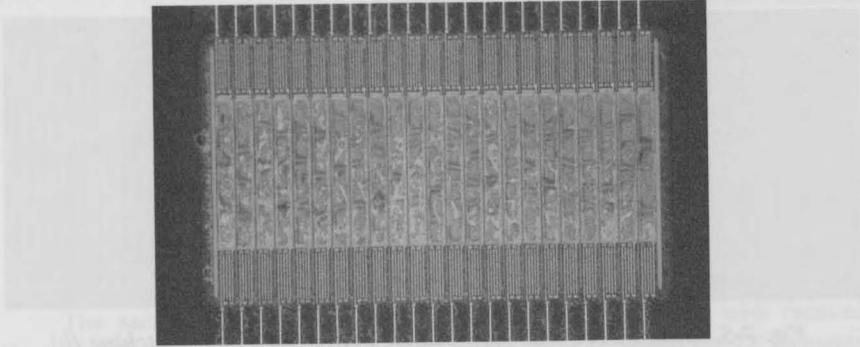


Fig. 7-6. Residue (non-transparent film) of *SiN* after etching in vapor *HF*.

The final free-standing device with the absorber after removal of the residue is shown in Figure 7-7. Although the thin film of absorber is still slightly damaged during etching, most of absorbers are intact on the bridge of *TE* elements.

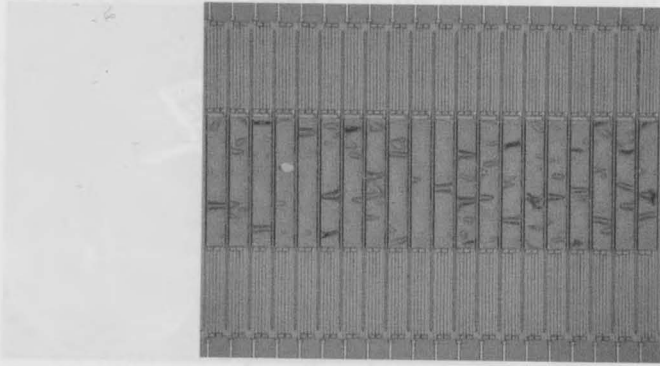


Fig. 7-7. Free-standing TE array after vapor HF.

7.5 Experimental results

The sensitivity of 36 μm wide TE elements in the array has been measured at room temperature and atmospheric pressure using an Exalos 1320 nm LED. The measurement is focus on the TE array with the first type of the absorber explained in the previous section and is deposited with SiC/Ti/SiC/Al four-layer stacks. The light is coupled into a single mode optical fiber with numerical aperture (NA) of 0.14. The spot size of IR should not be larger than the width of the TE element and is resolved by the distance between the tip of fiber and absorber, while taking into account the mode field diameter and the NA. The alignment of optical fiber and element is realized by the optical microscope as shown in Figure 7-8(a). The spot is projected onto one element and the resulting Seebeck voltage and cross-talk to a neighbouring element is measured using a HP 34420A nano-voltmeter, as shown in Figure 7-8(b).

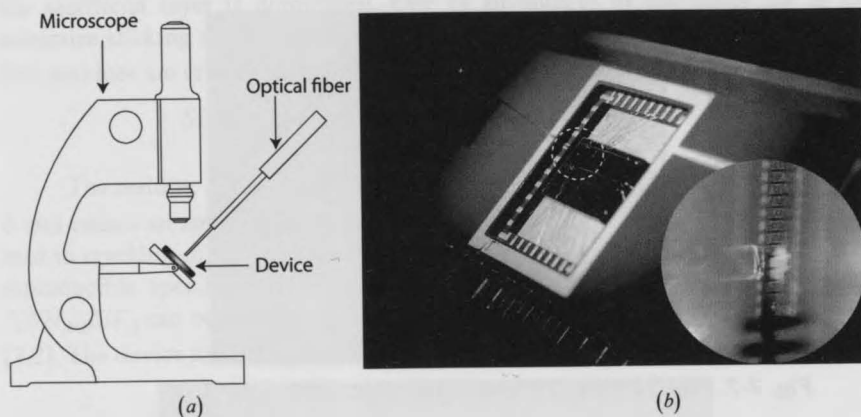


Fig. 7-8. (a) Illustration of measurement set-up. (b) Sensitivity and cross-talk measurement of TE elements with the optical fiber on illuminating the device from a 90 μm distance. The inset shows a zoom-in view.

A Thorlab Germanium photo detector has been selected as a reference to examine the output optical power of fiber. The output of TE element with absorber on the top is measured up to 627 μV . The applied optical power is 66 μW . Therefore, the sensitivity is 9.5 V/W. The sensitivity of the TE element without absorber is measured to be 3.8 V/W. The enhancement in sensitivity results as about 2.5. The sensitivity of TE element is low when operating at atmospheric pressure. This is principal from the fact that conductive heat losses causes most of the heat flux to flow from the absorber to substrate via the 4 μm air path instead of through the suspension bridge.

Five different IR LEDs (peak emission at 2.15 μm , 3 μm , 3.4 μm , 3.8 μm , 4.2 μm and 4.7 μm wavelength) and different optical power have been used as light sources. The FWHM of the LEDs is up to 490 nm. The IR-3775 thermopile reference from Xensor Integration has been used for expressing the measurement result in terms of optical power. The measurement setup also includes the Agilent 33220A function generator and a custom-made LED driving circuit, a vacuum chamber with sapphire window and lock-in amplifier SR830 for measuring optical response of the device as shown in Figure 7-9. The device is evacuated to a pressure at 1 mBar. The optical signal is chopped using the LED drive circuit to reduce sensitivity to stray light. The comparison of the sensitivity of the TE

element both with the absorber and uncoated element at the vacuum pressure operation is shown in Figure 7-10. The improved sensitivity of the TE element with absorber is considerable. Furthermore, the wavelength-dependence of the response is strongly reduced. This result is in agreement with the simulation result (Figure 7-1) of the absorber with Ti layer of 20 nm thickness.

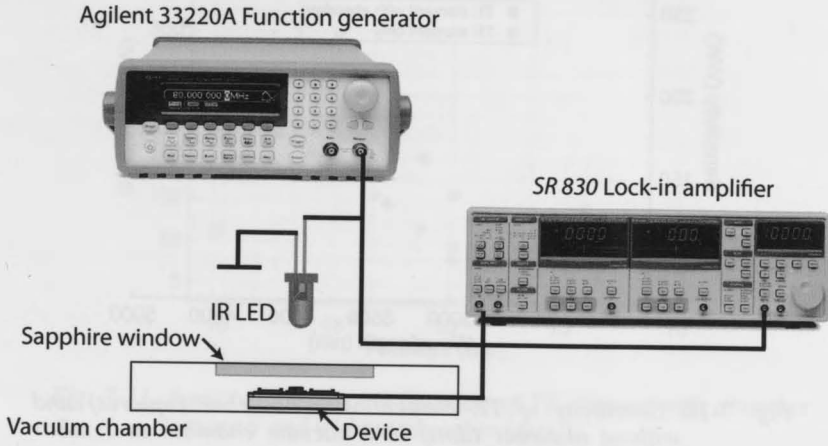


Fig. 7-9. Schematic of the measurement set-up.

The decreased thickness of Ti during vapor HF etching is probably due to pinholes in the SiC dielectric film. Ti might be oxidized to form TiO , which has a much higher etch rate in vapor HF etching [7.3]. Variations in the thickness of the thin titanium film from the fabrication tolerances and after the sacrificial process are not considered. This issue requires further research.

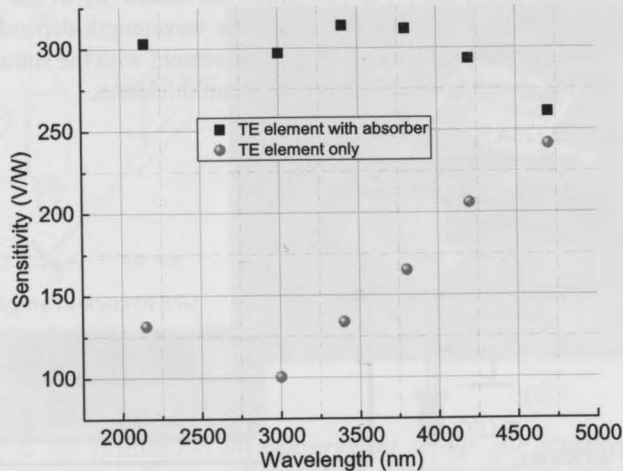


Fig. 7-10. Sensitivity of TE element with absorber (squares) and without absorber (dots) in a vacuum chamber at 1 mBar pressure in the 2-5 μm spectral range.

The high deviation between the simulation and measurement results can be explained by the following reason. Extrapolated data is being used in the simulation tool for wavelength above 1.2 μm by using simple linear fit and does not include nitride absorption at 4 μm wavelength range [7.4]. As a result, the improvement of absorption of device with SiC interference absorber is less beneficial at this wavelength. Further research is required on this topic.

Figure 7-11 indicates the improved sensitivity for a device with absorber in a low-pressure environment. The TE element with an absorber has a sensitivity of 21 V/W at ambient pressure, which is a low value, but compares favorably with the sensitivity of 7.4 V/W in air for the uncoated device (improvement by a factor of 2.8). At 1 mBar, however, the sensitivity of the TE element with absorber is 294.7 V/W, while that of the uncoated device is 129.8 V/W (a factor of 2.16). The sensitivity of the device is improved by almost a factor 20 when operated in vacuum, as compared to ambient pressure. The effect of the absorber is slightly reduced in vacuum, which is because of the increased relative effect of heat loss due to radiation.

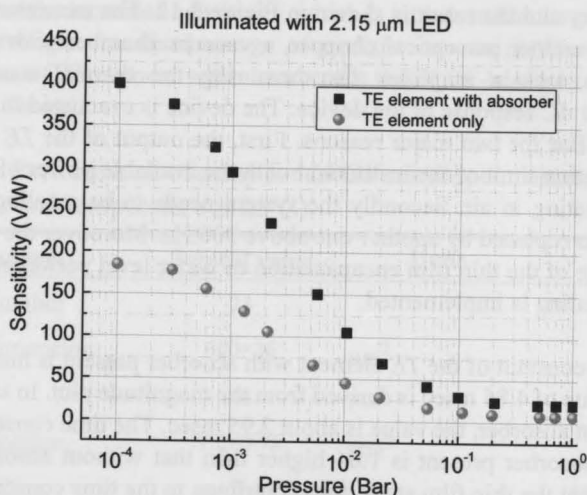


Fig. 7-11. Sensitivity versus air pressure of TE element with absorber (squares) and without absorber (dots).

The thermal cross-talk between two TE elements in an array with 10 μm wide trenches has been measured at room temperature and atmospheric pressure using the same set-up as described in the previous section. The measured cross-talk is up to 4.5% for each side and results in 9% overall cross-talk. The result is comparable to the same element pitch discussed in chapter 6, which however has a much larger vertical spacing between element and substrate due to the use of bulk-micromachining for fabrication.

The measurement result indicates that the cross-talk in the case of bulk-micromachining is one order of magnitude less than atmospheric pressure. In fact the reduction of cross-talk is from the fact that the vertical heat conduction to the substrate (spacing 4 μm) is relatively high as compared to the conduction to the neighbouring element (spacing 10 μm). This is a direct consequence of the application of surface micromachining in this work. The measured 4.5% cross-talk compares favorably to the 5.6% for the bulk-micromachined devices. Nevertheless, the reduced element-substrate spacing does reduce the sensitivity. In the case of operating in vacuum the cross-talk between elements is reduced to only 0.23% at 1 mBar (see chapter 6).

The time constant of the *TE* element has been investigated by measuring the cut-off frequency and the result is shown in Figure 7-12. The measurement setup includes an *IR* emitter, an optical chopper, a vacuum chamber with a sapphire window and a lock-in amplifier for measuring the thermal modulus plot representing the *AC* response of the device. The device is evacuated to a pressure lower than 0.1 Bar for two major reasons. First, the output of the *TE* element is below the detection limit of the instrument with the available power of *IR* emitter in case of operating in air. Secondly the system needs to be recalibrated if the chopper blade is replaced by another one above 300 Hz. Moreover the pressure is within the range of the thin film encapsulation or wafer level packaging at which the hermetic sealing is implemented.

The time constant of the *TE* element with absorber present is measured at 1 mBar and a value of 4.85 msec is derived from the magnitude plot. In case of a *TE* element without absorber, the value is about 2.95 msec. The time constant of a *TE* element with absorber present is 1.64 higher than that without absorber, which demonstrates that the thin film stack does contribute to the time constant.

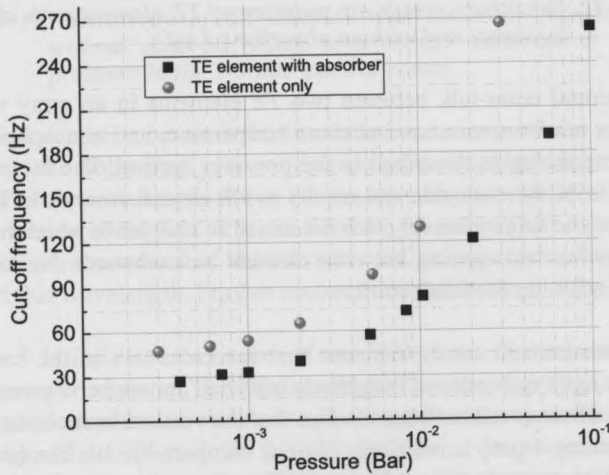


Fig. 7-12. Cut-off frequency measurement of TE elements versus pressure.

In a different set-up the time constant of device is measured at ambient pressure. The optical chopper is replaced by *LEDs* operated in a pulsed mode. The time constant with absorber present is measured to a value of 0.537 msec,

while the *TE* element only device has a time constant of 0.35 msec. The advantage of the increased sensitivity, which is introduced in the previous section, clearly outweighs the disadvantage of a slight increase in time constant. The performance of *TE* element with absorber for the *LVOF*-based microspectrometer is listed in Table 1.

TABLE 1. Performance of array for *LVOF* microspectrometer (ambient pressure and temperature at 25°C)

Parameter	Typical value	Units	Notes
Element number	23		
Element dimension	650×36	μm ²	
Pitch	46	μm	
Array dimension	1.2×0.76	mm ²	
Number of thermocouple	5		For single element
Sensitive area	282×36	μm ²	For single element
Thermopile resistance	31	kOhm	
Operating in air			
Sensitivity S_v	21	V/W	
NEP	1.078	nW	2.15 μm optical source
Specific detectivity D^*	9.346	10 ⁶ cmHz ^{1/2} W ⁻¹	source
Time constant	0.537	msec	
Operating in vacuum (1 mBar)			
Sensitivity S_v	294.7	V/W	
NEP	0.0769	nW	2.15 μm optical source
Specific detectivity D^*	131	10 ⁶ cmHz ^{1/2} W ⁻¹	
Time constant	4.85	msec	IR emitter as source

7.6 Conclusion

The fabrication and experimental validation of the *CMOS* compatible interference filter based absorbers for the thermopile detector array using surface micromachining technology are presented. The dimensions of the detector array are $1.2 \times 0.76 \text{ mm}^2$. The area of each pixel is $650 \times 36 \text{ }\mu\text{m}^2$ with a $46 \text{ }\mu\text{m}$ pitch. The presented device is intended for use in an *LVOF*-based microspectrometer. The improvement of *IR* absorption is proved by measured factor of three higher with $1.3 \text{ }\mu\text{m}$ light source. The surface micromachining is more *IC* compatible and allows for a narrower pitch, however, it limits the sensitivity of the device as well. High-performance devices are accomplished by the operation at low pressures.

The integration process includes wafer level packaging with an *LVOF* and thin film encapsulation resulting in a complete micro-spectrometer. For this reason fabrication of *TE* array with absorber should be *CMOS* compatible. *PECVD SiC* has been applied as both resonance cavity and protection layer during the sacrificial etch to release the structure. Moreover *SiC* is used as the spacing layer in the interference filter based absorber that is composed of *Ti*, *SiC* and *Al* in a sandwich structure. *SiC* is relatively resistant to *HF* attack during the etching, as compared to *SiO₂*. Nevertheless, the sidewall and pinhole issues had to be thoroughly taken into account in the design phase. The enhanced absorption, as compared to the non-coated device, and the resulting increased sensitivity of device has been demonstrated as well.

7.7 References

- [7.1] G. Vereecke, M. Schaekers, K. Verstraete, S. Arnauts, M. M. Heyns, and W. Plante, "Quantitative Analysis of Trace Metals in Silicon Nitride Films by a Vapor Phase Decomposition/Solution Collection Approach," *Journal of The Electrochemical Society*, vol. 147, pp. 1499-1501, 2000.
- [7.2] B. Du Bois, G. W. A. Vereecke, P. De Moor, C. Van Hoof, A. De Caussemaker, and A. Verbist, "HF etching of Si-oxides and Si-nitrides for surface micromachining," *Sensor Technology Conference*, pp. 131-136, 2001.

- [7.3] K. R. Williams, K. Gupta, and M. Wasilik, "Etch rates for micromachining processing-Part II," *Microelectromechanical Systems, Journal of*, vol. 12, pp. 761-778, 2003.
- [7.4] M. Modreanu, N. Tomozeiu, P. Cosmin, and M. Gartner, "Optical properties of LPCVD silicon oxynitride," *Thin Solid Films*, vol. 337, pp. 82-84, 1999.

8

Microspectrometers based on this technology offer huge potential in applications where (1) miniaturization of size or volume is paramount or (2) data pre-processing using integrated CMOS circuits is extremely beneficial. Space exploration is an example of an application in which optimization of mass or volume is essential, while scientific and medical applications (point-of-care diagnostics based on a handheld instrument with immediate results without the use of a laboratory infrastructure) are candidates for data pre-processing.

The thermal sensor plays an important role in a microspectrometer. It is shown that the performance of the thermal sensor is determined by the performance of its two essential sub-processes: the surface absorber and the thermopile element.

An excellent absorber is necessary and essential for achieving a high absorption coefficient in the spectral range of interest of a thermal sensor array. The use of metal black has been extensively applied in the commercial products due to its acceptable absorption and wide spectral range. The problems are the vulnerability and CMOS-process incompatibility. In this thesis, the use of carbon nanotubes was introduced as an alternative. It has been shown the superior

[15] K. Williams, K. Opat, and M. Waller, "Microspectrometry using surface micromachining," *Proc. SPIE*, vol. 4242, pp. 103-110, 2000.

The fabrication and experimental results of the TE detector array are presented. The device is fabricated using surface micromachining on a silicon substrate. The device is a 1.2- μm pitch array of 1.2- μm wide, 1.2- μm high pixels. The area of each pixel is $1.44 \mu\text{m}^2$ with a volume of $1.728 \mu\text{m}^3$. The presented device is intended for use in an LPOF-based microspectrometer. The improvement of IR absorption is given by measured factor of three higher with 1.3 μm light source. The surface micromachining is more IC compatible and allows for a narrower pitch, however, it limits the size of the device as well. High-performance devices are accomplished by the operation at low pressures.

The integration process includes wafer level packaging with an LPOF and thin film encapsulation resulting in a complete micro-spectrometer. For this reason fabrication of TE array with absorber should be CMOS compatible. PECVD SiC has been applied as both exposure cavity and protection layer during the sacrificial etch to release the structure. Moreover SiC is used as the spacers in the interference filter based absorber that is composed of SiC and Al in a sandwich structure. SiC is relatively resistant to HF attack during the etching, as compared to SiO₂. Nevertheless, the sidewall and platelet issues had to be thoroughly taken into account in the design phase. The enhanced absorption, as compared to the top-coated device, and the resulting increased sensitivity of device has been demonstrated as well.

7.7 References

- [7.1] G. Vereecke, M. Schackert, K. Verbeke, S. Apalich, M. M. Reyns, and W. Plante, "Quadrupole Analysis of Trace Metals in Silicon Nitride Films by a Vapor Phase Decomposition/Solution Collection Approach," *Journal of The Electrochemical Society*, vol. 147, pp. 1499-1501, 2000.
- [7.2] S. De Boel, G. W. A. Vereecke, F. De Moor, C. Van Haef, A. De Ceuninck, and A. Verbiest, "HF etching of Si-nitride and Si-dinitride for surface micromachining," *Sensory Technology Conference*, pp. 131-136, 2001.

Conclusions

8

Microspectrometers based on silicon-compatible *MEMS* technology offer huge potential in applications where: (1) optimization of mass or volume is paramount or (2) data pre-processing using integrated *CMOS* circuits is extremely beneficial. Space exploration is an example of an application in which optimization of mass or volume is essential, while consumer and medical applications (point-of-care diagnostics based on a handheld instrument with immediate results without the use of a laboratory infrastructure) are candidates for data pre-processing.

The thermal sensor plays an important role in a microspectrometer. It is shown that the performance of a thermal sensor is determined by the performance of its two essential components: the radiant absorber and the thermoelectric element.

An excellent absorber is necessary and essential for achieving a high absorption coefficient in the spectral range of interest in a thermal sensor array. The use of metal black has been extensively applied in the commercial products due to its acceptable absorption and wide spectral range. The problems are the vulnerability and *CMOS*-process incompatibility. In this thesis, the use of carbon nanotubes was introduced as an alternative. It has been shown the superior

performance as compared with the metal black type. However, some main drawbacks were related to technology constraints because of the high growth temperature (around 550 degree) of carbon nanotubes. As another alternative, absorbers based on metamaterials have been discussed. An attractive feature of these absorbers was that the absorption function and spectral-filtering can be combined. It has also been shown that the use of metamaterials in the absorbers will yield a linear relationship between the wavelength of the *IR* absorption peak and the unit-cell size. However, in that case, the small feature size of unit cells required the use of advanced lithography technology. Therefore, the interference-based (microwave) absorber was selected for our thermopile (thermoelectric) device because it adequately met the requirement of *IC*-compatibility.

The design and testing of the interference-filter-based absorbers for use in a thermopile array for an *IR* microspectrometer were discussed (chapter 3). It has been shown that even though absorbers based on SiO_2 had a better spectral response, *SiC* was still preferred because of its high resistance to *HF* etching. The experiments successfully validated the simulations, which implied that the simulation tools and our material database can be used in a subsequent phase.

The principle of the thermoelectric effect and the theoretical analysis of a single element were discussed. In an addition to that the modeling of the thermopile array for use in a miniaturized infrared microspectrometer was presented (chapter 4). Polysilicon has been selected as the thermoelectric material, despite of its moderate figure *Z*, because of its excellent *CMOS*-compatibility.

The design of the thermopile detector array is dictated by the optical properties of the dispersive element in the spectrometer. Two types of dispersive elements were proposed: a grating and an *LVOF*. The specific spatial pattern provided by the diffractive imaging grating implied that the dimensions of the sensing element depend on the position within the array. The resolving power designed was maximized at the centre element of the array. It has been shown that a spacing of 4 μm between elements theoretically limits the cross-talk of adjacent elements to 19%, whereas a gap spacing of 10 μm results in a thermal cross-talk of 10.3% when operated at atmospheric pressure. However, both cases were not acceptable in an actual device. A wider trench between elements helped to decrease cross-talk, but not efficiently. A larger element pitch in the array would only reduce the spectral selectivity. As a more efficient solution for this problem it has been proposed to operate the array in a vacuum, which consequently

contributes to the sensitivity of each thermopile element.

Several micromachining techniques were available for device fabrication (chapter 5). Removal of excess silicon under the device by bulk micromachining enabled the release of the thermoelectric detector. Since much more silicon was removed than sacrificial material in surface micromachining, the thermal insulation was superior in the bulk micromachined devices. However, the drawbacks of using bulk micromachining were the longer etching time and the stress concentration at the interface between the silicon and the device, which can lower the yield of whole process. The wafer cannot easily re-enter the clean room for further processing, for instance for deposition of a thin-film for encapsulation. Therefore, the fabrication of device based on surface micromachining was preferred. Stiction was introduced during rinse/drying, which was due to surface tension and capillary force and should be prevented by using both freeze-drying and vapour *HF* etching techniques. It has been shown that these results are presented in a high-yield process.

The thermal cross-talk in a thermopile array has been extensively studied. For experimental investigations, a test chip has been fabricated with spacing of 10 μm between the elements. For the tested array a cross-talk of about 11.2% was found. Cross-talk in the device was further reduced when placing the device in a vacuum chamber. The residual thermal cross-talk was measured at 1 mBar to be 0.8%, which corresponds well with the model (chapter 4) and was acceptable in an *IR* microspectrometer. The bandwidth at the given dimensions was at 240 Hz for the main radiated element due to its suspension and at 183 Hz for the side element due to cross-talk. This result corresponded with the simulations, which also indicate a pressure-independent cut-off frequency.

The fabrication and experimental validation of the *CMOS*-compatible interference filter-based absorbers for the thermopile detector array using surface micromachining technology were presented (chapter 7). The dimensions of the detector array are $1.2 \times 0.76 \text{ mm}^2$, with the area of each pixel being $650 \times 36 \mu\text{m}^2$ with a 46 μm pitch. The device presented was intended for the *LVOF*-based microspectrometer. Surface micromachined devices were best in terms of *IC*-compatibility and narrow pitch. However, the sensitivity of the bulk micromachined devices was slightly better. It has been shown that high-performance devices are realized by operation at low pressures.

8.1 Future work

There are highly interesting topics for further research, which are listed below.

Integration the optical system and detector array

The *CMOS* compatibility calls for the on-chip integration of *TE* elements, the detector array and readout circuitry. The hybrid integration of the optimized grating or the *LVOF* and the detector part in one package yields a fully integrated *IR* microspectrometer.

Advanced thermal cross-talk model

The measurement results do validate the model, while also revealing deviations at the higher end of the pressure range which are due to convection. In future work the effect of convection through the gap should be included in the modeling to improve the accuracy of the prediction.

Advanced packaging technology

The device shows a high performance in an evacuated environment. Therefore, the new device packaging technologies, e.g. wafer-level packaging and thin-film encapsulation, are suitable topics for the future research.

Prototype of a metamaterial microspectrometer

The microspectrometer using metamaterials only or combined with *LVOF* has the best potential to actually achieve a high-performance and low-cost optical microsystem, which should be considered in future research.

Appendix A: Thermal analytical modeling

A

A.1 Fundamentals of heat transfer

To optimize the design of the thermal sensor for use in microspectrometer application, the fundamental physics in the thermal domain should be practically applied and implemented. Heat transfer theory is used to model the performance of the detector and the limits should be well exploited. Since the thermal modeling is strongly dependent on boundary conditions, partially due to the shape of the detector, it is necessary to determine the best possible detector in terms of the geometry. This section discuss the chosen shape of the detector followed by the thermal modeling with the derived analytical solution.

A.1.1 Geometries considerations

According to literature [A.1], the geometry and materials of the thermopile detectors can be optimized dependently on the application. The different types of geometries can be practiced in the thermopile infrared sensor. Some possible structures are described: rectangular membrane, circular membrane, bridge structure, cantilever structure and hinged cantilever structure. These structures are presented in Figure A-1. The simplified model for rectangular membrane has

been reported by some assumptions [A.2][A.3][A.4]. The hinged cantilever can be analyzed as cantilever since the effect of the small support beams is negligible. The thermal signal is generated owing to the incident radiant from the optical element, for example grating. A typical characteristic of a planar imaging diffraction grating is a linear dimensional projection. As a result of the rectangular, the circular and the hinged types of the detector are not suitable in the spectrometer application since the resolving power could be limited. Therefore, the cantilever structure and bridge structure are analyzed with the corresponding models which are utilized to estimate the performance of the detectors. The analysis is focused on the cantilever and extended to bridge due to the symmetrical structure.

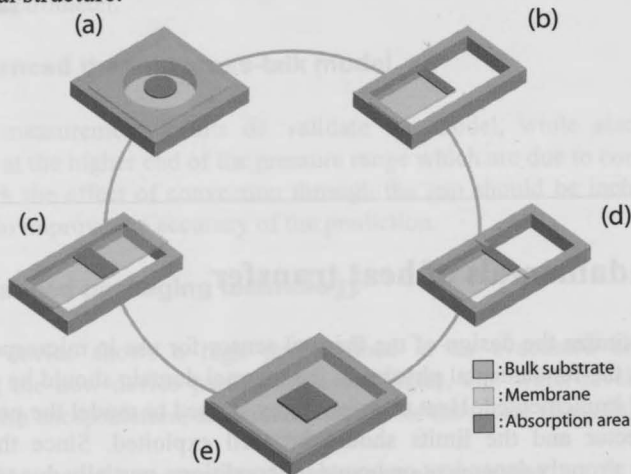


Fig. A-1. General configuration of shape of detectors. (a) circular membrane, (b) cantilever structure, (c) bridge structure, (d) hinged cantilever structure and (e) rectangular membrane.

A.1.2 Heat transfer mechanism

Three fundamental modes of heat transfer are discussed since these equations will be used in the thermal modeling.

A.1.2.1 Conduction

The law of heat conduction, also known as Fourier's law, states that the heat

flux ϕ_q is equal to the product of the thermal conductivity λ and the negative temperature gradient $-\nabla T$, as expressed by

$$\phi_q = -\lambda \nabla T \quad (\text{A-1})$$

This equation determines the heat flux for a given temperature profile and thermal conductivity. The minus sign ensures that heat flows down the temperature gradient.

A.1.2.2 Convection

Convection is the heat transfer by mass motion of a fluid (such as air or water) when the heated fluid is caused to move away from the source of heat, carrying energy with it. There are two major types of heat convection:

- Natural convection: when the fluid motion is caused by buoyancy forces that result from the density variations due to variations of temperature in the fluid.
- Forced convection: when the fluid is forced to flow over the surface by external source, creating an artificially induced convection current.

However, the natural convection from a micro-scale detector to surrounding still air is negligible, in a small package, and the heat loss is dominated by the heat conduction and the radiation [A.5].

A.1.2.3 Radiation

The thermal radiation is electromagnetic radiation emitted from a heated material. As stated in the Stefan-Boltzmann law, the total energy radiated per unit surface area of a black body in unit time is directly proportional to the fourth power of the black body's absolute temperature T . Therefore, the total radiant power from the general grey body can be written as:

$$P_{rad} = \epsilon \sigma A T^4 \quad (\text{A-2})$$

where the constant ϵ is the emissivity factor, σ is the Stefan-Boltzmann constant which equals to 5.67×10^{-8} , and A is the radiating surface area.

A.1.3 Heat Equation

The heat equation is an important partial differential equation which describes the distribution of heat (or variation in temperature) in a given region over time. For a function (x,y,z,t) of three spatial variables (x,y,z) and the time variable t , the heat equation is [A.6]:

$$\frac{\partial T}{\partial t} = \alpha \left(\frac{\partial^2 T}{\partial x^2} + \frac{\partial^2 T}{\partial y^2} + \frac{\partial^2 T}{\partial z^2} \right) + \frac{\Phi_s}{\rho c_p} \quad (\text{A-3})$$

where Φ_s the heat source power per volume V , and λ the thermal conductivity, and thermal diffusivity α which can be expressed as:

$$\alpha = \frac{\lambda}{\rho c_p} \quad (\text{A-4})$$

in which ρ is the density, and c_p is the constant pressure specific heat.

When the temperature is unchanging in time, which means the system in a steady state, the heat equation is expressed as:

$$\frac{\partial T}{\partial t} = 0 \Rightarrow \alpha \left(\frac{\partial^2 T}{\partial x^2} + \frac{\partial^2 T}{\partial y^2} + \frac{\partial^2 T}{\partial z^2} \right) + \frac{\Phi_s}{\rho c_p} = 0 \quad (\text{A-5})$$

with $\lambda \neq 0$, the heat equation is simplified as:

$$\left(\frac{\partial^2 T}{\partial x^2} + \frac{\partial^2 T}{\partial y^2} + \frac{\partial^2 T}{\partial z^2} \right) + \frac{\Phi_s}{\lambda} = 0 \quad (\text{A-6})$$

A.2 Modeling

Figure A-2 shows the top view of the sensor schematic. In order to evaluate the performance of the thermal sensor, the temperature distribution in the x -direction along the beam should be derived. Assume a uniform temperature

distribution in the y -direction and a uniform thermal conductivity of the beam.

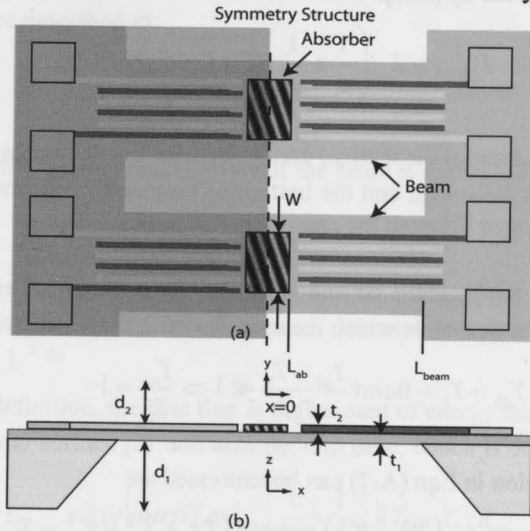


Fig. A-2. Sensor schematic of thermopile on bridge for modeling.

A.2.1 Heat loss at absorber

First of all, the heat transfer equations relevant to the absorber ($0 \leq x \leq L_{ab}$) are derived:

Heat loss P_{rad-ab} due to the radiation from the absorber is given by rewriting Eqn (A-2):

$$P_{rad-ab} = \epsilon \sigma A_{ab} (T_{ab}^4 - T_0^4) \quad (\text{A-7})$$

where A_{ab} is the radiating absorber area which expressed as $A_{ab} = W \cdot L_{ab}$, T_{ab} is the temperature of the absorber, and T_0 is the ambient temperature (cold edge).

Heat conduction P_{gas} from the absorber to the heat sink through the gas path

in z direction is given by [A.7]:

$$P_{gas-ab} = \lambda_{gas} \left(\frac{1}{d_1} + \frac{1}{d_2} \right) A_{ab} (T_{ab} - T_0) \quad (A-8)$$

where λ_{gas} denotes the thermal conductivity of the gas atmosphere, d_1 is the distance between the bridge and the bottom of heat sink as shown in Figure A-2 and d_2 is the distance between the cantilever and package cap.

Since the temperature of the absorber is moderately higher than the temperature of the heat sink, which means:

$$T_{ab} > T_0 > 0 \text{ and } \frac{T_{ab} - T_0}{T_0} \ll 1 \Rightarrow \frac{T_{ab}}{T_0} \approx 1 \quad (A-9)$$

Heat radiation in Eqn (A-7) can be expressed as:

$$\begin{aligned} P_{rad-ab} &= \varepsilon \sigma A_{ab} (T_{ab}^4 - T_0^4) = \varepsilon \sigma A (T_{ab}^2 + T_0^2) (T_{ab}^2 - T_0^2) \\ &= \varepsilon \sigma A_{ab} (T_{ab}^2 + T_0^2) (T_{ab} + T_0) (T_{ab} - T_0) \\ &= \varepsilon \sigma A_{ab} T_0^3 \left(\left(\frac{T_{ab}}{T_0} \right)^2 + 1 \right) \left(\frac{T_{ab}}{T_0} + 1 \right) (T_{ab} - T_0) \\ &\approx 4 \varepsilon \sigma A_{ab} T_0^3 (T_{ab} - T_0) \end{aligned} \quad (A-10)$$

Therefore, the heat power from the heating absorber to the beam is:

$$\begin{aligned} P_{ab} &= P_{in} - (P_{rad-ab} + P_{gas-ab}) \\ &= P_{in} - \left(4 \varepsilon \sigma T_0^3 + \lambda_{gas} \left(\frac{1}{d_1} + \frac{1}{d_2} \right) \right) (T_{ab} - T_0) A_{ab} \end{aligned} \quad (A-11)$$

First Boundary condition

The heat flux through the interface of the absorber and beam at $x = L_{ab}$ is conducted in two ways:

1. As states in the law of heat conduction, the heat flux expressed in Eqn (A-1) can be described as:

$$\phi_q = -\lambda_{eq} \frac{dT(x)}{dx} \quad (\text{A-12})$$

in which the thermal conductivity of the beam is expressed as:

$$\lambda_{eq} = \frac{\sum \lambda_s \cdot t_s}{\sum t_s} \quad (\text{A-13})$$

with film thickness t_s ($s=1,2,\dots$) and thermal conductivities of each film λ_s ($s=1,2,\dots$).

2. By the definition, the heat flux is the amount of energy that flows through a particular surface per unit area per unit time, which is described as:

$$\phi_q = \frac{P_{ab}}{A_{cross}} = \frac{P_{in} - \left(4\epsilon\sigma T_0^3 + \lambda_{gas} \left(\frac{1}{d_1} + \frac{1}{d_2} \right) \right) (T_{ab} - T_0) A_{ab}}{A_{cross}} \quad (\text{A-14})$$

in which the cross section area $A_{cross} = W(\sum t_s)$.

Combine the heat flux Eqn (A-12) and the Eqn (A-14), result in:

$$\phi_q = \frac{P_{in} - \left(4\epsilon\sigma T_0^3 + \lambda_{gas} \left(\frac{1}{d_1} + \frac{1}{d_2} \right) \right) (T_{ab} - T_0) A_{ab}}{A_{cross}} = -\lambda_{eq} \frac{dT(x)}{dx} \Big|_{x=L_{ab}} \quad (\text{A-15})$$

Rearranging the above equation to obtain the first boundary condition:

$$\frac{dT(x)}{dx} \Big|_{x=L_{ab}} = -\frac{\frac{P_{in}}{W} - \left(4\epsilon\sigma T_0^3 + \lambda_{gas} \left(\frac{1}{d_1} + \frac{1}{d_2} \right) \right) (T_{ab} - T_0) L_{ab}}{\sum \lambda_s \cdot t_s} \quad (\text{A-16})$$

A.2.2 Heat loss along beam

Loss mechanisms including radiation and gas to describe the heat equation along the beam are again specified in the Table 1:

TABLE 1. Heat loss mechanisms along beam.

Heat loss due to gas	Heat loss due to radiation
$P_{gas-beam} = \lambda_{gas} \left(\frac{1}{d_1} + \frac{1}{d_2} \right) A_{beam} (T(x) - T_0)$	$P_{rad-beam} \approx 4\epsilon\sigma A_{beam} T_0^3 (T(x) - T_0)$

where A_{beam} is the beam area and $T(x)$ is the temperature at point x on the beam $L_{ab} \leq x \leq L_{beam}$.

Rewriting the heat equation Eqn (A-6) results in:

$$\frac{\partial^2 (T(x) - T_0)}{\partial x^2} + \frac{\Phi_s}{\lambda_{eq}} = 0 \quad (A-17)$$

With the volume of beam $V = A_{beam} \cdot \sum t_s$, the power of heat source/loss of the beam per volume V is expressed by:

$$\begin{aligned} \Phi_s &= -\frac{P_{rad-beam} + P_{gas-beam}}{V} \\ &= -\frac{\left(4\epsilon\sigma T_0^3 + \lambda_{gas} \left(\frac{1}{d_1} + \frac{1}{d_2} \right) \right) A_{beam}}{A_{beam} \sum t_s} (T(x) - T_0) \end{aligned} \quad (A-18)$$

From Eqn (A-13), Eqn (A-17) and Eqn (A-18), the second-order differential equation is derived as:

$$\frac{\partial^2 (T(x) - T_0)}{\partial x^2} - \frac{\left(4\epsilon\sigma T_0^3 + \lambda_{gas} \left(\frac{1}{d_1} + \frac{1}{d_2} \right) \right)}{\sum \lambda_s \cdot t_s} (T(x) - T_0) = 0 \quad (A-19)$$

The Eqn (A-19) can be further be rewriting into:

$$\frac{\partial^2 (T(x) - T_0)}{\partial x^2} - \beta^2 (T(x) - T_0) = 0 \quad (\text{A-20})$$

where β refers to the heat transfer coefficient:

$$\beta = \left(\frac{4\varepsilon\sigma T_0^3 + \lambda_{gas} \left(\frac{1}{d_1} + \frac{1}{d_2} \right)}{\lambda_{eq} t_{eq}} \right)^{1/2} \quad (\text{A-21})$$

The general solution of the second-order differential equation Eqn (A-20) is given as:

$$T(x) - T_0 = A \cdot e^{-\beta x} + B \cdot e^{+\beta x} \quad (\text{A-22})$$

where β refers to the heat transfer coefficient.

Second Boundary condition

First, it is assumed that a uniform temperature distribution in x -direction on the beam. As shown in Figure A-2, the following boundary conditions apply:

- At hot edge:

$$T(L_{beam}) = T_0 \quad (\text{A-23})$$

- At cold edge:

$$T(L_{ab}) = T_{ab} \quad (\text{A-24})$$

Apply the Eqn (A-23) and Eqn (A-24) into Eqn (A-22) to solve A and B respectively:

$$A = \frac{(T_{ab} - T_0) \cdot e^{2\beta L_{beam}}}{e^{\beta L_{beam}} \left(e^{\beta(L_{beam} - L_{ab})} - e^{-\beta(L_{beam} - L_{ab})} \right)} \quad (\text{A-25})$$

$$B = \frac{T_{ab} - T_0}{e^{\beta L_{beam}} \left(e^{\beta(L_{beam} - L_{ab})} - e^{-\beta(L_{beam} - L_{ab})} \right)} \quad (A-26)$$

Taking A and B back into Eqn (A-22) and rearrange it; the solution of the second-order differential equation is expressed as:

$$\begin{aligned} T(x) - T_0 &= \frac{(T_{ab} - T_0) \cdot e^{2\beta L_{beam}} \cdot e^{-\beta x}}{e^{\beta L_{beam}} \left(e^{\beta(L_{beam} - L_{ab})} - e^{-\beta(L_{beam} - L_{ab})} \right)} - \frac{(T_{ab} - T_0) \cdot e^{\beta x}}{e^{\beta L_{beam}} \left(e^{\beta(L_{beam} - L_{ab})} - e^{-\beta(L_{beam} - L_{ab})} \right)} \\ &= \frac{e^{\beta L_{beam}} \left(e^{\beta(L_{beam} - L_{ab})} - e^{-\beta(L_{beam} - L_{ab})} \right)}{e^{\beta L_{beam}} \left(e^{\beta(L_{beam} - L_{ab})} - e^{-\beta(L_{beam} - L_{ab})} \right)} (T_{ab} - T_0) \\ &= \frac{\sinh(\beta \cdot (L_{beam} - x))}{\sinh(\beta \cdot (L_{beam} - L_{ab}))} (T_{ab} - T_0) \end{aligned} \quad (A-27)$$

A.2.3 Temperature distribution along beam

To get the unknown T_{ab} , the complete analytical solution can be derived with the first boundary condition via Eqn (A-16) which is first rewritten by applying Eqn (A-21):

$$\left. \frac{dT(x)}{dx} \right|_{x=L_{ab}} = - \frac{\frac{P_{in}}{W} - \beta^2 \left(\sum \lambda_s \cdot t_s \right) (T_{ab} - T_0) L_{ab}}{\sum \lambda_s \cdot t_s} \quad (A-28)$$

Eqn (A-27) is differentiated to match the above equation and shown as:

$$\begin{aligned} \frac{dT(x)}{dx} &= \frac{d \left(\frac{\sinh(\beta \cdot (L_{beam} - x))}{\sinh(\beta \cdot (L_{beam} - L_{ab}))} \right)}{dx} (T_{ab} - T_0) \\ &= \frac{-\beta \cosh(\beta \cdot (L_{beam} - x))}{\sinh(\beta \cdot (L_{beam} - L_{ab}))} (T_{ab} - T_0) \end{aligned} \quad (A-29)$$

Combine the Eqn (A-28) and Eqn (A-29), T_{ab} is expressed as:

$$\frac{\beta \cosh(\beta \cdot (L_{beam} - x))}{\sinh(\beta \cdot (L_{beam} - L_{ab}))} (T_{ab} - T_0) = \frac{\frac{P_{in}}{W} - \beta^2 (\sum \lambda_s \cdot t_s) (T_{ab} - T_0) L_{ab}}{\sum \lambda_s \cdot t_s} \quad (A-30)$$

$$\Rightarrow T_{ab} = \frac{\frac{P_{in}}{\beta \cdot W (\sum \lambda_s \cdot t_s)}}{\beta \cdot L_{beam} + \coth(\beta \cdot (L_{beam} - L_{ab}))} + T_0$$

Taking Eqn (A-30) into Eqn (A-27), the final analytical solution for the temperature distribution in x -direction on the beam is expressed as:

$$T(x) = \left(\frac{\frac{P_{in}}{\beta \cdot W (\sum \lambda_s \cdot t_s)}}{\beta \cdot L_{beam} + \coth(\beta \cdot (L_{beam} - L_{ab}))} \right) \frac{\sinh(\beta \cdot (L_{beam} - x))}{\sinh(\beta \cdot (L_{beam} - L_{ab}))} + T_0 \quad (A-31)$$

When $x = L_{ab}$ (temperature at the interface of the absorber and the beam), the above equation can be simplified into:

$$T(x=L_{ab}) = \frac{P_{in}}{\left(4\epsilon\sigma T_0^3 + \lambda_{gas} \left(\frac{1}{d_1} + \frac{1}{d_2} \right) \right) L_{ab} W + W (\sum \lambda_s t_s) \beta \coth(\beta L_{beam})} + T_0 \quad (A-32)$$

A.3 References

- [A.1] F. Völklein and H. Baltes, "Optimization tool for the performance parameters of thermoelectric microsensors," *Sensors and Actuators A: Physical*, vol. 36, pp. 65-71, 1993.
- [A.2] A. G. Kozlov, "Optimization of thin-film thermoelectric radiation sensor with separate disposition of absorbing layer and comb thermoelectric transducer," *Sensors and Actuators A: Physical*, vol. 84, pp. 259-269, 2000.

- [A.3] C. Escriba, E. Campo, D. Estève, and J. Y. Fourniols, "Complete analytical modeling and analysis of micromachined thermoelectric uncooled IR sensors," *Sensors and Actuators A: Physical*, vol. 120, pp. 267-276, 2005.
- [A.4] D. Randjelovic, A. Petropoulos, G. Kaltsas, M. Stojanovic, Z. Lazic, Z. Djuric, and M. Matic, "Multipurpose MEMS thermal sensor based on thermopiles," *Sensors and Actuators A: Physical*, vol. 141, pp. 404-413, 2008.
- [A.5] X. J. Hu, A. Jain, and K. E. Goodson, "Investigation of the natural convection boundary condition in microfabricated structures," *International Journal of Thermal Sciences*, vol. 47, pp. 820-824, 2008.
- [A.6] D. M. Rowe, *Handbook of Thermoelectrics*. Boca Raton., USA: CRC Press, 1994.
- [A.7] T. Elbel, S. Poser, and H. Fischer, "Thermoelectric radiation microsensors," *Sensors and Actuators A: Physical*, vol. 42, pp. 493-496, 1994.

Abbreviations and Acronyms

The following abbreviations and acronyms are used in this thesis:

AC	Alternating current
Al	Aluminium
CMOS	Complementary metal oxide semiconductor
CNT	Carbon nanotube
CVD	Chemical vapour deposition
DC	Direct current
DIMES	Delft institute of microsystems and nanoelectronics
FEM	Finite element method
FTIR	Fourier transform infrared spectrometer
FWHM	Full width at half maximum
HF	Hydrogen fluoride
IC	Integrated circuit
IR	Infrared
IPA	Isopropyl alcohol
KOH	Potassium hydroxide

Abbreviations and Acronyms

LED	Light emitting diode
LPCVD	Low pressure chemical vapour deposition
LVOF	Linear variable optical filter
MEMS	Microelectromechanical systems
MIR	Mid infrared
NA	Numerical aperture
NDIR	Non-dispersive infrared sensor
PECVD	Plasma enhanced chemical vapour deposition
PolySi	polysilicon
RIE	Reactive ion etching
SEM	Scanning electron microscope
SiC	Silicon carbide
SiN	Silicon nitride
SiO ₂	Silicon dioxide
SNR	Signal to noise ratio
TCR	Temperature coefficient resistance
TE	Thermoelectric
TEOS	Tetraethyl orthosilicate
Ti	Titanium

Summary

This thesis discusses research on a thermo-electric detector array, the thermo-electric elements of which are coated with a custom-designed absorber. The research is partly driven by the challenges of miniaturizing an optical system using *MEMS* technology, but it is also application-driven, since the optical microspectrometer has huge potential for implementation in applications that cannot be served with expensive, bulky conventional spectroscopic instruments. The emphasis of this thesis is on the design and *CMOS*-compatible fabrication of an array of thermopiles coated with an optical absorber for use in mid-infrared (mid-*IR*) microspectrometers. The measured specifications are listed in a table on page 129.

Applications

The major applications of the spectrometer are in chemical analyses of gas and liquids. In spectroscopy the absorption, emission, or scattering of electromagnetic radiation by materials is measured to study atoms or molecules, or to observe physical processes. *IR* absorption spectroscopy is the most frequently used technique in the industry. The thermal detector is the key component in such an instrument.

Microspectrometer systems

The general configuration of a microspectrometer is comprised of a light source, a dispersion element and a detector. The light source supplies a continuous optical output or a pulsed signal, which facilitates an enhanced *SNR*.

The dispersion element is used to split up the broadband light signal into several narrow spectral bands. In general, two approaches can be used for dispersion: wavelength selection and wavelength encoding. The optical signals that result from the dispersion are converted into the electrical signals for further processing.

The available dispersion techniques can be classified into several categories based on the operating principles: refraction, interference, diffraction, and application of the newly developed metamaterials. Microspectrometers can be fabricated with a dispersion function implemented using grating, which is based on diffraction. Alternatively, a linear variable optical filter (*LVOF*) based on the interference (Fabry-Perot) principle can be used to realize the dispersive element.

The detectors can be classified into two groups based on their operating principle: photon detectors and thermal detectors. The photon detectors combine a good signal-to-noise performance and a very fast response. However, photon detectors have a wavelength-dependent response and generally need to be cooled at the mid-*IR* wavelength range. The thermal detector is selected and fabricated in this thesis despite the less favourable detection limit because of the advantages of un-cooled operation, and the flat and broadband responses.

Thermal detector

Operation of the thermal detector is comprised of two conversion steps: (a) radiant (optical)-to-thermal and (b) thermo-to-electrical. The absorber is an essential component in the optical-thermal conversion. Two new types of absorbers are introduced, both of which are based on carbon nanotubes and use metamaterials. The interference-based (microwave) absorber is also used for the thermopile-based detectors described in this thesis, because of the *IC*-compatibility of the fabrication in the post-process.

Thermopiles are used for the conversion from the thermal to the electrical domain. Various thermoelectric materials are discussed in this thesis and polysilicon is selected as the material used, because of its acceptable Seebeck coefficient and compatibility with the *CMOS* process.

Design of the system

The basic *TE* element is analyzed and the results are used in the design of an optimum *TE* element (pixel) to satisfy the application requirements. This

approach is extended to the optimum design of elements in an array. The array is intended for use in either the grating-based or the *LVOF*-based microspectrometer. Analytical and numerical modeling was applied in the design of the grating for a microspectrometer which was intended for the 1.5-3 μm wavelength range. The resolving power, R , is greatest at the centre element of the array ($R=68$) and the calculated sensitivity $S = 289 \text{ VW}^{-1}$, in the case of fabrication using bulk micromachining and assuming a perfect absorber. A spacing of 4 μm between elements limits the cross-talk of adjacent elements to 19% theoretically, whereas a gap spacing of 10 μm results in a thermal cross-talk of 10.3% when operated at atmospheric pressure.

Technology

The micromachining techniques applied during the fabrication of the thermoelectric detector in the *IR* microspectrometer are bulk and surface micromachining. Since the final goal is to combine a micro-scale physics sensor and the readout realized in a *CMOS* process, the emphasis is on the fabrication compatibility. Generally the planar wafer is processed into three-dimensional structures by micromachining technologies subsequent to the *IC* fabrication. An essential aspect of the detector is the removal of silicon under the device. One approach is to use bulk micromachining, which results in a relatively large gap and consequently in better thermal insulation as compared to a thermopile that is fabricated based on surface micromachining. Nevertheless, thermopiles based on surface micromachining are the most promising because of the superior *CMOS* compatibility and potential for further processing, for instance in the deposition of a thin film for encapsulation.

New concepts, original contributions and their results

The original work presented in this thesis is:

- Fabrication of a detector array with an absorber based on an interference-filter on the thermopiles.
- Design of a microspectrometer based on an *LVOF* as the optical dispersion element, and a metamaterial as the spectral selective absorber, which eliminates the need for the bandpass filter that is typically mounted on the top of the housing to limit the operating band.

- The properties of carbon nanotubes are explored for use as an absorber. The performance is superior to that of the conventional metal-black absorber.
- Detector arrays are designed and optimized for use in combination with different dispersion components (imaging grating and *LVOF*).
- The physical performance limits of the thermopile detector array are explored and the sensitivity and cross-talk between elements (pixels) is specified, including the dependence on air pressure.

Outlook

The overview presented in chapter 2 shows that very few mid-IR microspectrometers are available and also shows the added value of an integrated microsystem in many applications. Technology research and product development in this field, therefore, seem to be very relevant. *IC*-compatible *MEMS* technology is the key to obtaining a microsystem with a small size and weight, without significantly reducing the optical performance and the potential for integrating the signal pre-processing that is needed to serve those applications.

The techniques for fabrication of optical absorbers, which are presented in this thesis for use in a microspectrometer, can be used to enhance the performance of many different optical components or systems, such as solar collectors.

Samenvatting

In dit proefschrift wordt onderzoek naar een array van thermo-elektrische detectoren, welke zijn voorzien van een speciaal ontworpen toplaag, beschreven. Dit onderzoek wordt deels gestuurd door de uitdagingen van de miniaturisatie van een optisch systeem op basis van *MEMS* technologie, maar wordt ook gestuurd door de toepassingen, aangezien de optische microspectrometer een groot potentieel biedt voor gebruik in toepassingen welke niet bedient kunnen worden door de gebruikelijke grote en dure spectroscopische instrumenten. De nadruk ligt in dit proefschrift op het ontwerp en de *CMOS*-compatibele fabricage van een array van thermozuilen, welke zijn voorzien van een optisch absorberende toplaag, voor toepassing in een microspectrometer, welke werkzaam is in het mid-infrarood (*mid-IR*). De gemeten specificaties van de detector array zijn opgelijst in een tabel op blz. 129.

Toepassingen

Het belangrijkste toepassingen van de spectrometer zijn in de chemische analyse van gassen en vloeistoffen. In de spectroscopie wordt de absorptie, emissie of verstrooiing van elektro-magnetische straling door materialen gemeten ten behoeve van de studie aan atomen of moleculen, of voor de waarneming van fysische processen. *IR* absorptie spectroscopie is de meest gebruikte techniek in industrie. De thermische detector is de bepalende component in zo'n instrument.

Microspectrometersystemen

In de algemene opzet is een microspectrometer is samengesteld uit een

lichtbron, een dispersief element en een detector. De lichtbron kan zodanig worden aangestuurd dat een continu optisch uitgangssignaal ontstaat of een pulserend signaal, welke een verbeterde Signaal-Ruis gedrag mogelijk maakt. Het dispersieve element wordt gebruikt om het breedbandige optische ingangssignaal op te splitsen in verschillende smalle spectrale banden. In het algemeen kunnen twee verschillende methoden worden gebruikt voor dispersie: golflengteselectie en golflengtecodering. De optische signalen na dispersie worden omgezet in elektrische signalen voor verdere verwerking.

De beschikbare technieken voor dispersie kunnen worden ingedeeld in verschillende klassen, gebaseerd op het werkprincipe: refractie, interferentie, diffractie en de toepassing van de recentelijk ontworpen metamaterialen. Microspectrometers kunnen worden gefabriceerd met de dispersiefunctie ingevuld door een tralie, waarvan de werking is gebaseerd op diffractie. Een lineair variabel optisch filter (*LVOF*) gebaseerd op interferentie (Fabry-Perot) kan worden gebruikt als alternatief voor de realisatie van het dispersieve element.

De detectoren kunnen worden ingedeeld in twee groepen op basis van het werkprincipe: foton detectoren en thermische detectoren. Fotondetectoren combineren een goed signaal-ruis gedrag met een zeer snelle responsie. Echter, fotondetectoren vertonen een golflengte-afhankelijke responsie en moeten in het algemeen worden gekoeld bij gebruik in het mid-*IR* golflengtegebied. De thermische detector is in dit proefschrift gekozen en gefabriceerd, ondanks de mindere detectiegrens, vanwege de voordelen van ongekoeld bedrijf en een vlakke en breedbandige responsie.

Thermische detectoren

De werking van de thermische detector omvat de omzetting in twee stappen: (a) straling (optisch) naar thermisch en (b) thermisch naar elektrisch. De absorber is een essentiële component in de opto-thermische omzetting. Twee nieuwe typen van absorbers zijn geïntroduceerd: gebaseerd op koolstof nanobuisjes en gebruik van metamaterialen. De absorber gebaseerd op interferentie (microgolf) wordt ook gebruikt in de thermoziil gebaseerde detectoren welke worden beschreven in dit proefschrift, vanwege de *IC*-compatibiliteit van de fabricage in een 'post-process'.

Thermoziilen worden gebruikt voor de omzetting vanuit het thermische naar het elektrische domein. Verschillende materialen worden in dit proefschrift

beschreven en gekozen is voor polysilicium als het toe te passen materiaal, vanwege de acceptabele Seebeck coëfficiënt en de compatibiliteit met een *CMOS* proces.

Ontwerp van het systeem

Het elementaire *TE* element is onderzocht en de resultaten worden gebruikt voor het ontwerp van een *TE* element (pixel), welke optimaal voldoet aan de eisen van de toepassing. Deze aanpak wordt voortgezet in het optimale ontwerp van een array. Het array is bedoeld voor gebruik in de tralie-gebaseerde of de *LVOF*-gebaseerde microspectrometer. Analytische en numerieke modellering werd toegepast bij het ontwerp van de tralie voor gebruik in een microspectrometer, welke was bedoeld voor het golflengtegebied tussen 1.5 en 3 μm . Het oplossend vermogen, R , is maximaal bij het middelste element in het array ($R=68$) en de berekende gevoeligheid $S = 289 \text{ VW}^{-1}$, in geval van fabricage op basis van 'bulk micromachining' en indien een perfecte absorber wordt verondersteld. Een afstand van 4 μm tussen de elementen beperkt de overspraak tussen naburige kanalen in theorie tot 19%, terwijl bij een afstand van 10 μm een thermische overspraak van 10.3% volgt, indien bedreven bij atmosferische druk.

Technologie

De microfabricagetechnieken welke zijn toegepast voor de fabricage van de thermo-elektrische detector in de *IR* microspectrometer zijn: 'bulk' and 'surface micromachining'. Aangezien de combinatie van de micro sensor en de uitlezing in een *CMOS* proces het uiteindelijke doel is, ligt de nadruk op de fabricagecompatibiliteit. In het algemeen worden drie-dimensionele structuren in een planaire wafer gerealiseerd door middel van 'micromachining' technieken, welke volgen op de *IC* fabricage. Een essentieel aspect van de detector is de verwijdering van silicium onder de thermozuil. Eén benadering is gebaseerd op het gebruik van 'bulk micromachining', waarbij een relatief groot gat ontstaat en dus een betere thermische isolatie in vergelijking tot een thermozuil gefabriceerd door 'surface micromachining'. Desondanks zijn thermozuilen op basis van 'surface micromachining' het meest veelbelovend, vanwege de superieure *CMOS* compatibiliteit en de mogelijkheden voor vervolgstappen in de fabricage, bij voorbeeld aanbrengen van een dunne film voor inkapselen.

Nieuwe concepten, originele contributies and de resultaten

Het originele werk gepresenteerd in dit proefschrift is:

- Fabricage van een array van detectoren, waarbij de thermozuilen zijn voorzien van een absorber gebaseerd op interferentie-filter.
- Ontwerp van een microspectrometer gebaseerd op een *LVOF* als het optisch dispersief element en een metamateriaal als de spectraal selectieve absorber, waardoor het band-doorlatende filter dat normaliter bovenop de behuizing wordt geplaatst om het werkgebied in te perken, overbodig wordt.
- De eigenschappen van koolstof nanobuisjes voor gebruik als een absorber zijn onderzocht. De prestaties blijken superieur aan die van de conventionele 'metal-black' absorber.
- Detector arrays zijn ontworpen en geoptimaliseerd voor gebruik in combinatie met verschillende dispersieve componenten (beeldvormende tralie en *LVOF*).
- The fysieke limieten van de prestaties van een detector gebaseerd op een array van thermozuilen zijn onderzocht en de gevoeligheid en overspraak tussen elementen (pixels) was gespecificeerd, inclusief de luchtdrukgevoeligheid.

Vooruitzicht

Het overzicht gepresenteerd in hoofdstuk 2 toont aan dat zeer weinig mid-IR microspectrometers beschikbaar zijn en toont ook aan dat een geïntegreerd microsysteem meerwaarde kan bieden in veel toepassingen. Technologisch onderzoek en product ontwikkeling in dit gebied lijken daarom zeer relevant. *IC*-compatible *MEMS* technologie is de sleutel tot het verkrijgen van een microsysteem met de benodigde kleine afmetingen en gewicht, zonder dat de optische prestaties significant behoeven te worden verlaagd. Het potentieel van silicium *MEMS* technologie voor de integratie van voorverwerking van signalen biedt groot potentieel in de genoemde toepassingen.

De technieken voor fabricage van optische absorbers, welke is gepresenteerd in dit proefschrift voor toepassing in een microspectrometer, kunnen worden toegepast voor de verbetering van de prestaties van andere optische componenten of systemen, zoals zonnecellen.

Acknowledgements

This thesis has partly been supported by the Dutch technology Foundation (STW) under grant number DET.6667 and by the TNO & ESA ITI-phase 1 project. Their support is gratefully acknowledged.

First of all I would like to thank my supervisor, Dr. Reinoud Wollffenbuttel, who offered me so much advice, patiently supervising, and always proper guidance. I also want to thank him for involving me in teaching. I have learned a lot from him, without his help I could not have finished my dissertation successfully in time.

I would like to thank Prof. Gerard Meijer, my promoter, to whom I am very thankful for his valuable comments and inspired discussion on my thesis. I do hope to have another opportunity to jog with him.

Heartily thank the advice of the committee members, Prof. G.M.H. Minas, Prof. P. Enoksson, Prof. B. Dam, Prof. P.P.L. Regtien, Dr. Ger de Graaf, for their significant comments, which enabled me to make the necessary improvements.

Thank Prof. Paddy French for the friendly and warm research environment and kindly representing me in the APCOT 2010 conference during my disability.

There is also one person I must offer my heartfelt thanks, Prof. Lina Sarro, who genially shared the experience on the process of fabrication. I am really appreciated for her generous and timely help.

Acknowledgements

I would like to thank Johan Leijters, who brought me into the world of sun sensor. I learned a great deal from them.

My sincere thanks go to group members to Arvin Emadi for helping me a lot especially while I was on crutches; to Semen Grabarnik for helping the optical simulations; to Sebastiaan Voorderhake for assisting on the encapsulated device; to Shuoxi Chen for characterizing the gas sensor; to Chi Liu for measuring the diodes. I have enjoyed substantial discussions with them.

Thank all my colleagues in the Electronic Instrumentation Laboratory, and especially to Joyce Siemers, Adri Roos-Rouffaer, Jawad Jodeh, Willem van der Sluys, and Ilse van der Kraaij for all their administration and financial support. I would like to thank Zu-yao Chang, Piet Trimp, Jeroen Bastemeijer, Jeff Mollinger, Antoon Frehe, and Maureen Meekel for their help with technical, instrumental and IT problems. Many thanks give to my fellows Sharma, Yue (also thanks for the ride), Bere, Chungkai, Lukasz, Rosana, Kamran, Vijay, Ning, Xia, Rong, Darko, Youngcheol, Lei, Agung, Mukul, Mina, Zili, Deva, Ruimin, Hamed, Qinwen, Yang, Jiaming, Saleh, Ali, Caspar, Zhichao, Mahdi, Gayathri, Nishant, Eduardo, Max, Bou, Karfee Frank, and Mohammad for the delightful time and pleasant chat.

Micromachining is always a major issue for IR detector fabrication, so I would like to thank everybody who helped with processing, technical support and instructions: Dr. Fredrik Creemer, Dr. Gregory Pandraud, Dr. Henk van Zeijl, Dr. Johannes van Wingerden, Charles de Boer, Alex van den Bogaard, Jan Groeneweg, Koos van Hartingsveldt, Ruud Klerks, Mario Laros, Silvana Milosavljevic, Tom Scholtes, Loek Steenweg, Petet Swart, Cassan Visser, Wim Wien, Jan Cornelis Wolff, Michiel van der Zwan, Robert Verhoeven and Joost Berendse. Especially thank Wim van der Vlist for his careful help with the device fabrication. Also I have enjoyed beneficial discussions and experiments on my work with several friends and colleagues. Therefore, I would like to thank Fabio Santagata, Sten Vollebregt, Thomas Moh, Solomon Agbo and Olindo Isabella.

I would like to thank all my family and friends in the Netherlands, Taiwan and Facebook for the nice moments we spend together.

I have been fortunate enough to learn from personal experience that seriously damaging the same foot twice during a four-year Ph.D. study only gives a temporarily physical disability each time and does not affect the operation of the

List of Publications

brain.

I am very grateful for my mother. Her support and love encouraged me to study abroad.

Last but not least, I thank my beloved wife, Ifan, who has always supported me and shared with me for better or worse.

In Scientific Journals

H. Wu, A. Enadi, P. M. Sarin, G. de Graaf, and R. F. Wölfel, "A surface micromachined thermopile detector array with an interference-based absorber," *Journal of Micromechanics and Microengineering*, vol. 21, p. 074005, 2011.

H. Wu, S. Grabenik, A. Enadi, G. de Graaf, and R. F. Wölfel, "Characterization of thermal cross-link in a MEMS-based thermopile detector array," *Journal of Micromechanics and Microengineering*, vol. 18, p. 074022, 2009.

H. Wu, S. Grabenik, A. Enadi, G. de Graaf, and R. F. Wölfel, "A thermopile detector array with scaled TE element for use in an integrated IR microspectrometer," *Journal of Micromechanics and Microengineering*, vol. 18, p. 064017, 2008.

A. Enadi, H. Wu, S. Grabenik, G. de Graaf, K. Helber, P. Eriksson, J. H. Correia, and R. F. Wölfel, "Fabrication and characterization of Bi₂Te Compatible Linear Variable Optical Filter with application in a microspectrometer," *Sensors and Actuators A: Physical*, vol. 162, pp. 400-405, 2010.

A. Enadi, H. Wu, S. Grabenik, G. de Graaf, and R. F. Wölfel, "Vertically tapered layers for optical applications fabricated using resist reflow," *Journal of Micromechanics and Microengineering*, vol. 19, p. 074014, 2009.

S. Grabenik, A. Enadi, H. Wu, G. de Graaf, and R. F. Wölfel, "High-resolution microspectrometer with an aberration-correcting planar grating," *Appl. Opt.*, vol. 47, pp. 6442-6447, 2008.

S. Grabenik, A. Enadi, H. Wu, G. de Graaf, G. Vdovin, and R. F.

Acknowledgements

I would like to thank John Leffers, who brought me into the world of IR detector. I learned a great deal from them.

My sincere thanks go to group members in Arvin Fung for helping them let especially while I was on crutches; to Simon Oubacht for helping the optical fabrication; to Sheng Chen for characterizing the various micro-fabricated detectors. I have enjoyed substantial discussions with them.

Thank all my colleagues in the Electronic Instrumentation Laboratory, and especially to Joyce Siemers, Adri Rous-Rodffier, Jowad Jodoh, Willem van der Sloys, and Ilsa van der Kraaij for all their administration and financial support. I would like to thank Zheyao Cheng, Piet Tripp, Jeroen Bontenberger, Jeff Mollinger, Anton Preha, and Maureen Mackel for their help with technical, instrumental and IT problems. Many thanks go to my fellow students, Yoe (also thanks for the ride), Bert, Chongxi, Lukasz, Roman, Karim, Vijay, Ning, Xia, Rong, Derks, Youngsook, Lei, Agung, Mikul, Mina, Zili, Deva, Raiman, Hamed, Qirwen, Yang, Jianing, Saleh, Ali, Caspar, Zhibao, Mahal, Gayatri, Nishant, Eduardo, Max, Bou, Karibe Frank, and Mohammad for the delightful time and pleasant chat.

Micromachining is always a major issue for IR detector fabrication, so I would like to thank everybody who helped with processing, technical support and instructions: Dr. Fredrik Groener, Dr. Gregory Papadour, Dr. Henk van Zoij, Dr. Johannes van Wingerden, Charles de Boer, Alex van den Bogert, Jan Groeneweg, Kees van Haringveldt, Roud Klerk, Mario Lavin, Silvana Milosavljevic, Tom Scholtes, Lock Stenweg, Peter Swart, Cees van Viper, Wim Wien, Jan Cornelis Wolff, Michiel van der Zwan, Robert Verhoeven and Joost Berrisbe. Especially thank Wim van der Vlist for his careful help with the device fabrication. Also I have enjoyed beneficial discussions and experiments on my work with several friends and colleagues. Therefore, I would like to thank Fabio Santagata, Sten Velleberg, Thomas Moh, Solomon Agbo and Oluwole Isabella.

I would like to thank all my family and friends in the Netherlands, Taiwan and Facebook for the nice moments we spend together.

I have been fortunate enough to learn from personal experience that seriously damaging the same foot twice during a four-year Ph.D. study only gives a temporarily physical disability each time and does not affect the operation of the

List of Publications

In Scientific Journals

H. Wu, A. Emadi, P. M. Sarro, G. de Graaf, and R. F. Wolffenbuttel, "A surface micromachined thermopile detector array with an interference-based absorber," *Journal of Micromechanics and Microengineering*, vol. 21, p. 074009, 2011.

H. Wu, S. Grabarnik, A. Emadi, G. de Graaf, and R. F. Wolffenbuttel, "Characterization of thermal cross-talk in a MEMS-based thermopile detector array," *Journal of Micromechanics and Microengineering*, vol. 19, p. 074022, 2009.

H. Wu, S. Grabarnik, A. Emadi, G. de Graaf, and R. F. Wolffenbuttel, "A thermopile detector array with scaled TE elements for use in an integrated IR microspectrometer," *Journal of Micromechanics and Microengineering*, vol. 18, p. 064017, 2008.

A. Emadi, H. Wu, S. Grabarnik, G. de Graaf, K. Hedsten, P. Enoksson, J. H. Correia, and R. F. Wolffenbuttel, "Fabrication and characterization of IC-Compatible Linear Variable Optical Filters with application in a microspectrometer," *Sensors and Actuators A: Physical*, vol. 162, pp. 400-405, 2010.

A. Emadi, H. Wu, S. Grabarnik, G. de Graaf, and R. F. Wolffenbuttel, "Vertically tapered layers for optical applications fabricated using resist reflow," *Journal of Micromechanics and Microengineering*, vol. 19, p. 074014, 2009.

S. Grabarnik, A. Emadi, H. Wu, G. de Graaf, and R. F. Wolffenbuttel, "High-resolution microspectrometer with an aberration-correcting planar grating," *Appl. Opt.*, vol. 47, pp. 6442-6447, 2008.

S. Grabarnik, A. Emadi, H. Wu, G. de Graaf, G. Vdovin, and R. F.

List of Publications

Wolffenbittel, "Fabrication of an imaging diffraction grating for use in a MEMS-based optical microspectrograph," *Journal of Micromechanics and Microengineering*, vol. 18, p. 064006, 2008.

In conference proceedings

2011

H. Wu, S. Vollebregt, A. Emadi, G. de Graaf, R. Ishihara, and R. F. Wolffenbittel, "Design and Fabrication of an Albedo Insensitive Analog Sun Sensor," in *Euroensors XXV conference*, Athens, Greece, 2011.

H. Wu, A. Emadi, G. de Graaf, J. Leijtens, and R. F. Wolffenbittel, "Design and Fabrication of an Albedo Insensitive Analog Sun Sensor," in *Euroensors XXV conference*, Athens, Greece, 2011.

2010

H. Wu, A. Emadi, G. de Graaf, and R. F. Wolffenbittel, "Encapsulated thermopile detector array for IR microspectrometer," 2010, p. 76800Z.

H. Wu, A. Emadi, G. de Graaf, and R. F. Wolffenbittel, "Inference filter based absorber for thermopile detector array by surface micromachining," in *MME (Micromechanics Europe)*, Enschede, The Netherlands, 2010.

H. Wu, A. Emadi, G. de Graaf, and R. F. Wolffenbittel, "Thin film encapsulated 1D thermoelectric detector in an IR microspectrometer," 2010, p. 772612.

S. Chen, H. Wu, G. de Graaf, and R. F. Wolffenbittel, "Surface-micromachined gas sensor using thermopiles for carbon dioxide detection," in *MME (Micromechanics Europe)*, Enschede, The Netherlands, 2010.

G. de Graaf, H. Wu, and R. F. Wolffenbittel, "Thermal analysis, fabrication and signal processing of surface micromachined thermal conductivity based gas sensors," in *MME (Micromechanics Europe)*, Enschede, The Netherlands, 2010.

A. Emadi, H. Wu, G. de Graaf, and R. F. Wolffenbittel, "CMOS-compatible

LVOF-based visible microspectrometer," 2010, p. 76800W.

A. Emadi, H. Wu, G. de Graaf, and R. F. Wolffenbittel, "Post-Processing of Linear Variable Optical Filter on CMOS chip at die-level," in MME (Micromechanics Europe), Enschede, The Netherlands, 2010.

A. Emadi, H. Wu, G. de Graaf, K. Hedsten, P. Enoksson, J. H. Correia, and R. F. Wolffenbittel, "An UV linear variable optical filter-based microspectrometer," in Eurosensors XXIV conference, Linz, Austria, 2010, pp. 416-419.

A. Emadi, S. Grabarnik, H. Wu, G. de Graaf, and R. F. Wolffenbittel, "Spectral measurement with a linear variable filter using a LMS algorithm," in Eurosensors XXIV conference, Linz, Austria, 2010, pp. 504-507.

A. Emadi, S. Grabarnik, H. Wu, G. de Graaf, K. Hedsten, P. Enoksson, J. H. Correia, and R. F. Wolffenbittel, "Spectral measurement using IC-compatible linear variable optical filter," 2010, p. 77162G.

A. Emadi, V. R. S. S. Mokkapati, H. Wu, G. de Graaf, and R. F. Wolffenbittel, "Linear Variable Optical Filter with Silver metallic layers," in MME (Micromechanics Europe), Enschede, The Netherlands, 2010.

C. Liu, A. Emadi, H. Wu, G. de Graaf, and R. F. Wolffenbittel, "A CMOS 128-APS linear array integrated with a LVOF for highsensitivity and high-resolution micro-spectrophotometry," 2010, p. 772616.

2009

H. Wu, A. Emadi, G. de Graaf, J. Leijtens, and R. F. Wolffenbittel, "Self-powered optical sensor systems," in Solid-State Sensors, Actuators and Microsystems Conference, 2009. TRANSDUCERS 2009. International, 2009, pp. 1373-1376.

H. Wu, S. Grabarnik, G. de Graaf, A. Emadi, and R. F. Wolffenbittel, "Thermal cross-talk in IC-compatible micromachined infrared thermopile detector arrays," in IRS² SENSOR+TEST, Nurnberg, Germany, 2009, pp. 319-323.

H. Wu, A. Emadi, G. de Graaf, J. Leijtens, and R. F. Wolffenbittel, "Self-Powered Sun Sensor Microsystems," in Eurosensors XXIII conference, Lausanne, Switzerland, 2009, pp. 1363-1366.

H. Wu, S. Grabarnik, A. Emadi, G. de Graaf, and R. F. Wolffenbittel, "Study of Thermal Cross-Talk in Micromachined Thermopile based infrared detector arrays," in Sense of Contact, Zeist, the Netherlands, 2009.

A. Emadi, H. Wu, S. Grabarnik, G. de Graaf, and R. F. Wolffenbittel, "Interference filter based IR absorber for MEMS thermopile array," in MME (Micromechanics Europe), Toulouse, France, 2009, p. 217/D21.

A. Emadi, H. Wu, S. Grabarnik, G. de Graaf, and R. F. Wolffenbittel, "IC-compatible fabrication of linear variable optical filters for microspectrometer," in Eurosensors XXIII conference, Lausanne, Switzerland, 2009, pp. 1143-1146.

A. Emadi, S. Grabarnik, H. Wu, G. de Graaf, and R. F. Wolffenbittel, "IC-compatible fabrication of linear variable optical filter for micro-spectrometer," in Sense of Contact, Zeist, the Netherlands, 2009.

S. Grabarnik, A. Emadi, H. Wu, G. de Graaf, and R. F. Wolffenbittel, "Microspectrometer with a concave grating fabricated in a MEMS technology," in Eurosensors XXIII conference, Lausanne, Switzerland, 2009, pp. 401-404.

2008

H. Wu, S. Grabarnik, G. de Graaf, A. Emadi, and R. F. Wolffenbittel, "Characterization of thermal cross-talk in thermopile detector array used in a MEMS-based IR microspectrometer," in MME (Micromechanics Europe), Aachen, Germany, 2008, pp. 415-418.

H. Wu, S. Grabarnik, A. Emadi, G. de Graaf, and R. F. Wolffenbittel, "Cross-talk characterisation of a thermal detector array," in Eurosensors XXII conference, Dresden Germany, 2008, pp. 366-369.

H. Wu, A. Emadi, W. van der Vlist, S. Grabarnik, G. de Graaf, and R. F. Wolffenbittel, "Design and fabrication of a thermopile detector array with scaled elements for an integrated IR microspectrometer," in APCOT (Asia-Pacific Conference On Transducers and Micro-Nano Technology), Tainan, Taiwan, 2008,

pp. 213-216.

A. Emadi, H. Wu, S. Grabarnik, G. de Graaf, and R. F. Wolffenbittel, "Fabrication of tapered optical structures using resist reflow," in MME (Micromechanics Europe), Aachen, Germany, 2008, pp. 113-116.

A. Emadi, H. Wu, S. Grabarnik, G. de Graaf, and R. F. Wolffenbittel, "Simulation and analytical calculation of reflowed resist structures," in MME (Micromechanics Europe), Aachen, Germany, 2008, pp. 347-350.

S. Grabarnik, A. Emadi, H. Wu, G. de Graaf, G. Vdovin, and R. F. Wolffenbittel, "IC-compatible microspectrometer using a planar imaging diffraction grating," 2008, p. 699215.

S. Grabarnik, A. Emadi, H. Wu, G. de Graaf, and R. F. Wolffenbittel, "Concave diffraction gratings fabricated with planar lithography," 2008, p. 699214.

S. Grabarnik, A. Emadi, H. Wu, G. de Graaf, and R. F. Wolffenbittel, "Optical microspectrometer with planar grating and external spherical lens," in Eurosensors XXII conference, Dresden Germany, 2008, pp. 350-353.

S. Grabarnik, A. Emadi, H. Wu, G. de Graaf, G. Vdovin, and R. F. Wolffenbittel, "Design and fabrication of a thermopile detector array with scaled elements for an integrated IR microspectrometer," in APCOT (Asia-Pacific Conference On Transducers and Micro-Nano Technology), Tainan, Taiwan, 2008, pp. 53-56.

2007

H. Wu, A. Emadi, G. de Graaf, S. Grabarnik, and R. F. Wolffenbittel, "Design and fabrication of thermopile detector array for microspectrometer application," in MME (Micromechanics Europe), Guimaraes, Portugal, 2007, pp. 103-106.

A. Emadi, H. Wu, S. Grabarnik, G. de Graaf, and R. F. Wolffenbittel, "Infrared thermopile detector array for the integrated micro spectrometer," in IEEE Sensors, Atlanta, USA, 2007, pp. 435-438.

List of Publications

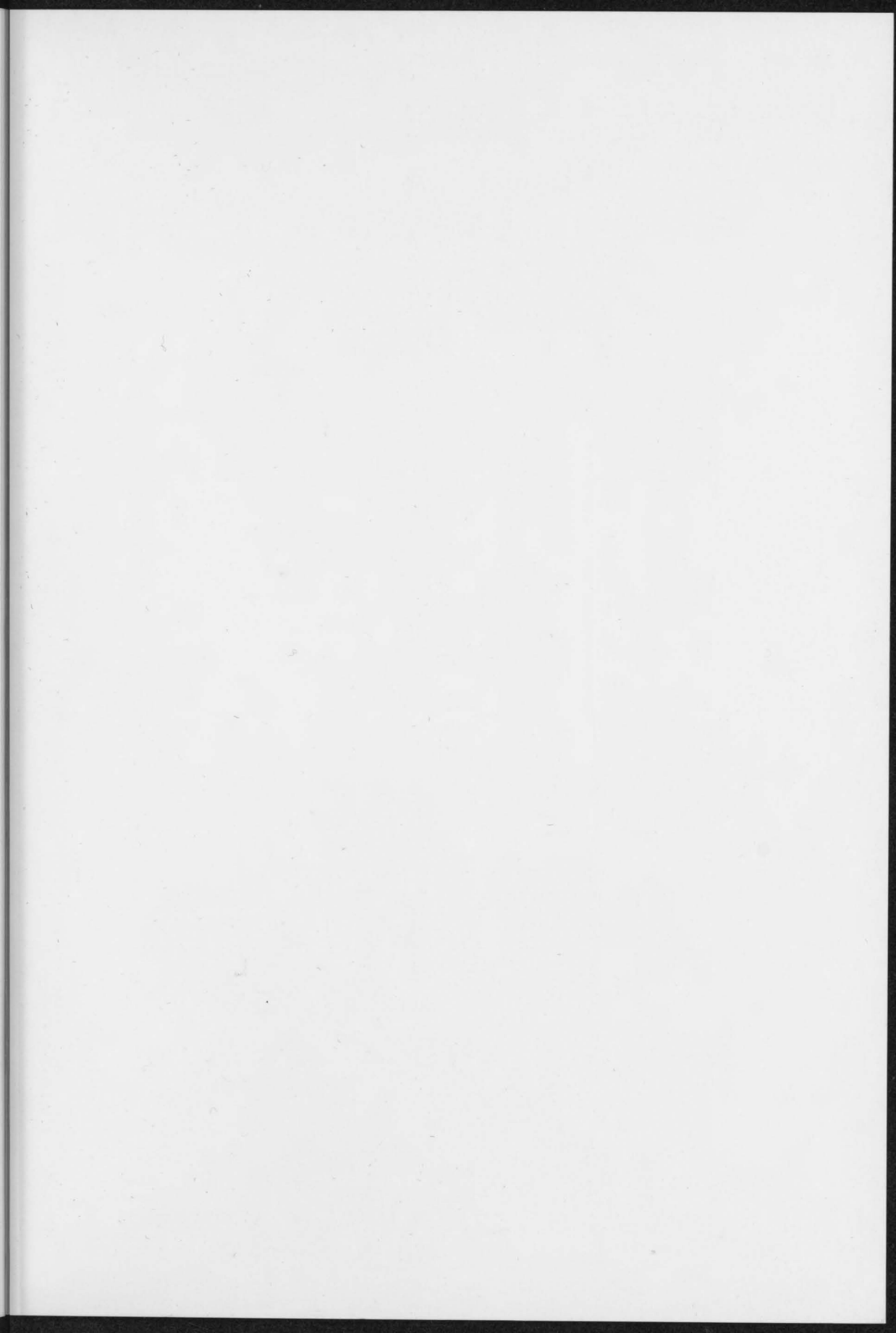
A. Emadi, S. Grabarnik, H. Wu, G. de Graaf, and R. F. Wolffenbuttel, "Fabrication and characterization of infra-red multi-layered interference filter," in MME (Micromechanics Europe), Guimaraes, Portugal, 2007, pp. 249-252.

S. Grabarnik, A. Emadi, H. Wu, G. de Graaf, G. Vdovin, and R. F. Wolffenbuttel, "Spectral sensor based on an imaging diffraction grating and fabricated with MEMS technologies," in MME (Micromechanics Europe), Guimaraes, Portugal, 2007, pp. 175-178.

About the author

Huaiwen (Wen) Wu was born in Taipei, Taiwan, on May 24, 1980. He received Bachelor degree in Electrical Engineering Department from the National Taipei University of Technology, Taipei, Taiwan, in 2002. After that, he served in Taiwan Marine Corps as a second lieutenant in an armored tank division for two years. In 2004, he worked on the design of tuner for set-up box in local electronic company in Taiwan. He completed the M.Sc. degree of Microelectronics at Delft University of Technology, the Netherlands in 2007 and is continuing his *Ph.D.* study in the Electronic Instrumentation Laboratory. His principal research interests are on high performance *CMOS* infrared thermal detector for mini-microspectrometer and micro & nano fabrication techniques.





dimes
Delft Institute of
Microsystems and
Nanoelectronics

 **TU Delft**
Delft
University of
Technology

ISBN 978-94-6190-102-6



9 789461 901026 >



**Sure,
I'm
Taiwan!
-ese!**